note 8579v1

Measurement of branching fractions and direct CP asymmetries of $B^0_{(s)} \to h^+h^{'-}$ decays in 1fb^{-1}

The CDF Collaboration
URL http://www-cdf.fnal.gov
(Dated: November 3, 2006)

We reconstruct a sample of about 6500 $B^0_{(s)} \to h^+h^{'-}$ (where $h, h' = K$ or π) in 1 fb^{-1} of data collected by the CDF II detector at the Fermilab Tevatron. We report the first observation of the mode $B^0_s \to K^-\pi^+$ with a yield of 230 ± 34 (*stat.*) $\pm$ 16 (*syst.*) events, corresponding to $(f_s/f_d) \times \mathcal{B}(B^0_s \to K^-\pi^+)/\mathcal{B}(B^0 \to K^+\pi^-) = 0.071 \pm 0.010(stat.) \pm 0.007(syst.)$, where f_s/f_d is the ratio of production fractions of B^0_s and B^0. With this sample, we perform the first measurement of a CP asymmetry in the B^0_s meson: $A_{\mathsf{CP}}(B^0_s \to K^-\pi^+) = 0.39 \pm 0.15$ (*stat.*) $\pm$ 0.08 (*syst.*). We also observe charmless decays of a b-baryon for the first time, in the modes $\Lambda^0_b \to p\pi^-$and $\Lambda^0_b \to pK^-$, with yields respectively of 110 ± 18 (*stat.*) $\pm$ 16 (*syst.*) events and of 156 ± 20 (*stat.*) $\pm$ 11 (*syst.*) events, from which we obtain $\mathcal{B}(\Lambda^0_b \to p\pi^-)/\mathcal{B}(\Lambda^0_b \to pK^-) = 0.66 \pm 0.14$ (*stat.*) $\pm$ 0.08 (*syst.*).

We also measure: $(f_s/f_d) \times \mathcal{B}(B^0_s \to K^+K^-)/\mathcal{B}(B^0 \to K^+\pi^-) = 0.347 \pm 0.020$ (*stat.*) $\pm$ 0.021 (*syst.*), $A_{\mathsf{CP}}(B^0 \to K^+\pi^-) = -0.086 \pm 0.023$ (*stat.*) $\pm$ 0.009 (*syst.*) and $\mathcal{B}(B^0 \to \pi^+\pi^-)/\mathcal{B}(B^0 \to K^+\pi^-) = 0.259 \pm 0.017$ (*stat.*) $\pm$ 0.016 (*syst.*). We find no significant signal for the modes $B^0 \to K^+K^-$ and $B^0_s \to \pi^+\pi^-$, and set upper limits at 90% CL: $\mathcal{B}(B^0 \to K^+K^-) < 0.7 \times 10^{-6}$, and $\mathcal{B}(B^0_s \to \pi^+\pi^-) < 1.3 \times 10^{-6}$.

The results reported in this document are slightly updated on April 10, 2008. The update is about only a more precise measurement of the isolation efficiency ratio between B^0 and B^0_s mesons.

Preliminary Results for fall 2006 Conferences

I. INTRODUCTION

The decay modes of B mesons into pairs of charmless pseudoscalar mesons are effective probes of the quark-mixing (CKM) matrix and are sensitive to potential new physics effects. The large production of B hadrons of all kinds at the Tevatron allows to measure such decays in new modes, which are important to supplement our understanding of B meson decays.

The still unobserved $B_s^0 \to K^-\pi^+$ mode can be used in measuring γ [3], and its CP asymmetry is a powerful model-independent test [7] of the source of the direct CP asymmetry in the B system, especially important in view of the current discrepancy between the asymmetries observed in the neutral and charged mode[23].

The $B_s^0 \to \pi^+\pi^-$ mode only proceeds through annihilation diagrams, which are currently poorly known and a source of significant uncertainty in many theoretical calculations [9]. Its features are similar to the as yet unobserved $B^0 \to K^+K^-$ mode, but it has a larger predicted branching fraction [9, 10]; a measurement of both modes would allow a determination of the strength of penguin-annihilation [4].

Throughout this paper, C-conjugate modes are implied and branching fractions indicate CP-averages unless otherwise stated.

II. DATA SAMPLE & EVENT SELECTION

We analyzed a $\int \mathcal{L}dt \simeq 1$ fb^{-1} sample of pairs of oppositely-charged particles, used to form $B_{(s)}^0$ meson candidates, with $p_T > 2$ GeV$/c$ and $p_T(1) + p_T(2) > 5.5$ GeV$/c$. The trigger required also a transverse opening-angle between tracks $20° < \Delta\phi < 135°$ to reject background from particles within light-quark jets. In addition, both charged particles were required to originate in a displaced vertex ($100\ \mu$m $< d_0 < 1$ mm), while the $B_{(s)}^0$ meson candidate was required to be produced in the primary p$\bar{\text{p}}$ interaction ($d_0(B) < 140\ \mu$m) and to have traveled a transverse distance $L_{xy}(B) > 200\ \mu$m.

A $B_{(s)}^0 \to h^+h^{'-}$ signal of about 14500 events and signal-to-noise ratio SNR $\simeq 0.2$ at peak is visible in data (Fig. 1) already after confirming the trigger selection on offline quantities: extraction of a $\mathcal{B} \simeq 10^{-5}$ signal at trigger-level is a remarkable achievement at a hadron collider, made it possible by the CDF trigger on displaced tracks.

In the offline analysis, an unbiased procedure of optimization determined a tightened selection on track-pairs fit to a common decay-vertex. For this analysis, we chose the selection cuts by the approach of minimizing the expected uncertainty individually for each of the physical observables to be measured. The uncertainty on each observable has been parameterized with analytical functions of the signal yield (S) and background level (B), and the free parameters determined from analysis of pseudo-experiments reproducing the experimental circumstance of data.
For each set of cuts, S was estimated from Monte Carlo simulation and normalized to the yield observed in data after the trigger selection, and B is the background extrapolated from the sidebands of the $\pi\pi$-mass distribution in the data. We chose to use just two different sets of cuts, respectively optimized to measure $A_{\mathsf{CP}}(B^0 \to K^+\pi^-)$ (Tab. IV) and $(f_s/f_d) \cdot \mathcal{B}(B_s^0 \to K^-\pi^+)/\mathcal{B}(B^0 \to K^+\pi^-)$ (Tab. V), since those two observables are the main focus of this analysis. For the latter, the sensitivity for discovery and limit setting[16] was optimized rather than the resolution on a particular parameter, since the mode had not yet been observed. It was verified that the former set of cuts is also well suited to measure all other observables related to the large-yield modes ($B^0 \to \pi^+\pi^-$, $B_s^0 \to K^+K^-$), while the latter, tighter set of cuts, is well-suited to measure all other observables related to rare modes ($B_s^0 \to \pi^+\pi^-$, $B^0 \to K^+K^-$, $\Lambda_b^0 \to p\pi^-$, $\Lambda_b^0 \to pK^-$).

Besides tightening the trigger cuts, in the offline analysis the discriminating power of the $B_{(s)}^0$ meson 'isolation' and the information provided by the 3D reconstruction capability of CDF tracking have been used to obtain a great improvement in the signal purity. Isolation is defined as $I(B) = p_{\rm T}(B)/[p_{\rm T}(B) + \sum_i p_{\rm T}(i)]$, in which the sum runs over every other track within a cone of radius one in the $\eta - \phi$ space around the $B_{(s)}^0$ meson flight-direction. By requiring $I(B) > 0.5$ in addition to the trigger cuts (Tab. III), we reduced the background by a factor four while keeping almost 80% of signal. The 3D view of tracking ($\chi^2_{3D}(B)$) allowed to resolve multiple vertices along the beam direction, thus reducing the background (mainly pairs of displaced tracks coming from distinct, uncorrelated heavy-flavor decays) by a factor two, with a small inefficiency on the signal.

The resulting $\pi\pi$-mass distributions (Fig. 2 selection optimized to measure $A_{\mathsf{CP}}(B^0 \to K^+\pi^-)$, Fig. 3 selection optimized to measure $(f_s/f_d) \cdot \mathcal{B}(B_s^0 \to K^-\pi^+)/\mathcal{B}(B^0 \to K^+\pi^-)$) show clean signals of $B_{(s)}^0 \to h^+h^{'-}$ candidates. A simple estimate of event yields has been done using a binned one-dimensional fit with a Gaussian (signal) plus an Exponential (combinatoric background) and an Argus-shaped (physical background) function. We found 6509 ± 159 events, with standard deviation $\sigma = 39 \pm 0.8$ MeV$/c^2$ and SNR $\simeq 8.3$ at peak applying the selection (Tab. IV) optimized for $A_{\mathsf{CP}}(B^0 \to K^+\pi^-)$ and 4918 ± 209 events, with standard deviation $\sigma = 38 \pm 1$ MeV$/c^2$ and SNR $\simeq 13$

at peak applying the selection (Tab. V) optimized for $(f_s/f_d) \cdot \mathcal{B}(B_s^0 \to K^-\pi^+)/\mathcal{B}(B^0 \to K^+\pi^-)$.

In spite of a good mass resolution ($\simeq$22 MeV/c^2), the $B_{(s)}^0 \to h^+h^{'-}$ modes overlap into an unresolved mass peak, and the Monte Carlo $\pi\pi$-mass distributions (Fig. 4) show clearly the anatomy of the $B_{(s)}^0 \to h^+h^{'-}$ signals. The peak is composed by the main modes already observed $B^0 \to \pi^+\pi^-$, $B^0 \to K^+\pi^-$, $B_s^0 \to K^+K^-$ and by the rare modes not yet observed $B^0 \to K^+K^-$, $B_s^0 \to K^-\pi^+$, $B_s^0 \to \pi^+\pi^-$, $\Lambda_b^0 \to p\pi^-$, $\Lambda_b^0 \to pK^-$. Since also the PID resolution is insufficient for separating them on an event-by-event basis, we achieved a statistical separation performing a multivariate, unbinned, maximum-likelihood fit (fit of composition) that use PID information (provided by the dE/dx in the drift chamber) and kinematics.

III. FIT OF COMPOSITION

We performed the fit of composition, combining kinematic and particle identification information, in order to statistically determine the contribution of each mode, and to measure the CP asymmetry of the $B^0 \to K^+\pi^-$ and $B_s^0 \to K^-\pi^+$ modes. For the kinematic portion, we used three loosely correlated observables to summarize the information carried by all possible values of invariant mass of the candidate B, resulting from different mass assignments to the two outgoing particles [15]. They are: a) the mass $M_{\pi\pi}$ calculated with the pion mass assignment to both particles; b) the signed momentum imbalance $\alpha = (1-p_1/p_2)q_1$, where p_1 (p_2) is the lower (higher) of the particle momenta, and q_1 is the sign of the charge of the particle of momentum p_1; c) the scalar sum of the particle momenta $p_{tot} = p_1 + p_2$. Using these three variables, the mass of any particular mode M_{12} ($M_{K\pi}, M_{\pi K}, M_{KK}, M_{p\pi}, M_{\pi p}, M_{pK}, M_{Kp}$) can be expressed as:

$$M_{12}^2 = M_{\pi\pi}^2 - 2m_\pi^2 + (m_1^2 + m_2^2) - 2 \cdot \left(\sqrt{p_1^2 + m_\pi^2} \cdot \sqrt{p_2^2 + m_\pi^2} - \sqrt{p_1^2 + m_1^2} \cdot \sqrt{p_2^2 + m_2^2}\right) \tag{1}$$

$$p_1 = \frac{1-|\alpha|}{2-|\alpha|}p_{tot} \qquad p_2 = \frac{1}{2-|\alpha|}p_{tot} \tag{2}$$

where m_1 (m_2) is the mass of the lower (higher) momentum particle. For simplicity the Eq. 1 is written as function of p_1 and p_2 instead of α and p_{tot}.

The kinematic differences exploited to separate between the modes are graphically visible in the correlation between the invariant $\pi\pi$-mass $M_{\pi\pi}$ and α (Figs. 25,26,27) or better in the bi-dimensional distribution of averaged $< M_{\pi\pi} >$ as a function of α (Fig. 28). By combining kinematics and charge we therefore separate also the self-tagging mode (e.g. $B^0 \to K^+\pi^-$ from $\overline{B}^0 \to K^-\pi^+$). The p_{tot} observable does not provide a large power separation between the signal modes in the kinematic side but it plays a key role in order to account for the dependence of the particle identification observables on particle momentum: p_{tot} in conjunction with α provides unique identification of the momenta of both particles.

Particle identification (PID) information is summarized by a single observable ID for each track defined as:

$$\mathsf{ID}(\text{track}) = \frac{\left.\frac{\text{dE}}{\text{dx}}\right|_{\text{meas}}(\text{track}) - \left.\frac{\text{dE}}{\text{dx}}\right|_{\pi}(\text{track})}{\left.\frac{\text{dE}}{\text{dx}}\right|_{\text{K}}(\text{track}) - \left.\frac{\text{dE}}{\text{dx}}\right|_{\pi}(\text{track})} \tag{3}$$

where the $dE/dx|_{meas}$ is the measured energy lost by the particle in the drift chamber and the $dE/dx|_{\pi(K)}$ is the expected value for the energy lost in the drift chamber in a given particle hypothesis $\pi(K)$ given the particle momentum. The average of ID observable respectively in pion and kaon particle hypothesis is $< \mathsf{ID} >_\pi = 0$ and $< \mathsf{ID} >_K = 1$.

With the chosen observables, the likelihood contribution of the i^{th} event is written as:

$$\mathcal{L}_i = (1-b)\sum_j f_j \mathcal{L}_j^{\text{kin}} \mathcal{L}_j^{\text{PID}} + b\left(f_{\text{A}}\mathcal{L}_{\text{A}}^{\text{kin}}\mathcal{L}_{\text{A}}^{\text{PID}} + (1-f_{\text{A}})\mathcal{L}_{\text{E}}^{\text{kin}}\mathcal{L}_{\text{E}}^{\text{PID}}\right) \tag{4}$$

where:

$$\begin{aligned}
\mathcal{L}_j^{\text{kin}} &= R(M_{\pi\pi} - \mathcal{M}_j(\alpha, p_{tot}), \alpha, p_{tot})P_j(\alpha, p_{\text{tot}}) && (5)\\
\mathcal{L}_{\text{A}}^{\text{kin}} &= \text{Argus}(M_{\pi\pi}|c_2, m_0)P_{\text{A}}(\alpha, p_{\text{tot}}) && (6)\\
\mathcal{L}_{\text{E}}^{\text{kin}} &= e^{c_1 M_{\pi\pi}} P_{\text{E}}(\alpha, p_{\text{tot}}) && (7)\\
\mathcal{L}_{j(\text{E,A})}^{\text{PID}} &= F_{j(\text{E,A})}(\mathsf{ID}_1, p_1(\alpha, p_{\text{tot}}), \mathsf{ID}_2, p_2(\alpha, p_{\text{tot}})) && (8)
\end{aligned}$$

The index 'A(E)' labels the combinatorial(physical) background-related quantities, the index j runs over the twelve distinguishable $B^0_{(s)} \to h^+h^{'-}$ and $\Lambda^0_b \to ph^-$ modes (Fig. 28), and f_j are their fractions, to be determined by the fit together with the total background fraction b and with the fraction of the physical(combinatorial) background $f_{A(E)}$. The conditional probability density $R(M_{\pi\pi} - \mathcal{M}_j(\alpha, p_{tot}), \alpha, p_{tot})$ is the mass resolution function of each mode j when the correct mass is assigned to both tracks. In fact the average mass $\mathcal{M}_j(\alpha, p_{tot})$ is the value of $M_{\pi\pi}$ obtained from Eq. (1) by setting the appropriate particle mass for each decay mode j. Making a simple variables change we obtain $R(M_{\pi\pi} - \mathcal{M}_j(\alpha, p_{tot}), \alpha, p_{tot}) = R(M_j - M_{B^0(B^0_s, \Lambda^0_b)}, \alpha, p_{tot})$ where M_j is invariant mass computed with the correct mass assignment to both particles for each mode j. R resolution function was parameterized with an accurate study using the detailed full CDF II simulation. To keep into account all non gaussian tails due to the emission of one or more photons in the final state (FSR) we modified "ad hoc" the CDF II simulation and we introduced the soft photon emission in agreement with the recent QED calculations [18] (Figs. 7, 8 and Figs. [9-16]). The width of the mass resolution function R is momenta dependent and the dependences by α and p_{tot} can be considered with good approximation independent (Figs. [17-24]). The dominant gaussian of the parameterization (about 85% of the total) has a averaged width $< \sigma >_{\alpha, p_{tot}} \simeq 22$ MeV/c^2.
We checked the goodness of the mass resolution model using an huge sample of $D^{*+} \to D^0\pi^+ \to [K^-\pi^+]\pi^+$ decays (Fig. 5) fitting the mass line shape of the $D^0 \to K^-\pi^+$ peak, where the signal function was completely fixed from the model, while the background function was free to vary (straight line) obtaining a very good agreement between data and simulation.
We used the B^0,B^0_s and Λ^0_b masses measured by CDF [19] to cancel the common systematic uncertainty. The background mass distribution is determined in the fit by varying the parameters c_1, c_2 and m_0 in Eq. (6,7). The $P_j(\alpha, p_{\rm tot})$ is the joint probability distribution of $(\alpha, p_{\rm tot})$, and is parameterized for each mode j by a product of polynomial and exponential functions (Figs. [29-36]) fitted to Monte Carlo samples produced by a detailed detector simulation. The background function $P_{\rm A(E)}$ is obtained from the mass sidebands of data.

A sample of 1.5×10^6 $D^{*+} \to D^0\pi^+ \to [K^-\pi^+]\pi^+$ decays, where the D^0 decay products are identified by the charge of the D^{*+} pion, was used to calibrate the dE/dx response over the tracking volume and time, and to determine the F functions in (8) [20]. The $\mathcal{O}(0.4\%)$ contamination from doubly Cabibbo-suppressed $D^0 \to K^+\pi^-$ decays was neglected. In a $> 95\%$ pure D^0 sample, we obtained 1.4σ separation between kaons and pions (Fig. 6), corresponding to an uncertainty on the measured fraction of each class of particles that is just 60% worse than the uncertainty attainable with ideal separation. We measured a 11% residual track-to-track correlation due to common-mode dE/dx fluctuations and since the correlation is sample dependent we fitted in the fit of composition the dE/dx correlation of the $B^0_{(s)} \to h^+h^{'-}$ modes using a sum of two gaussian.

The background term in (8) is similar to the signal terms, but allows for independent pion, kaon, proton, and electron components, which are free to vary independently. Muons are indistinguishable from pions with the available dE/dx resolution.

IV. FIT RESULTS

We performed two different fits: the first one on the data sample optimized to measure the direct $A_{\mathsf{CP}}(B^0 \to K^+\pi^-)$ and the second one to measure $(f_s/f_d) \cdot \mathcal{B}(B^0_s \to K^-\pi^+)/\mathcal{B}(B^0 \to K^+\pi^-)$.
The fits returned the fractions and the yields listed in Tabs. VI, VIII while the complementary results are reported in Tabs. VII, IX. Significant signals were seen for $B^0 \to \pi^+\pi^-$, $B^0 \to K^+\pi^-$, and $B^0_s \to K^+K^-$ mode previously observed by CDF [21], three new rare modes were observed for the first time $B^0_s \to K^-\pi^+$, $\Lambda^0_b \to p\pi^-$ and $\Lambda^0_b \to pK^-$ while no evidence was obtained for $B^0_s \to \pi^+\pi^-$and $B^0 \to K^+K^-$mode.

In order to visualize the agreement between the fit and the data, we reported the plots of the fit projections. The relevant projections are those onto the fit observables $m_{\pi\pi}$, α, p_{tot}, $\mathsf{ID}(1)$ and $\mathsf{ID}(2)$ and other two additional PID observables (linear combination of ID_1 and ID_2) $\mathsf{ID}_{sum} = \mathsf{ID}_1 + \mathsf{ID}_2$ and $\mathsf{ID}_{dif} = \mathsf{ID}_1 - \mathsf{ID}_2$ (Figs. 37-50). An alternative way to check the goodness of the fit of composition and to visualize the separation power between the different modes is the "*probability ratio plot*" (Figs. 51-62). The agreement between data and fit function is very satisfactory.

To convert raw yields into relative branching fractions, we applied corrections for the different efficiencies of trigger and offline selection requirements for different decay modes; the relative efficiency corrections between modes do not exceed 19%. Most corrections were determined from the detailed detector simulation, with some exceptions which are measured using data. A momentum-averaged relative isolation efficiency between B^0_s and B^0 of 1.07 ± 0.11 was determined from fully-reconstructed samples of $B^0_s \to J/\psi\,\phi$, $B^0_s \to D^-_s\pi^+$, $B^0 \to J/\psi\,K^{*0}$, and $B^0 \to D^-\pi^+$. The lower specific ionization of kaons with respect to pions in the drift chamber is responsible for a $\simeq 5\%$ lower efficiency to reconstruct a kaon by the XFT. This effect was measured in a sample of $D^+ \to K^-\pi^+\pi^+$ decays triggered on two tracks, using the unbiased third track. The only correction needed by the direct CP-asymmetries $A_{\mathsf{CP}}(B^0 \to K^+\pi^-)$

and $A_{\mathsf{CP}}(B^0_s \to K^-\pi^+)$ was a $\leq 0.6\%$ shift due to the different probability for K^+ and K^- to interact with the tracker material. The measurement of this probability ratio has been done using an huge control sample of prompt $D^0 \to K^-\pi^+$ decays (Figs. 63, 64) reconstructed and selected using the same criteria of $B^0_{(s)} \to h^+h^{'-}$ decays. Assuming that the Standard Model predicts $A_{\mathsf{CP}}(D^0 \to K^-\pi^+) = 0$, the measurement of the raw direct CP asymmetry provides the measurement from the data (without using the Monte Carlo) of the probability ratio K^+/K^-. Since we used the same fit technique developed for the $B^0_{(s)} \to h^+h^{'-}$ decays (Figs. 65) this measurement provides also a robust check on all possible charge asymmetry biases of the detector, of the calibration and parameterization of PID pdfs and of the parameterization of the kinematic pdfs.
The $B^0_s \to K^+K^-$ and $B^0_s \to \pi^+\pi^-$ modes required a special treatment, since they contain a superposition of the flavor eigenstates of the B^0_s. Their time evolution might differ from the flavor-specific modes if the width difference $\Delta\Gamma_s$ between the B^0_s mass eigenstates is significant. The current result was derived under the assumption that both modes are dominated by the short-lived B^0_s component , that $\Gamma_s = \Gamma_d$, and $\Delta\Gamma_s/\Gamma_s = 0.12 \pm 0.06$ [22]. The latter uncertainty is included in estimating the overall systematic uncertainty.

V. SYSTEMATIC UNCERTAINTIES

The dominant contributions to the systematic uncertainty are: the statistical uncertainty on isolation efficiency (B^0_s modes), the uncertainty on the dE/dx calibration and parameterization and the uncertainty of the combinatorial background model. The former is the larger systematics of all measurements with the meson B^0_s in the initial state (except for $A_{\mathsf{CP}}(B^0_s \to K^-\pi^+)$). It is a conservative systematics since the measurement of relative isolation efficiency ratio was performed on the first 180 pb^{-1}: using all data sample available (1 fb^{-1}), we expect a reduction factor $\simeq 2.7$ for this systematics. Although the parameterization of the dE/dx is very accurate the related systematic uncertainty is dominant since the fit of composition is very sensitive to the PID information. Finally the latter is due to the statistical uncertainty of the possible combinatorial background models and it is a dominant systematics for the observables of the rare modes as $B^0 \to K^+K^-$ $B^0_s \to \pi^+\pi^-$, $B^0_s \to K^-\pi^+$, $\Lambda^0_b \to p\pi^-$ and $\Lambda^0_b \to pK^-$. Smaller systematic uncertainties are assigned for: trigger efficiencies; background shape and kinematics; B meson masses, lifetimes, and differences in momenta, allowed to vary by a factor $(m_{B^0_s} - m_{B^0})/m_{B^0}$ due to fragmentation effects.
The systematics uncertainties are listed in the Tables [X-XXIII]. Here a short explanation of the systematics uncertainties.

- *Mass scale.* The central fit is performed by assuming a known global mass scale, in which we assign to the B^0, B^0_s and Λ^0_b masses the values measured in Run II [19]. Since the mass is one of the information used in separating all the different contributions it is interesting to check how the fit behaves when the mass scale is allowed to float. An additional output parameter Δ was added to the fit in the parameterization of the input masses: $m^{\rm fit}_{B^0_s} = m^{\rm CDFII}_{B^0_s} + \Delta$, $m^{\rm fit}_{B^0} = m^{\rm CDFII}_{B^0} + \Delta$ and $m^{\rm fit}_{\Lambda^0_b} = m^{\rm CDFII}_{\Lambda^0_b} + \Delta$ and the global scale of masses is determined to be: 0.1 ± 0.6 MeV/c^2. Then, we generated an ensemble of pseudo-experiments in which the global mass scale is shifted by the above measured value, and we applied the fit to these toy-MC.

- *Input masses.* The B masses are an input parameter to the fit through the analytic expressions of $\mathcal{M}_j(\alpha, p_{tot})$. We generated distinct ensembles of pseudo-experiments in which we independently varied the B^0, B^0_s, Λ^0_b and input masses within $\pm 1\sigma$ statistical uncertainty of the published CDF II measurement [19] to evaluate the systematics due to the uncertainty on the input masses.

- *Asymmetries in p.d.f.(α, p_{tot}).* In order to take into account hidden asymmetries in the distributions of the probability densities for symmetric modes and background, we repeated the fit after refitting the templates with asymmetric fit functions.

- *Momentum background model p.d.f.(α, $p_{\rm tot}$)* In order to take into account the different composition of the background (combinatorial plus physical background), in the distributions of (α, p_{tot}) we repeated the fit after refitting the templates using the two different methods to parameterize $P_{\rm A}(\alpha, p_{\rm tot})$ and $P_{\rm E}(\alpha, p_{\rm tot})$.

- *dE/dx induced systematics.* We repeated the global fit by varying the parameters associated to dE/dx calibrations within a 1σ-radius multidimensional sphere in the space of the parameters of the dE/dx calibrations.

- *Combinatorial-background model:* The central fit uses an exponential distribution for the combinatorial background. We repeated the fit on large ensembles of pseudo-experiments using polynomial distributions (third degree maximum) for the combinatorial background.

- *Monte Carlo statistics.* This is the uncertainty deriving from the limited statistics of the Monte Carlo samples used to estimate the relative efficiencies. The statistic uncertainty on the relative efficiencies is 0.0004.

- *Charge Asymmetry.* We associated a systematic uncertainty corresponding to $\pm 1\sigma$ variation of the measurement of $\varepsilon(K^+\pi^-)/\varepsilon(K^-\pi^+) = 1.0131 \pm 0.0028$ (*stat.*) performed using the sample of prompt $D^0 \to K^-\pi^+$ decays.

- *Lifetime induced systematics* The selection of the sample relies on both track impact parameters (d_0) and on transverse decay length of the B candidate ($L_{xy}(B)$) cuts, therefore we assigned a systematic uncertainty due to the experimental uncertainty on the measurement of $\tau(B^0)$ and $\tau(B^0_s)$ from semileptonic decays. This affects also the $\tau(B^0_s \to K^+K^-)$ since also $\tau(B^0_s \to K^+K^-)$ is evaluated from Γ_d in the central fit (see Sec. IV). The additional systematics on $\tau(B^0_s \to K^+K^-)$ coming from the uncertainty on $\Delta\Gamma_s/\Gamma_s$ is evaluated separately.

- *Systematics from* $\Delta\Gamma_s/\Gamma_s$. The measurements involving $B^0_s \to K^+K^-$ and $B^0_s \to \pi^+\pi^-$ suffer from the additional systematic uncertainty coming from the error on $\Delta\Gamma_s/\Gamma_s$. To quote the results from the central fit we assumed the Standard Model expectations for the lifetime-difference which has a 50% relative uncertainty ($\Delta\Gamma_s/\Gamma_s = 0.12 \pm 0.06$)[22].

- *Uncertainty on the B-isolation efficiency.* We measured a momentum-averaged relative isolation efficiency between B^0_s and B^0 of 1.000 ± 0.028 using the fully-reconstructed samples of $B^0_s \to J/\psi\,\phi$ and $B^0 \to J/\psi\,K^{*0}$. The statistical uncertainty $\sigma_{iso} \simeq 2.8\%$ contributed to systematic uncertainty to all measurements with a B^0_s meson in the initial state (except to $A_{\mathsf{CP}}(B^0_s \to K^-\pi^+)$).

- *Uncertainty on the XFT-bias correction.* The lower specific ionization of kaons with respect to pions in the drift chamber is responsible for a $\simeq 5\%$ lower efficiency to reconstruct a kaon by the XFT. This effect was measured in a sample of $D^+ \to K^-\pi^+\pi^+$ decays triggered on two tracks, using the unbiased third track. We quoted an associated systematics due to the uncertainty of the parameterization of this effect.

VI. RESULTS

The relative branching fractions obtained after applying all corrections are listed in Table I and in Table II, where f_d and f_s indicate the production fractions respectively of B^0 and B^0_s from fragmentation of a b quark in $\bar{p}p$ collisions. Upper limits are quoted also for modes in which no significant signal is observed [24]. We also list absolute results obtained by normalizing our data to the world-average of $\mathcal{B}(B^0 \to K^+\pi^-)$ and assuming for f_s and f_d the world-averages from $\bar{p}p$ and e^+e^- experiments [23].

We observed for the first time three new rare charmless decays $B^0_s \to K^-\pi^+$, $\Lambda^0_b \to p\pi^-$ and $\Lambda^0_b \to pK^-$respectively with a significance of 8.2σ, 6σ and 11.5σ. The significance includes both statistic and systematic uncertainty and in particular the statistic uncertainty to estimate the significance of these new modes was calculated using several pseudo-experiments where the fractions of the rare modes were fixed to 0 (Fig. 66 and Tab. XXIV).

The rate of the newly observed mode $\mathcal{B}(B^0_s \to K^-\pi^+) = 5.27 \pm 0.74 \pm 0.90$ is in agreement with the latest theoretical expectation $\mathcal{B}(B^0_s \to K^-\pi^+ \;\simeq 4.9 \cdot 10^{-6})$ [25]. This mode is a self-tagging mode as $B^0 \to K^+\pi^-$and we measured (for the first time in the B$_s$-meson system) its direct CP asymmetry $A_{\mathsf{CP}}(B^0_s \to K^-\pi^+) = 0.39 \pm 0.15 \pm 0.08$. It is different from 0 by 2.5σ and it is in agreement with the Standard Model expectation $\simeq 0.37$ [7] calculated using the just now measured $\mathcal{B}(B^0_s \to K^-\pi^+)$. In the same paper [7] it is suggested a robust test of the Standard Model vs New Physics by comparison of the direct CP asymmetries in the $B^0_s \to K^-\pi^+$ and $B^0 \to K^+\pi^-$ decays. In particular the Standard Model with some minimal assumption predicts that

$$|A(\overline{B}^0 \to K^-\pi^+)|^2 - |A(B^0 \to K^+\pi^-)|^2 \;=\; |A(B^0_s \to K^-\pi^+)|^2 - |A(\overline{B}^0_s \to K^+\pi^-)|^2$$

and we measured (using HFAG input [23])

$$\frac{\Gamma(\overline{B}^0 \to K^-\pi^+) - \Gamma(B^0 \to K^+\pi^-)}{\Gamma(B^0_s \to K^-\pi^+) - \Gamma(\overline{B}^0_s \to K^+\pi^-)} = 0.78 \pm 0.39 \pm 0.12$$

in agreement with the Standard Model expectation (where Γ is the decay width and A is the decay amplitude $\Gamma \propto |A|^2$).

The rate of the mode $\mathcal{B}(B^0_s \to K^+K^-) = 25.8 \pm 1.5 \pm 3.9$ is in agreement with the latest theoretical expectation $\mathcal{B}(B^0_s \to K^+K^-) \simeq \mathcal{B}(B^0 \to K^+\pi^-)$ [26, 27] and with the previous CDF measurement [21] and disfavors the higher values predicted by calculations based on QCD sum rules [4, 28] implying large U-spin breaking in this process.

mode	N_s	Quantity	Measurement	$\mathcal{B}(10^{-6})$
$B^0 \to \pi^+\pi^-$	1121 ± 63	$\frac{\mathcal{B}(B^0\to\pi^+\pi^-)}{\mathcal{B}(B^0\to K^+\pi^-)}$	0.259 ± 0.017 ± 0.016	5.02 ± 0.33 ± 0.35
$B^0 \to K^+\pi^-$	4045 ± 84	$\frac{\mathcal{B}(\overline{B}^0\to K^-\pi^+)-\mathcal{B}(B^0\to K^+\pi^-)}{\mathcal{B}(\overline{B}^0\to K^-\pi^+)+\mathcal{B}(B^0\to K^+\pi^-)}$	-0.086 ± 0.023 ± 0.009	
$B^0_s \to K^+K^-$	1307 ± 64	$\frac{f_s}{f_d}\frac{\mathcal{B}(B^0_s\to K^+K^-)}{\mathcal{B}(B^0\to K^+\pi^-)}$	0.347 ± 0.020 ± 0.021	25.8 ± 1.5 ± 3.9

TABLE I: Summary of results (selection optimized to measure the direct $A_{\mathsf{CP}}(B^0 \to K^+\pi^-)$ and the quantities of the large modes). Absolute branching fractions are normalized to the the world–average values $\mathcal{B}(B^0 \to K^+\pi^-) = (19.4 \pm 0.6) \times 10^{-6}$ and $f_s = (10.4 \pm 1.4)\%$ and$f_d = (39.8 \pm 1.0)\%$ [23]. The first quoted uncertainty is statistical, the second is systematic.

mode	N_s	Quantity	Measurement	$\mathcal{B}(10^{-6})$
$B^0_s \to K^-\pi^+$	230 ± 34 ± 16	$\frac{f_s}{f_d}\frac{\mathcal{B}(B^0_s\to K^-\pi^+)}{\mathcal{B}(B^0\to K^+\pi^-)}$	0.071 ± 0.010 ± 0.007	5.27 ± 0.74 ± 0.90
		$\frac{\mathcal{B}(\overline{B}^0_s\to K^+\pi^-)-\mathcal{B}(B^0_s\to K^-\pi^+)}{\mathcal{B}(\overline{B}^0_s\to K^+\pi^-)+\mathcal{B}(B^0_s\to K^-\pi^+)}$	0.39 ± 0.15 ± 0.08	
		$\frac{f_d}{f_s}\frac{\Gamma(\overline{B}^0\to K^-\pi^+)-\Gamma(B^0\to K^+\pi^-)}{\Gamma(\overline{B}^0_s\to K^+\pi^-)-\Gamma(B^0_s\to K^-\pi^+)}$	-3.00 ± 1.50 ± 0.22	
$B^0_s \to \pi^+\pi^-$	26 ± 16 ± 14	$\frac{f_s}{f_d}\frac{\mathcal{B}(B^0_s\to\pi^+\pi^-)}{\mathcal{B}(B^0\to K^+\pi^-)}$	0.007 ± 0.004 ± 0.005	0.52 ± 0.29 ± 0.38 (< 1.3 @ 90% CL)
$B^0 \to K^+K^-$	61 ± 25 ± 35	$\frac{\mathcal{B}(B^0\to K^+K^-)}{\mathcal{B}(B^0\to K^+\pi^-)}$	0.020 ± 0.008 ± 0.006	0.39 ± 0.16 ± 0.12 (< 0.7 @ 90% CL)
$\Lambda^0_b \to pK^-$	156 ± 20 ± 11	$\frac{\mathcal{B}(\Lambda^0_b\to p\pi^-)}{\mathcal{B}(\Lambda^0_b\to pK^-)}$	0.66 ± 0.14 ± 0.08	
$\Lambda^0_b \to p\pi^-$	110 ± 18 ± 16			

TABLE II: Summary of results (selection optimized to measure $(f_s/f_d) \cdot \mathcal{B}(B^0_s \to K^-\pi^+)/\mathcal{B}(B^0 \to K^+\pi^-)$ and the quantities of the rare modes). Absolute branching fractions are normalized to the the world–average values $\mathcal{B}(B^0 \to K^+\pi^-) = (19.4 \pm 0.6) \times 10^{-6}$ and $f_s = (10.4 \pm 1.4)\%$ and$f_d = (39.8 \pm 1.0)\%$ [23]. The first quoted uncertainty is statistical, the second is systematic.

While the systematic uncertainty of the measurement of relative branching fraction has the same order of statistical uncertainty (see Table I), in the absolute measurement of $\mathcal{B}(B^0_s \to K^+K^-)$ the systematic uncertainty is dominant bucause of the large uncertainties on $f_d = (39.8 \pm 1.0)\%$ and $f_s = (10.4 \pm 1.4)\%$ from [23].

The results for the B^0 are in agreement with world average values [23]. The measurement of the direct $A_{\mathsf{CP}}(B^0 \to K^+\pi^-) = -0.086 \pm 0.023 \pm 0.009$ is competitive with with latest B-Factories measurements [23].

We updated the upper limit on $B^0 \to K^+K^-$ with the same uncertainty of the current measurements [23] and on $B^0_s \to \pi^+\pi^-$ world's best upper limit, approaching the expectations from recent calculations [10, 30]. Both modes are annihilation dominated decays and they have not been observed yet. The measurement of their branching fractions is crucial because the related Feynman diagrams are hard to calculate and contribute to many relevant processes like the $\mathcal{B}(B^0_s \to K^+K^-)$.

We observed for the first time also two new baryon charmless modes $\Lambda^0_b \to p\pi^-$ and $\Lambda^0_b \to pK^-$. The measurements of their branching fractions and direct CP asymmetries can be found in [31]. In this analysis we measured only $\mathcal{B}(\Lambda^0_b \to p\pi^-)/\mathcal{B}(\Lambda^0_b \to pK^-) = 0.66 \pm 0.14 \pm 0.08$ in agreement with the current theoretical expectation [32].

Acknowledgments

We thank the Fermilab staff and the technical staffs of the participating institutions for their vital contributions. This work was supported by the U.S. Department of Energy and National Science Foundation; the Italian Istituto Nazionale di Fisica Nucleare; the Ministry of Education, Culture, Sports, Science and Technology of Japan; the Natural Sciences and Engineering Research Council of Canada; the National Science Council of the Republic of China; the Swiss National Science Foundation; the A.P. Sloan Foundation; the Bundesministerium fuer Bildung und

Forschung, Germany; the Korean Science and Engineering Foundation and the Korean Research Foundation; the Particle Physics and Astronomy Research Council and the Royal Society, UK; the Russian Foundation for Basic Research; the Comision Interministerial de Ciencia y Tecnologia, Spain; and in part by the European Community's Human Potential Programme under contract HPRN-CT-20002, Probe for New Physics.

[1] B. Aubert *et al.* (BaBar Collaboration) , Phys. Rev. Lett. **89**, 281802 (2002); B. Aubert *et al.* (BaBar Collaboration), hep-ex/0608003 submitted to Phys Rev. D; Y. Chao *et al.* (Belle Collaboration), Phys Rev. D **69**, 111102 (2004); K. Abe *et al.* (Belle Collaboration), hep-ex/0609015; A. Bornheim *et al.* (CLEO Collaboration), Phys. Rev. D **68**, 052002 (2003); B. Aubert *et al.* (BaBar Collaboration), arXiv:hep-ex/0508046; Y. Chao *et al.* (Belle Collaboration), Phys. Rev. Lett. **93**, 191802 (2004); Y. Unno (Belle Collaboration), talk presented at Moscow ICHEP 2006.
[2] M. Gronau, Phys. Lett. B **492**, 297 (2000).
[3] M. Gronau and J. L. Rosner, Phys. Lett. B **482**, 71 (2000).
[4] A. J. Buras *et al.*, Nucl. Phys. B **697**, 133 (2004).
[5] J. F. Sun, G. H. Zhu, and D. S. Du, Phys. Rev. D **68**, 054003 (2003).
[6] R. Fleischer, Phys. Lett. B **459**, 306 (1999); D. London and J. Matias, Phys. Rev. D **70**, 031502 (2004).
[7] H. J. Lipkin, Phys. Lett. B **621**, 126 (2005).
[8] B. Aubert *et al.* (BaBar Collaboration), Phys. Rev. Lett. **93**, 131801 (2004); Y. Chao *et al.* (Belle Collaboration), Phys. Rev. Lett. **93**, 191802 (2004).
[9] M. Beneke and M. Neubert, Nucl. Phys. B **675**, 333 (2003).
[10] Y. D. H. Yang, F. Su, G. R. Lu, and H. J. Hao, arXiv:hep-ph/0507326, submitted to Eur. Phys. J. C.
[11] D. Acosta *et al.* (CDF Collaboration), Phys. Rev. D**71**, 032001 (2005).
[12] A. Sill *et al.*, Nucl. Intrum. Methods **A 447**, 1 (2000).
[13] T. Affolder *et al.*, Nucl. Instrum. Methods **A 526**, 249 (2004).
[14] CDF II uses a cylindrical coordinate system in which ϕ is the azimuthal angle, r is the radius from the nominal beam line, and z points in the proton beam direction, with the origin at the center of the detector. The transverse plane is the plane perpendicular to the z axis.
[15] For a discussion of the bias in multi-component fits related to the use of multiple variables see G. Punzi, eConf **C030908**, WELT002 (2003); arXiv:physics/0401045.
[16] G. Punzi, eConf **C030908**, MODT002 (2003); arXiv:physics/0308063.
[17] W. Ashmanskas *et al.*, *"The CDF Silicon Vertex Trigger"*, Nucl. Instrum. Meth. **A518**:532 (2004), [physics/0306169].
[18] V. Cirigliano, J. F. Donoghue, and E. Golowich, Eur. Phys. J. C **18**, 83 (2000); E. Baracchini and G. Isidori, Phys. Lett. B **633**, 309 (2006).
[19] D. Acosta *et al.* (CDF Collaboration), Phys. Rev. Lett. **96**, 202001 (2006).
[20] D. Tonelli, Ph.D. Thesis, Scuola Normale Superiore, Pisa (in preparation).
[21] A. Abulencia *et al.* (CDF Collaboration), arXiv:hep-ex/0607021.
[22] I. Dunietz, R. Fleischer, and U. Nierste, Phys. Rev. D **63**, 114015 (2001).
[23] E. Barberio *et al.* [Heavy Flavor Averaging Group (HFAG)], arXiv:0704.3575 [hep-ex].
[24] We use frequentist limits based on Gaussian distribution of fit pulls (with systematics added in quadrature), and LR-ordering; see G. J. Feldman and R. D. Cousins, Phys. Rev. D **57**, 3873 (1998).
[25] A.R. Williamson, J. Zupan, Phys. Rev. D **74**, 014003 (2006).
[26] S. Descotes-Genon, J. Matias, J. Virto, Phys. Rev. Lett. **97** 061801 (2006).
[27] Seungwon Baek, D. London, J. Matias, J. Virto, hep-ph/0610109.
[28] A. Khodjamirian, T. Mannel, and M. Melcher, Phys. Rev. D **68**, 114007 (2003).
[29] W.-M. Yao *et al.* (Particle Data Group), J. Phys. G **33**, 1 (2006) and web update 2006: http://pdg.lbl.gov.
[30] Y. Li *et al.*, Phys. Rev. D **70**, 034009 (2004).
[31] Public CDF-note 9092.
`http://www-cdf.fnal.gov/physics/new/bottom/071018.blessed-ACP_Lambdab_ph/cdf9092_public_Lbph_CP-BR.ps`
[32] R.Mohanta *et al.* Phys. Rev. D **63**, 074001 (2001).

track variable	cut value
# axial COT SL	≥ 2(5 hits)
# stereo COT SL	≥ 2(5 hits)
# $r - \phi$ SVXII hits	≥ 3
$\mid \eta \mid$	≤ 1.2
p_T	≥ 2 GeV/c
$p_T(1) + p_T(2)$	≥ 5.5 GeV/c
$q(1) \cdot q(2)$	< 0
$\Delta\phi$	$\geq 20°$
$\Delta\phi$	$\leq 135°$
$\mid d_0 \mid$	≥ 100 μm
$\mid d_0 \mid$	≤ 1 mm

candidate variable	cut value
$\mid d_0(B) \mid$	≤ 140 μm
$\mid L_{xy}(B) \mid$	≥ 200 μm
$M_{\pi\pi}$	≥ 4 GeV/c^2
$M_{\pi\pi}$	≤ 7 GeV/c^2

TABLE III: Offline trigger confirmation cuts applied to the tracks and to the $B^0_{(s)} \to h^+ h^{'-}$ candidate.

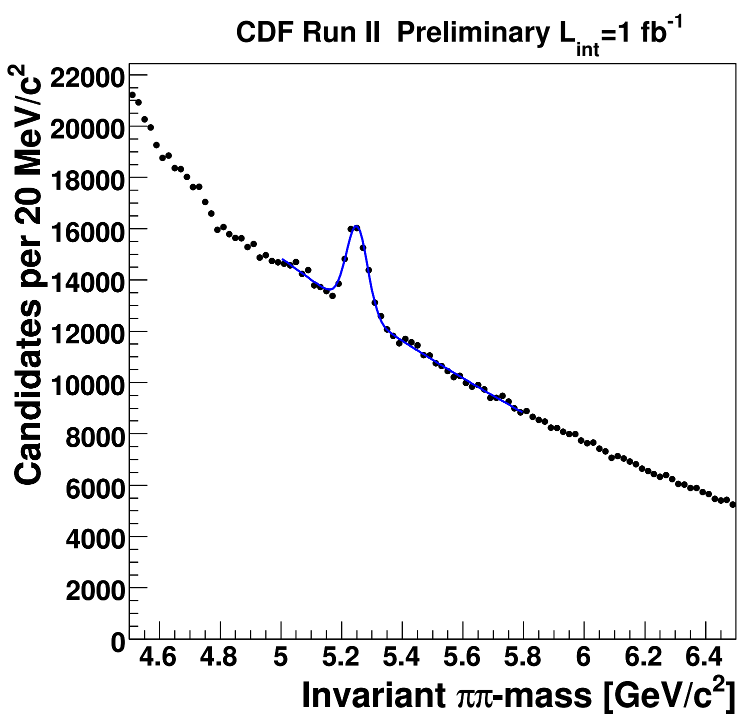

FIG. 1: Invariant $\pi\pi$-mass distribution obtained after applying only the trigger confirmation cuts. A Gaussian (signal) plus exponential (background) fit function is overlaid.

track variable	cut value
# axial COT SL	≥ 2(5 hits)
# stereo COT SL	≥ 2(5 hits)
# $r-\phi$ SVXII hits	≥ 3
tracking algorithm	sil. r-ϕ and 90°z hits
$\mid \eta \mid$	$\leq$1
p_T	$\geq$ 2 GeV/c
$p_T(1) + p_T(2)$	$\geq$ 5.5 GeV/c
$q(1) \cdot q(2)$	< 0
$\Delta\phi$	$\geq$20°
$\Delta\phi$	$\leq$135°
$\mid d_0 \mid$	$\geq$100 μm
$\mid d_0 \mid$	$\leq$ 1 mm
$d_0(1) \cdot d_0(2)$	$<$0 cm^2

candidate variable	cut value
$\mid \eta(B) \mid$	≤ 1
$\mid d_0(B) \mid$	$\leq$ 80 μm
$L_{xy}(B)$	$\geq$ 300 μm
$\chi^2_{3D}(B)$	≤ 7
isolation $I_{R=1}(B)$	≥ 0.5

TABLE IV: Cuts selection applied to the tracks and to the $B^0_{(s)} \to h^+h^{'-}$ candidate optimized for the $A_{\mathsf{CP}}(B^0 \to K^+\pi^-)$ measurement.

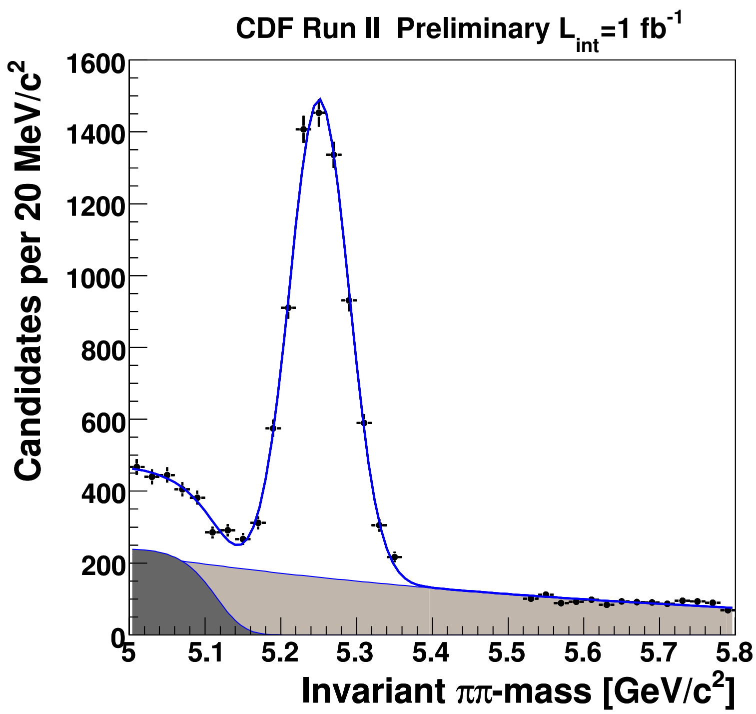

FIG. 2: Invariant $\pi\pi$-mass distribution obtained after applying the cuts optimized to measure $A_{\mathsf{CP}}(B^0 \to K^+\pi^-)$ reported in table IV. A Gaussian (signal) plus exponential (combinatoric background) plus a smeared Argus (physical background) fit function is overlaid. Since three new rare signals ($B^0_s \to K^-\pi^+$, $\Lambda^0_b \to p\pi^-$, $\Lambda^0_b \to pK^-$) are expected in the rigth tail of the peak the mass region $5.38 < m_{\pi\pi} < 5.52$ GeV/c^2 is excluded by this 1-dimensional fit.

track variable	cut value
# axial COT SL	$\geq$ 2(5 hits)
# stereo COT SL	$\geq$ 2(5 hits)
# $r-\phi$ SVXII hits	≥ 3
tracking algorithm	sil. r-ϕ and 90°z hits
$\mid \eta \mid$	$\leq$1
p_T	$\geq$ 2 GeV/c
$p_T(1) + p_T(2)$	$\geq$ 5.5 GeV/c
$q(1) \cdot q(2)$	< 0
$\Delta\phi$	$\geq$20°
$\Delta\phi$	$\leq$135°
$\mid d_0 \mid$	$\geq$100 μm
$\mid d_0 \mid$	$\leq$ 1 mm
$d_0(1) \cdot d_0(2)$	<0 cm^2

candidate variable	cut value
$\mid \eta(B) \mid$	≤ 1
$\mid d_0(B) \mid$	$\leq$ 60 μm
$L_{xy}(B)$	$\geq$ 350 μm
$\chi^2_{3D}(B)$	≤ 5
isolation $I_{R=1}(B)$	≥ 0.525

TABLE V: Cuts selection applied to the tracks and to the $B^0_{(s)} \to h^+h^{'-}$ candidate optimized for the $(f_s/f_d) \cdot \mathcal{B}(B^0_s \to K^-\pi^+)/\mathcal{B}(B^0 \to K^+\pi^-)$ measurement.

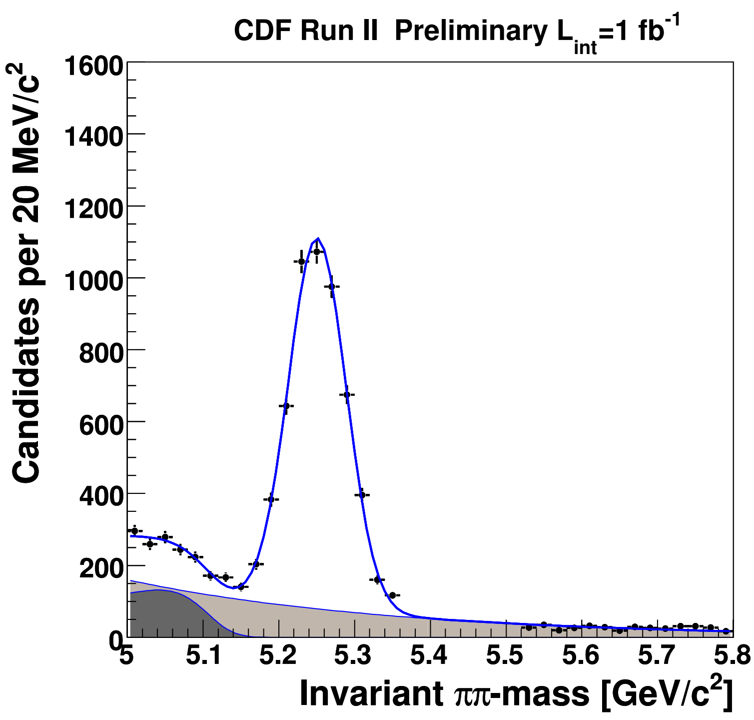

FIG. 3: Invariant $\pi\pi$-mass distribution obtained after applying the cuts optimized to measure $(f_s/f_d) \cdot \mathcal{B}(B^0_s \to K^-\pi^+)/\mathcal{B}(B^0 \to K^+\pi^-)$ reported in table V. A Gaussian (signal) plus exponential (combinatoric background) plus a smeared Argus (physical background) fit function is overlaid. Since three new rare signals ($B^0_s \to K^-\pi^+$, $\Lambda^0_b \to p\pi^-$, $\Lambda^0_b \to pK^-$) are expected in the right tail of the peak the mass region $5.38 < m_{\pi\pi} < 5.52$ GeV/c^2 is excluded by this 1-dimensional fit.

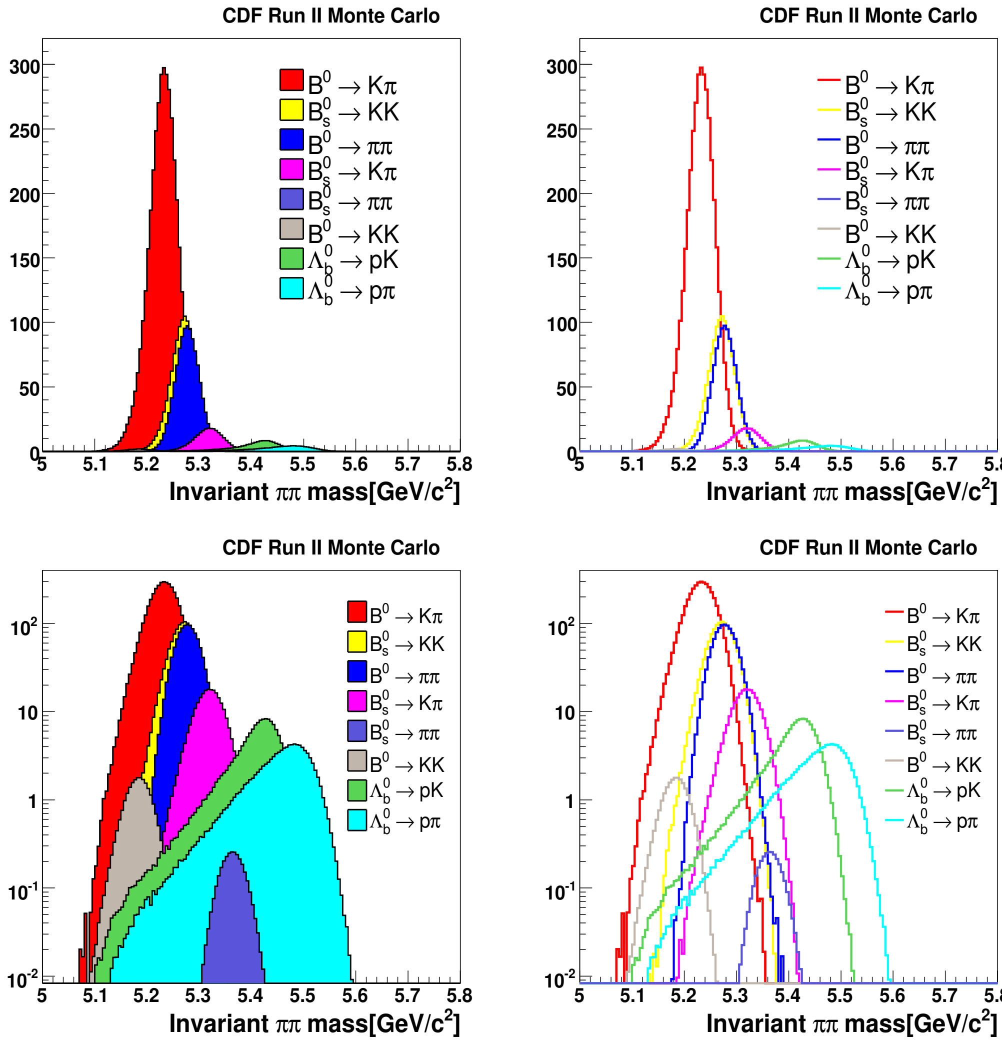

FIG. 4: Invariant $\pi\pi$-mass of the simulated $B^0_{(s)} \to h^+h^{'-}$ signals without the Final State Radiation. For this plot we used the measured branching fractions of the already observed modes ($B^0 \to \pi^+\pi^-$, $B^0 \to K^+\pi^-$ $B^0_s \to K^+K^-$) and the theoretical expected branching fractions for the not yet observed modes ($B^0 \to K^+K^-$, $B^0_s \to K^-\pi^+$, $B^0_s \to \pi^+\pi^-$, $\Lambda^0_b \to p\pi^-$, $\Lambda^0_b \to pK^-$).

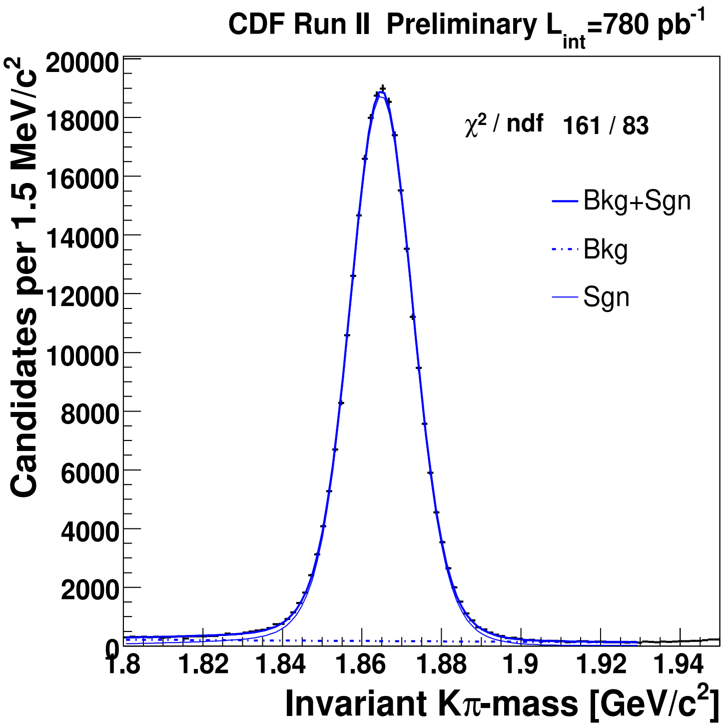

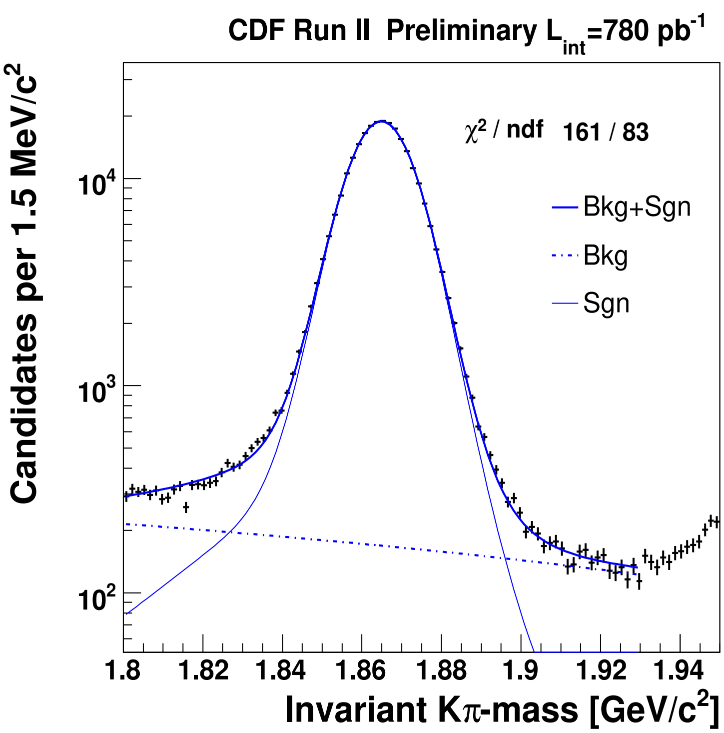

FIG. 5: Check of the mass line shape template using a sample of $D^0 \to K^-\pi^+$ decays from $D^{*+} \to D^0\pi_s^+ \to [K^-\pi^+]\pi_s^+$. We performed a 1-dimensional binned fit where the signal mass line shape is completely fixed from the model.

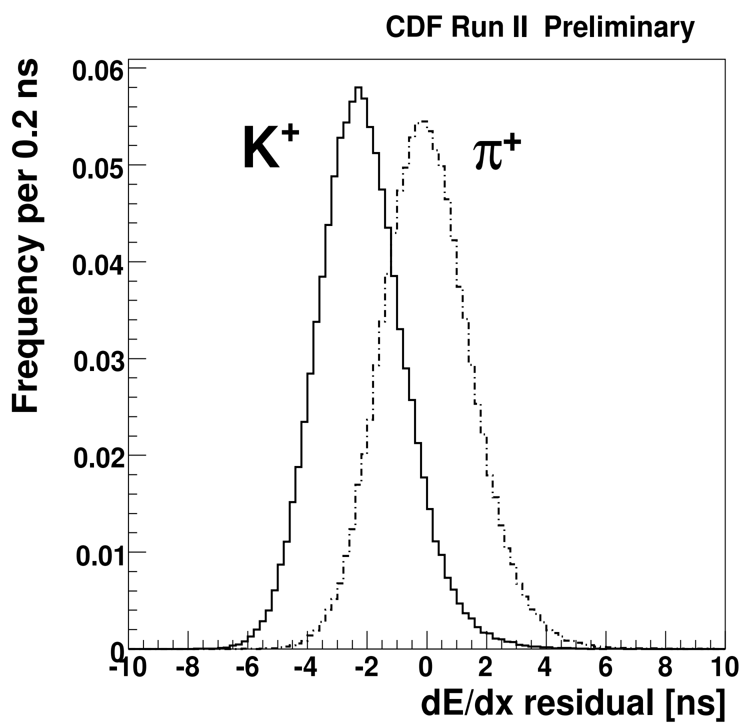

FIG. 6: Distribution of dE/dx (mean COT pulse-width) around the average pion response, for calibration samples of kaons and pions from tagged $D^{*+} \to D^0\pi_s^+ \to [K^-\pi^+]\pi_s^+$ decays. We obtain 1.4σ separation between kaons and pions over the range $2 < p_T < 10$ GeV/c, corresponding to an uncertainty on the measured fraction of each class of particles that is just 60% worse than the uncertainty attainable with ideal separation.

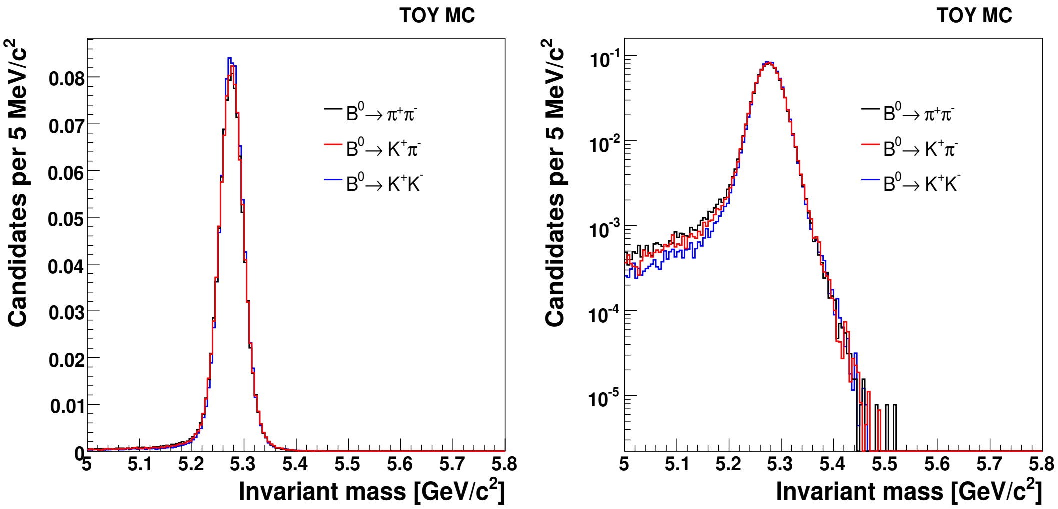

FIG. 7: Invariant mass distribution (correct mass assignment) of the simulated $B^0 \to \pi^+\pi^-$ (black) and $B^0 \to K^+\pi^-$ (red) and $B^0 \to K^+K^-$ (blue) events. On the left linear scale, on the right logarithmic scale.

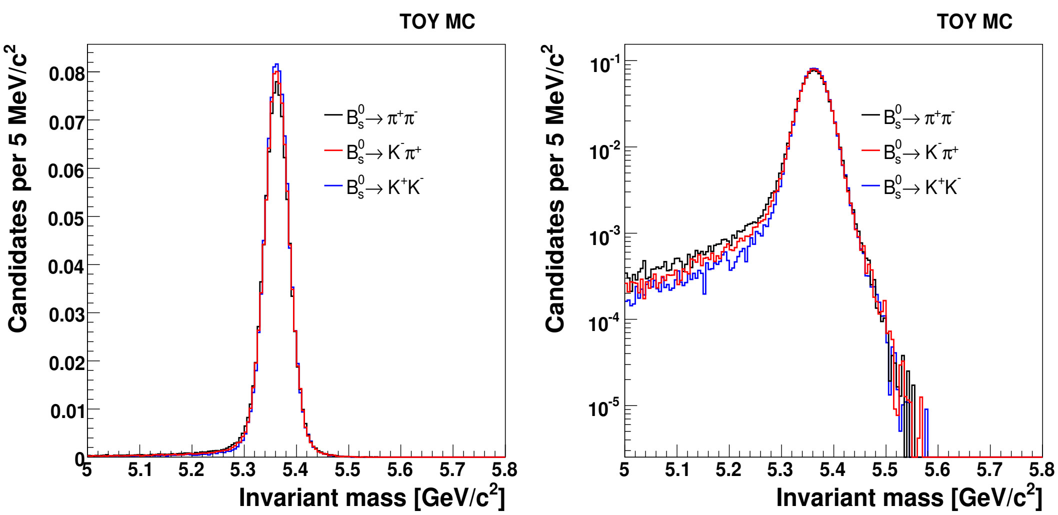

FIG. 8: Invariant mass distribution (correct mass assignment) of the simulated $B_s^0 \to \pi^+\pi^-$ (black) and $B_s^0 \to K^-\pi^+$ (red) and $B_s^0 \to K^+K^-$ (blue) events. On the left linear scale, on the right logarithmic scale.

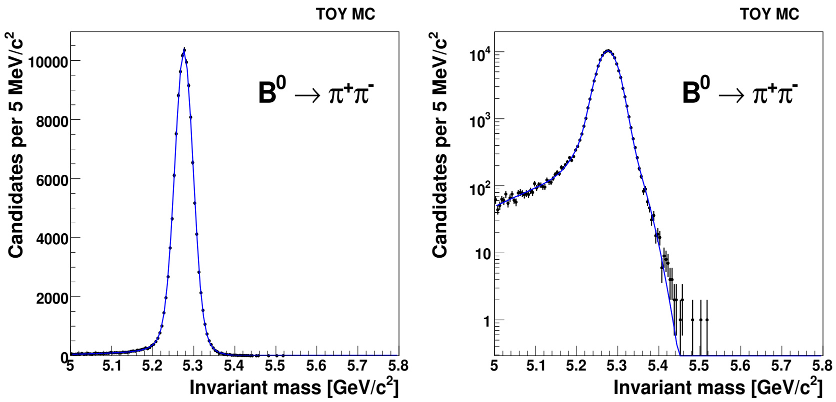

FIG. 9: Invariant mass distribution (correct mass assignment) of the simulated $B^0 \to \pi^+\pi^-$ events (on the left: linear scale, on the right: logarithmic scale on Y axis). We overlaided the mass template.

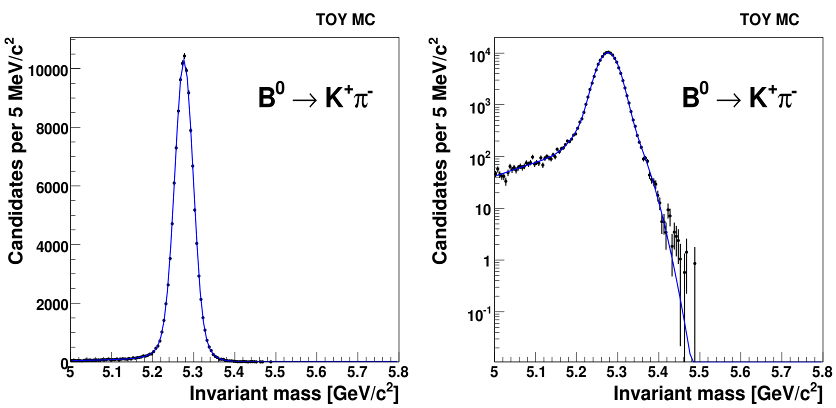

FIG. 10: Invariant mass distribution (correct mass assignment) of the simulated $B^0 \to K^+\pi^-$ events (on the left: linear scale, on the right: logarithmic scale on Y axis). We overlaided the mass template.

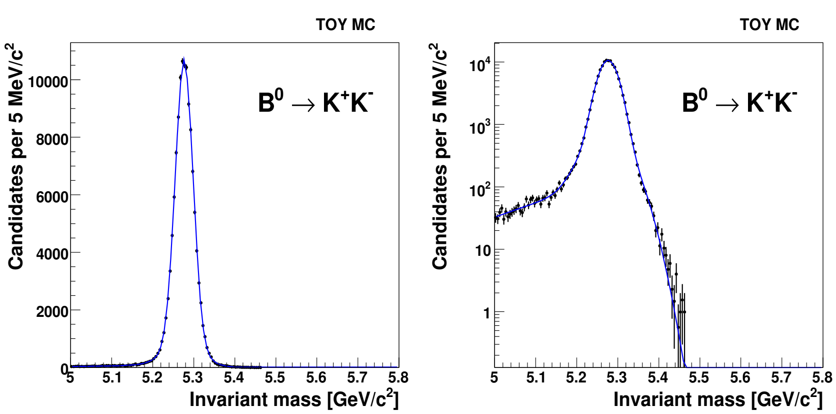

FIG. 11: Invariant mass distribution (correct mass assignment) of the simulated $B^0 \to K^+K^-$ events (on the left: linear scale, on the right: logarithmic scale on Y axis). We overlaided the mass template.

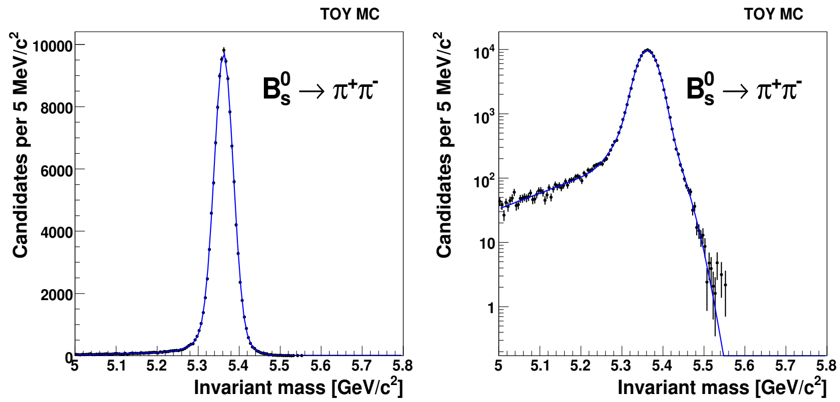

FIG. 12: Invariant mass distribution (correct mass assignment) of the simulated $B_s^0 \to \pi^+\pi^-$ events (on the left: linear scale, on the right: logarithmic scale on Y axis). We overlaided the mass template.

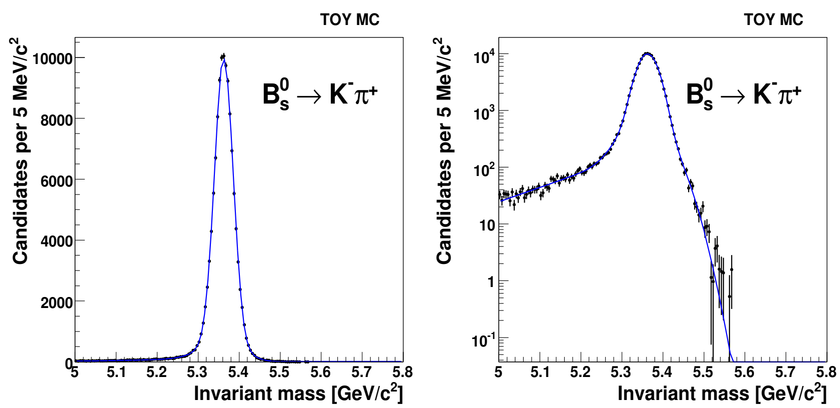

FIG. 13: Invariant mass distribution (correct mass assignment) of the simulated $B_s^0 \to K^-\pi^+$ events (on the left: linear scale, on the right: logarithmic scale on Y axis). We overlaided the mass template.

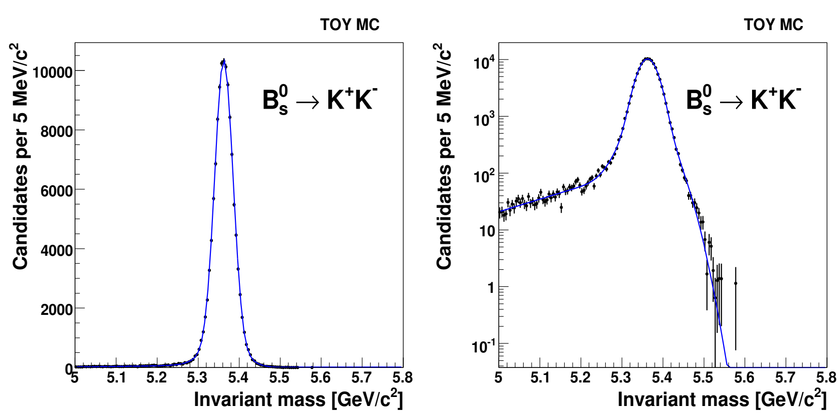

FIG. 14: Invariant mass distribution (correct mass assignment) of the simulated $B_s^0 \to K^+K^-$ events (on the left: linear scale, on the right: logarithmic scale on Y axis). We overlaided the mass template.

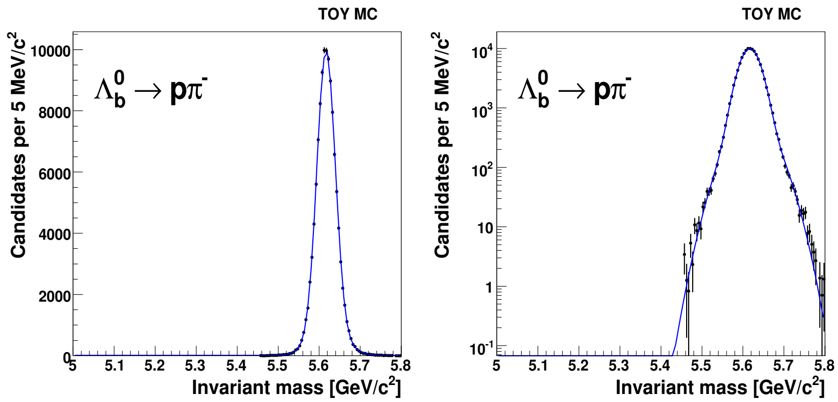

FIG. 15: Invariant mass distribution (correct mass assignment) of the simulated $\Lambda_b^0 \to p\pi^-$ events (on the left: linear scale, on the right: logarithmic scale on Y axis). We overlaided the mass template.

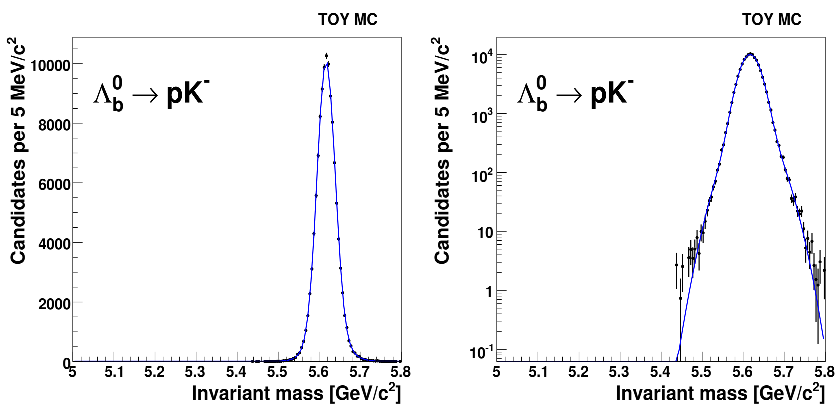

FIG. 16: Invariant mass distribution (correct mass assignment) of the simulated $\Lambda_b^0 \to pK^-$ events (on the left: linear scale, on the right: logarithmic scale on Y axis). We overlaided the mass template.

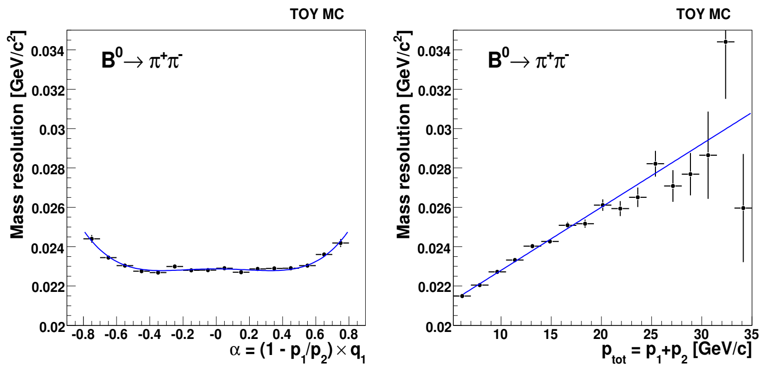

FIG. 17: Dependence of the mass resolution on the momentum for the $B^0 \to \pi^+\pi^-$ mode. On the left: mass resolution versus α parameterized with a fourth order degree polynomial (pol4), even terms are fixed to 0. On the right: mass resolution versus p_{tot} parameterized with a first order degree polynomial (pol1).

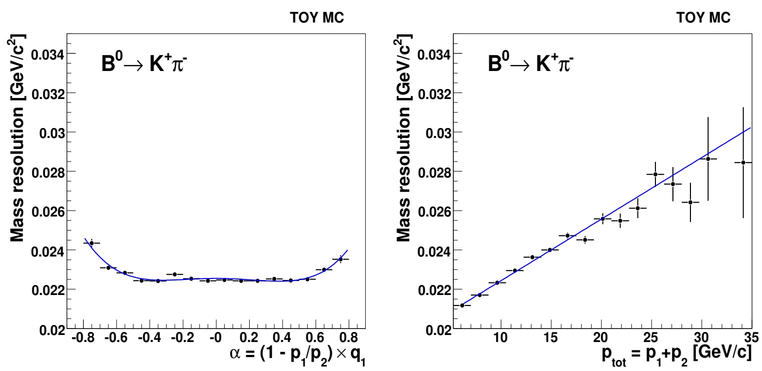

FIG. 18: Dependence of the mass resolution on the momentum for the $B^0 \to K^+\pi^-$ mode. On the left: mass resolution versus α parameterized with a fourth order degree polynomial (pol4). On the right: mass resolution versus p_{tot} parameterized with a first order degree polynomial (pol1).

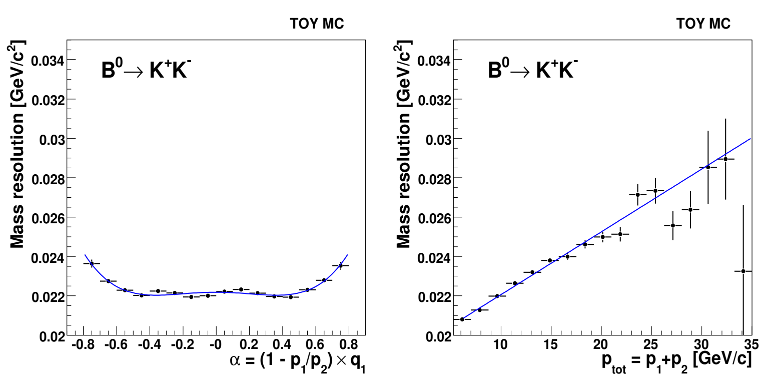

FIG. 19: Dependence of the mass resolution on the momentum for the $B^0 \to K^+K^-$ mode. On the left: mass resolution versus α parameterized with a fourth order degree polynomial (pol4), even terms are fixed to 0. On the right: mass resolution versus p_{tot} parameterized with a first order degree polynomial (pol1).

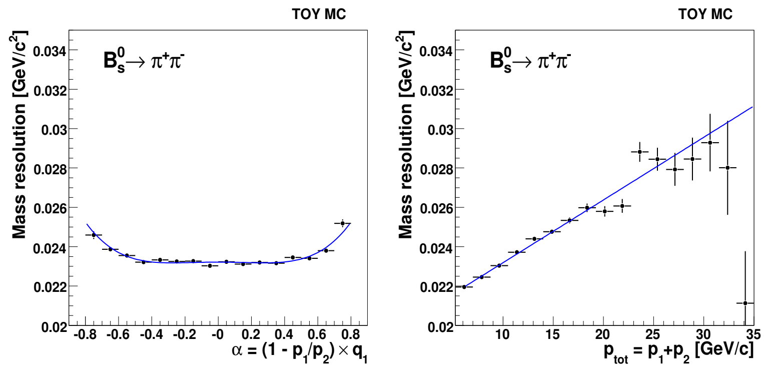

FIG. 20: Dependence of the mass resolution on the momentum for the $B_s^0 \to \pi^+\pi^-$ mode. On the left: mass resolution versus α parameterized with a fourth order degree polynomial (pol4), even terms are fixed to 0. On the right: mass resolution versus p_{tot} parameterized with a first order degree polynomial (pol1).

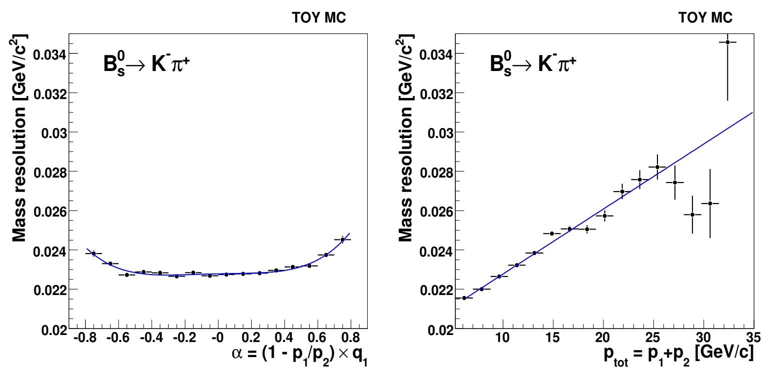

FIG. 21: Dependence of the mass resolution on the momentum for the $B_s^0 \to K^-\pi^+$ mode. On the left: mass resolution versus α parameterized with a fourth order degree polynomial (pol4). On the right: mass resolution versus p_{tot} parameterized with a first order degree polynomial (pol1).

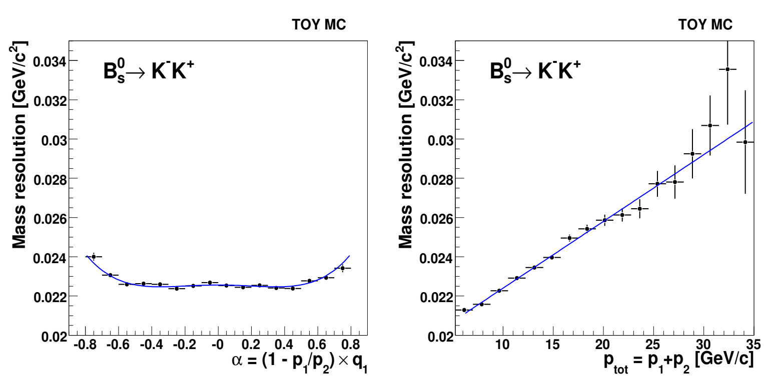

FIG. 22: Dependence of the mass resolution on the momentum for the $B_s^0 \to K^+K^-$ mode. On the left: mass resolution versus α parameterized with a fourth order degree polynomial (pol4), even terms are fixed to 0. On the right: mass resolution versus p_{tot} parameterized with a first order degree polynomial (pol1).

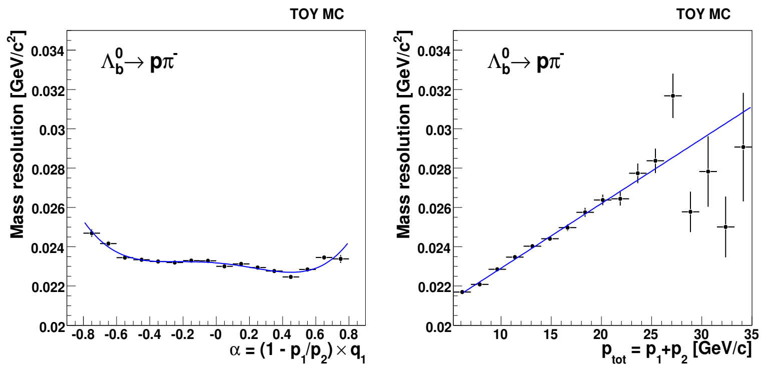

FIG. 23: Dependence of the mass resolution on the momentum for the $\Lambda_b^0 \to p\pi^-$ mode. On the left: mass resolution versus α parameterized with a fourth order degree polynomial (pol4). On the right: mass resolution versus p_{tot} parameterized with a first order degree polynomial (pol1).

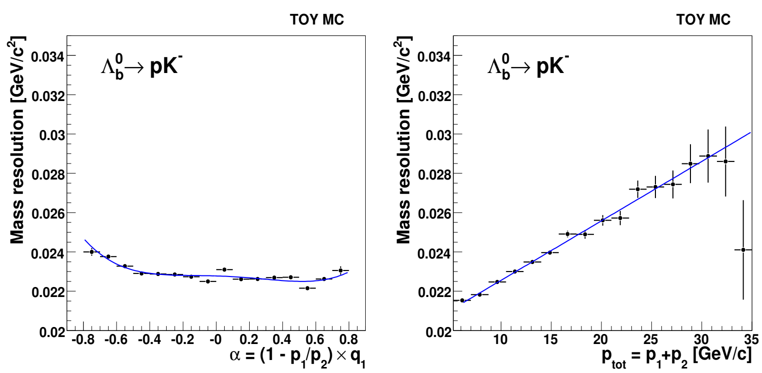

FIG. 24: Dependence of the mass resolution on the momentum for the $\Lambda_b^0 \to pK^-$ mode. On the left: mass resolution versus α parameterized with a fourth order degree polynomial (pol4). On the right: mass resolution versus p_{tot} parameterized with a first order degree polynomial (pol1).

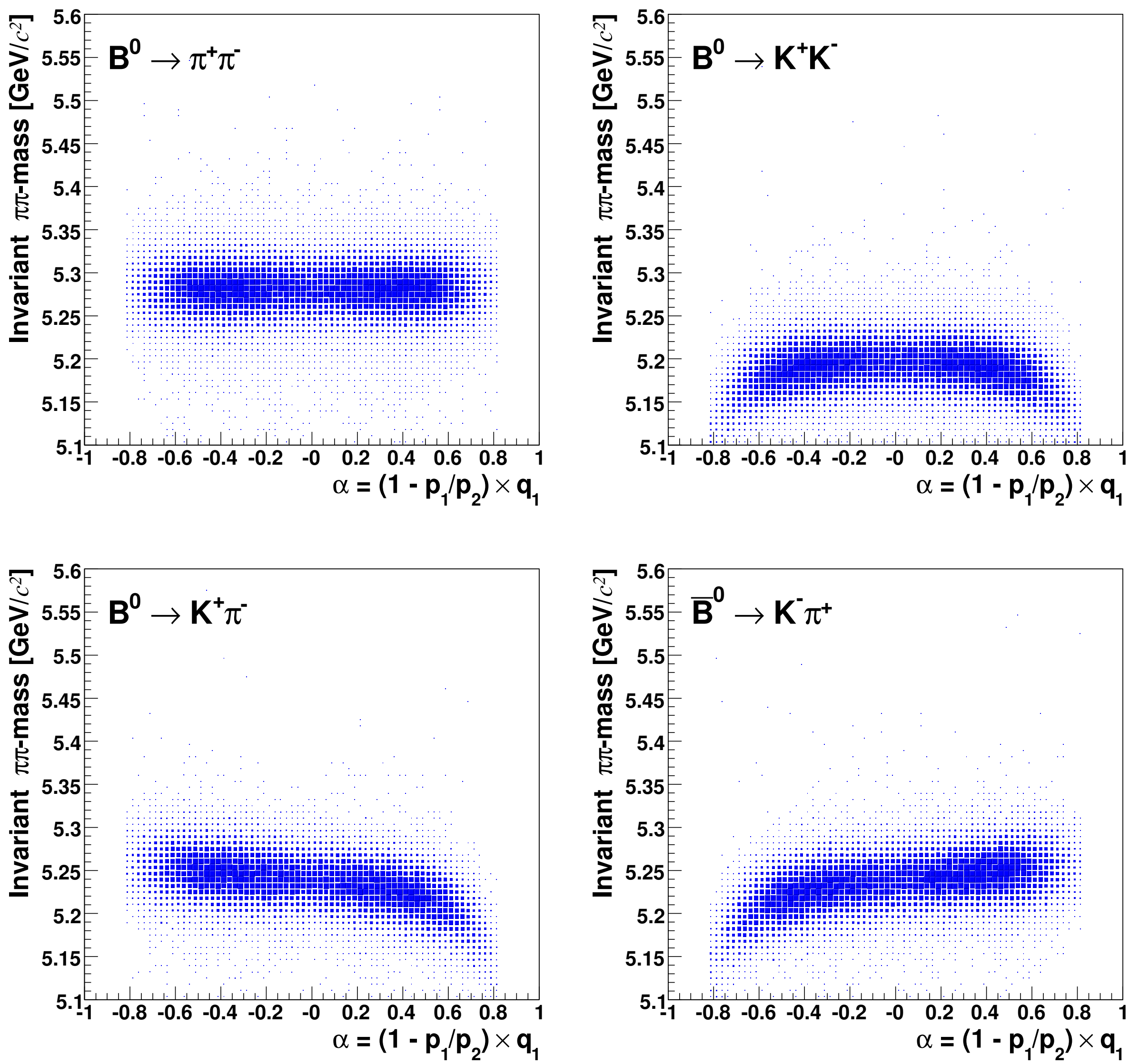

FIG. 25: $m_{\pi\pi}$ distribution of the $B^0 \to \pi^+\pi^-$, $B^0 \to K^+K^-$, $B^0 \to K^+\pi^-$, $\overline{B}^0 \to K^-\pi^+$signals as a function of α (Monte Carlo).

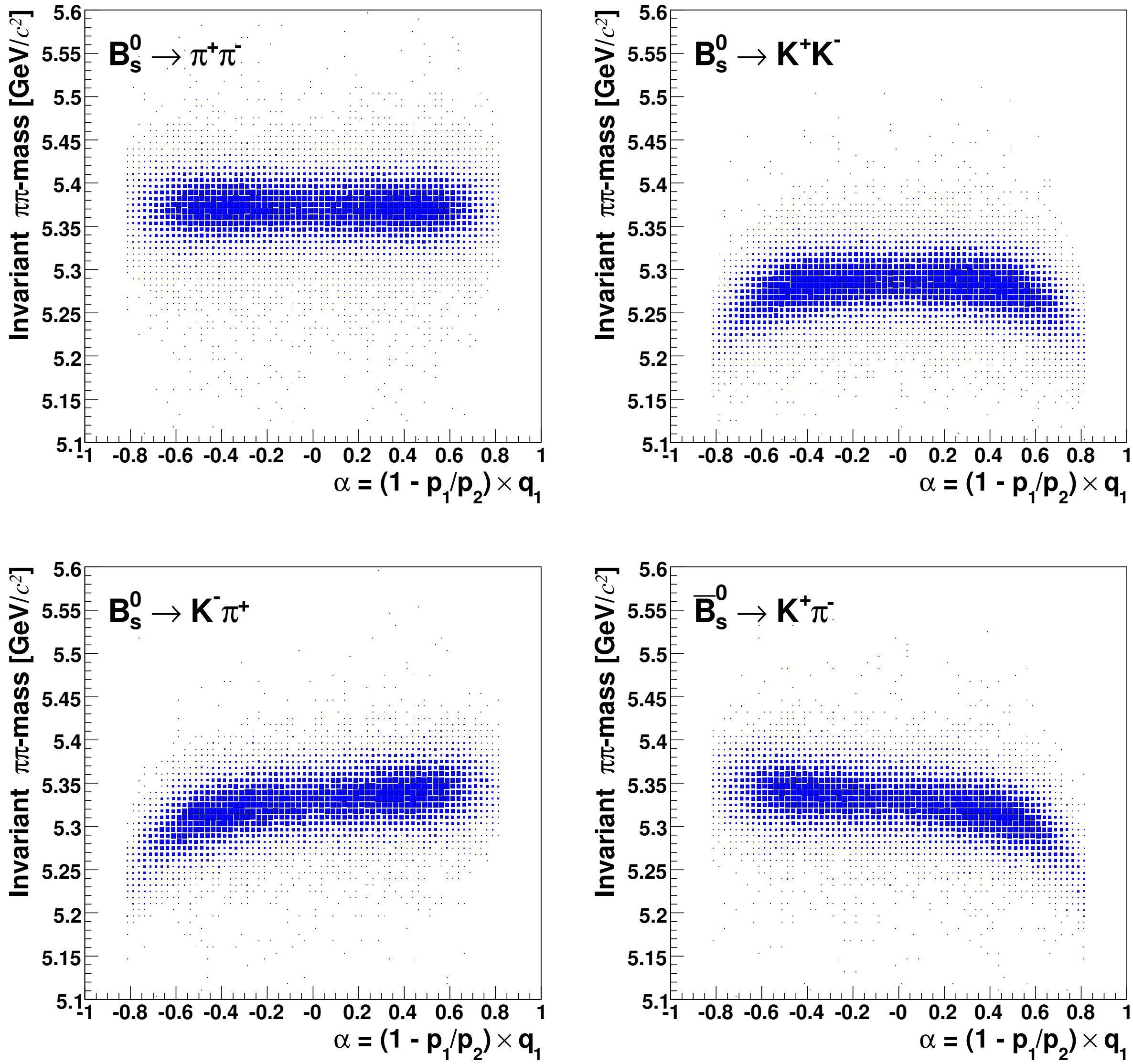

FIG. 26: $m_{\pi\pi}$ distribution of the $B_s^0 \to \pi^+\pi^-$, $B_s^0 \to K^+K^-$, $B_s^0 \to K^-\pi^+$, $\overline{B}_s^0 \to K^+\pi^-$signals as a function of α (Monte Carlo).

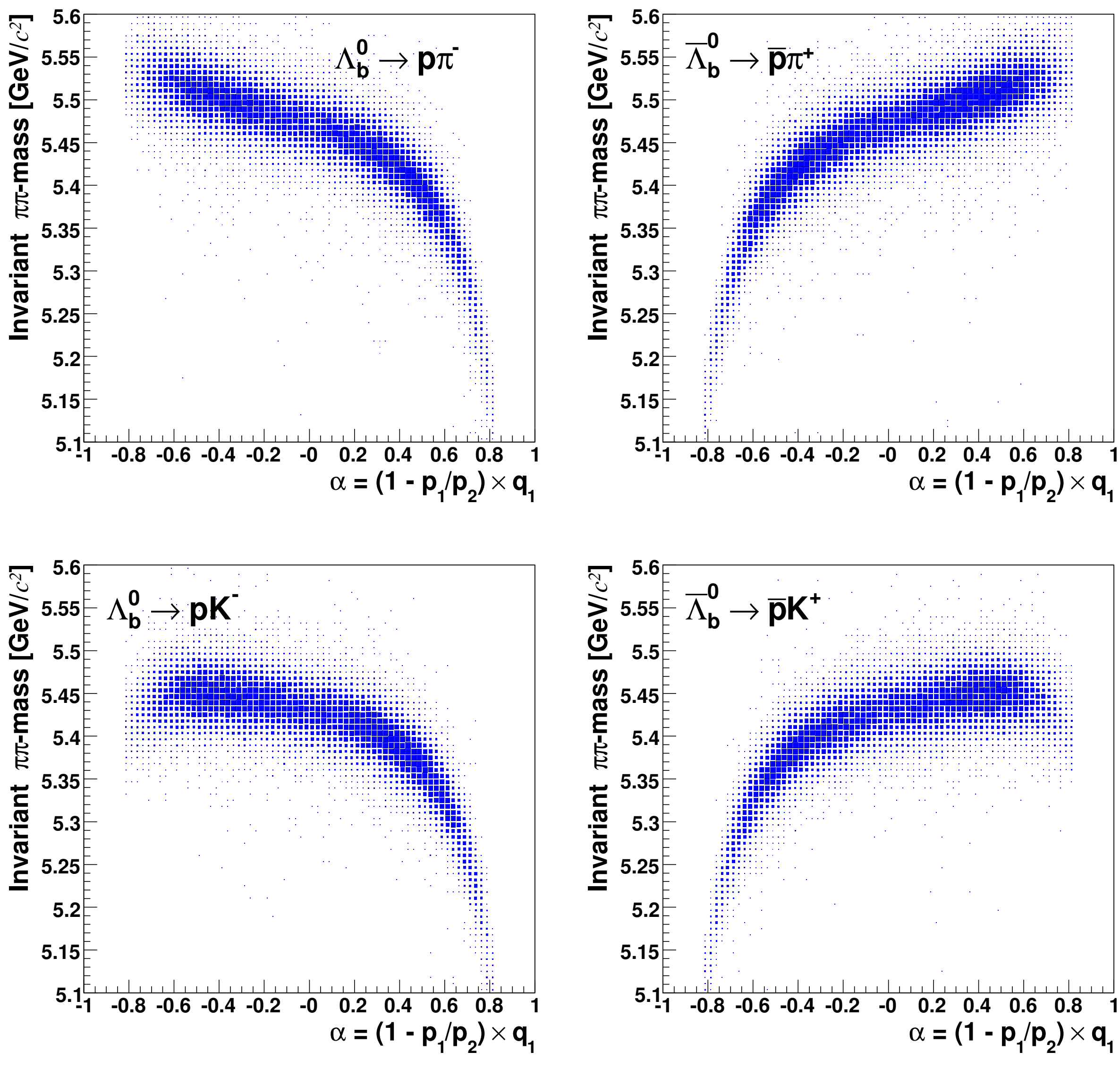

FIG. 27: $m_{\pi\pi}$ distribution of the $\Lambda_b^0 \to p\pi^-$, $\overline{\Lambda}_b^0 \to \overline{p}\pi^+$, $\Lambda_b^0 \to pK^-$, $\overline{\Lambda}_b^0 \to \overline{p}K^+$signals as a function of α (Monte Carlo).

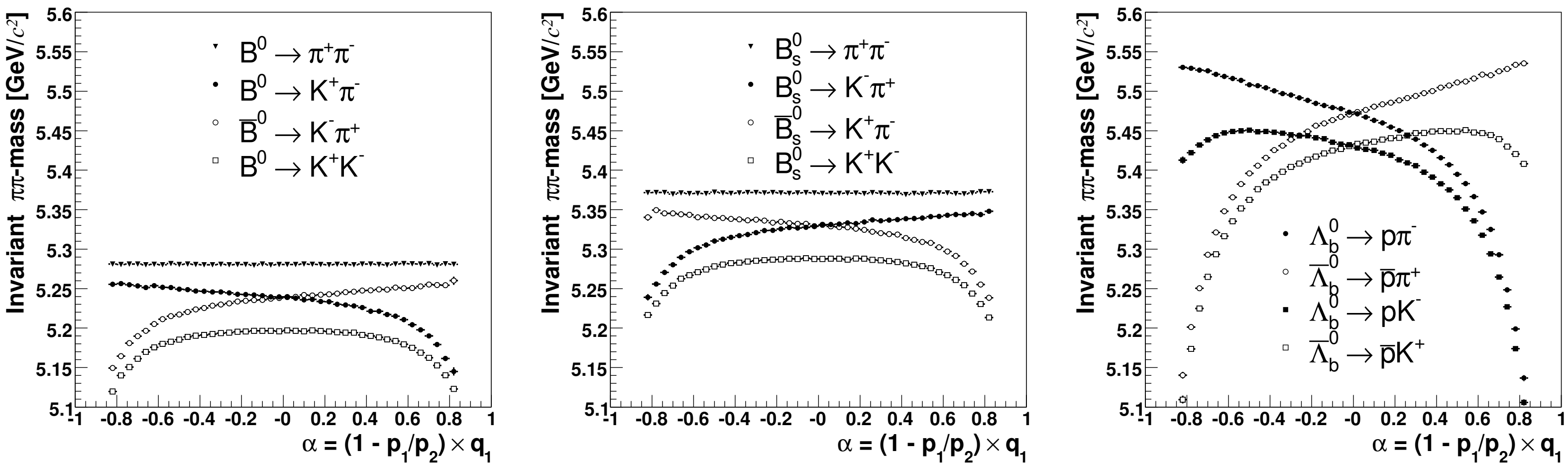

FIG. 28: Averaged $m_{\pi\pi}$ distribution of the $B^0_{(s)} \to h^+ h^{'-}$ and $\Lambda^0_b \to p h^-$ signals as a function of α (Monte Carlo).

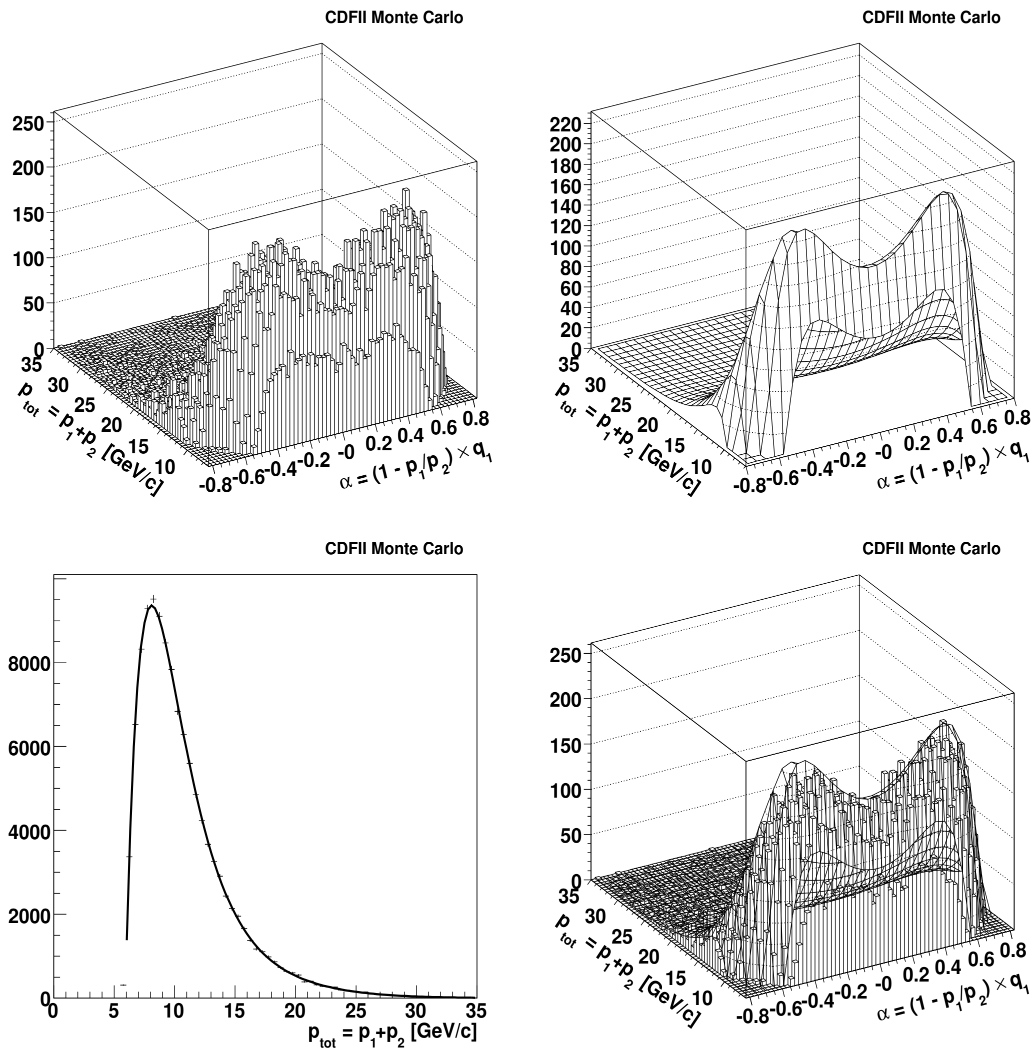

FIG. 29: Determination of the joint (α, p_{tot}) density for the mode $B^0 \rightarrow \pi^+\pi^-$. Top left plot: distribution of $\alpha - p_{tot}$ in simulated events. Top right plot: fit results. Bottom left plot: result of the fit of the p_{tot} distribution. Bottom right plot: result of the two-dimensional fit overlaid to the distribution of Monte Carlo.

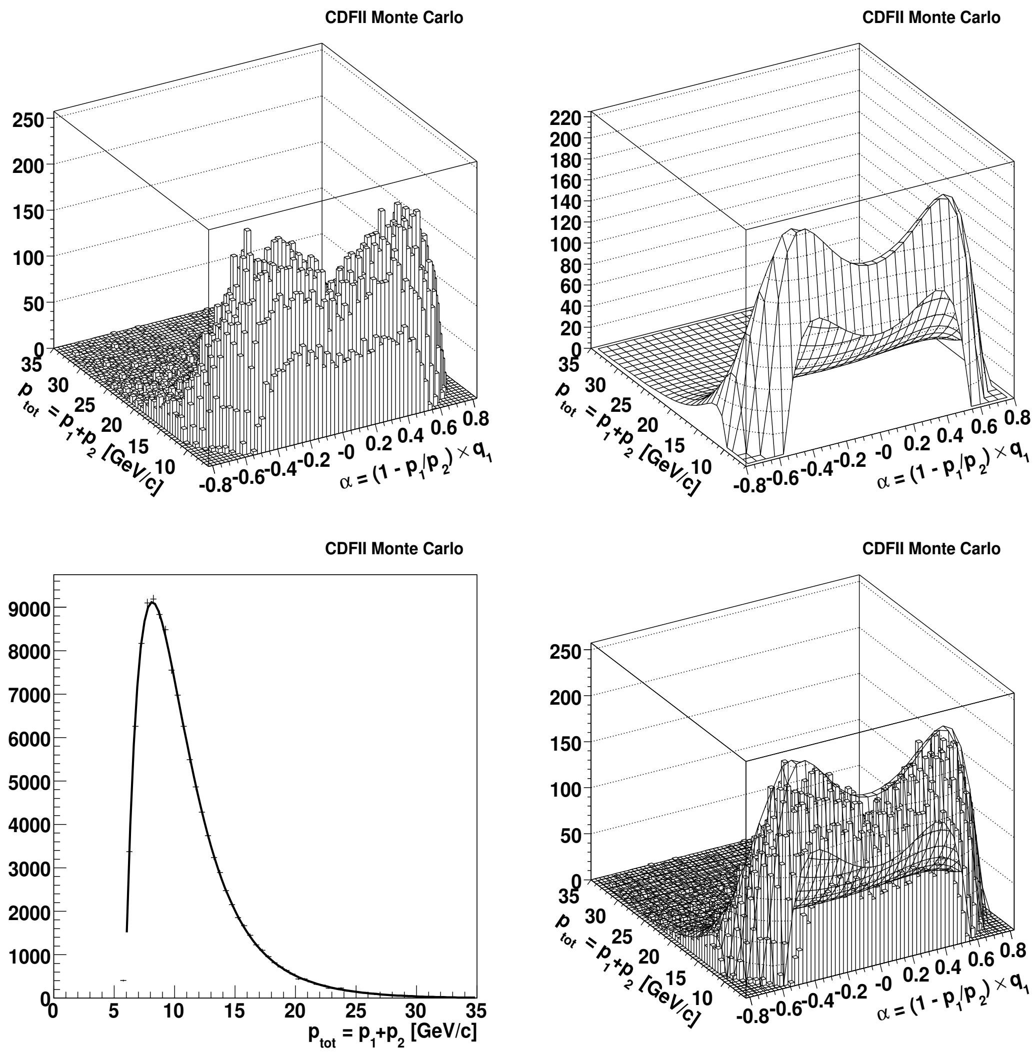

FIG. 30: Determination of the joint (α, p_{tot}) density for the mode $B^0 \to K^+\pi^-$. Top left plot: distribution of $\alpha - p_{tot}$ in simulated events. Top right plot: fit results. Bottom left plot: result of the fit of the p_{tot} distribution. Bottom right plot: result of the two-dimensional fit overlaid to the distribution of Monte Carlo.

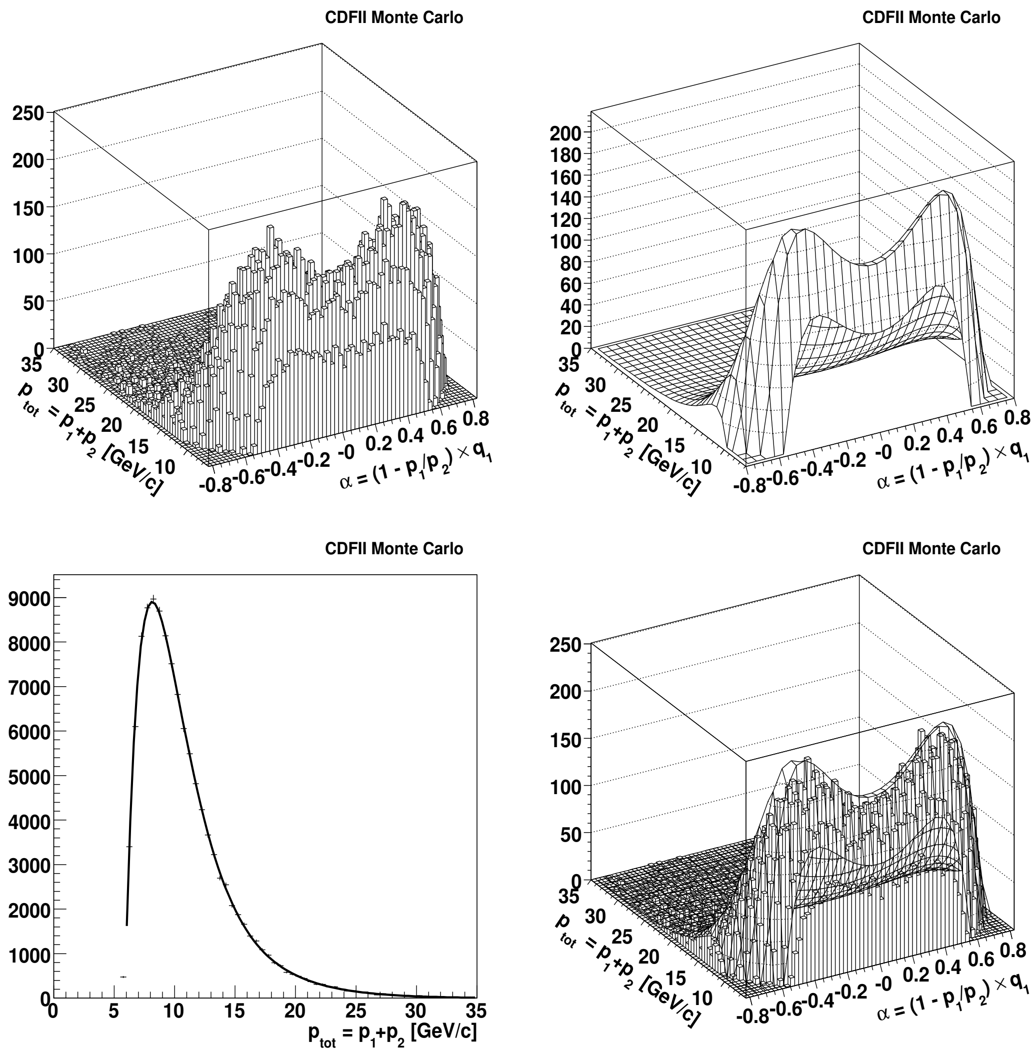

FIG. 31: Determination of the joint (α, p_{tot}) density for the mode $B^0 \to K^+K^-$. Top left plot: distribution of $\alpha - p_{tot}$ in simulated events. Top right plot: fit results. Bottom left plot: result of the fit of the p_{tot} distribution. Bottom right plot: result of the two-dimensional fit overlaid to the distribution of Monte Carlo.

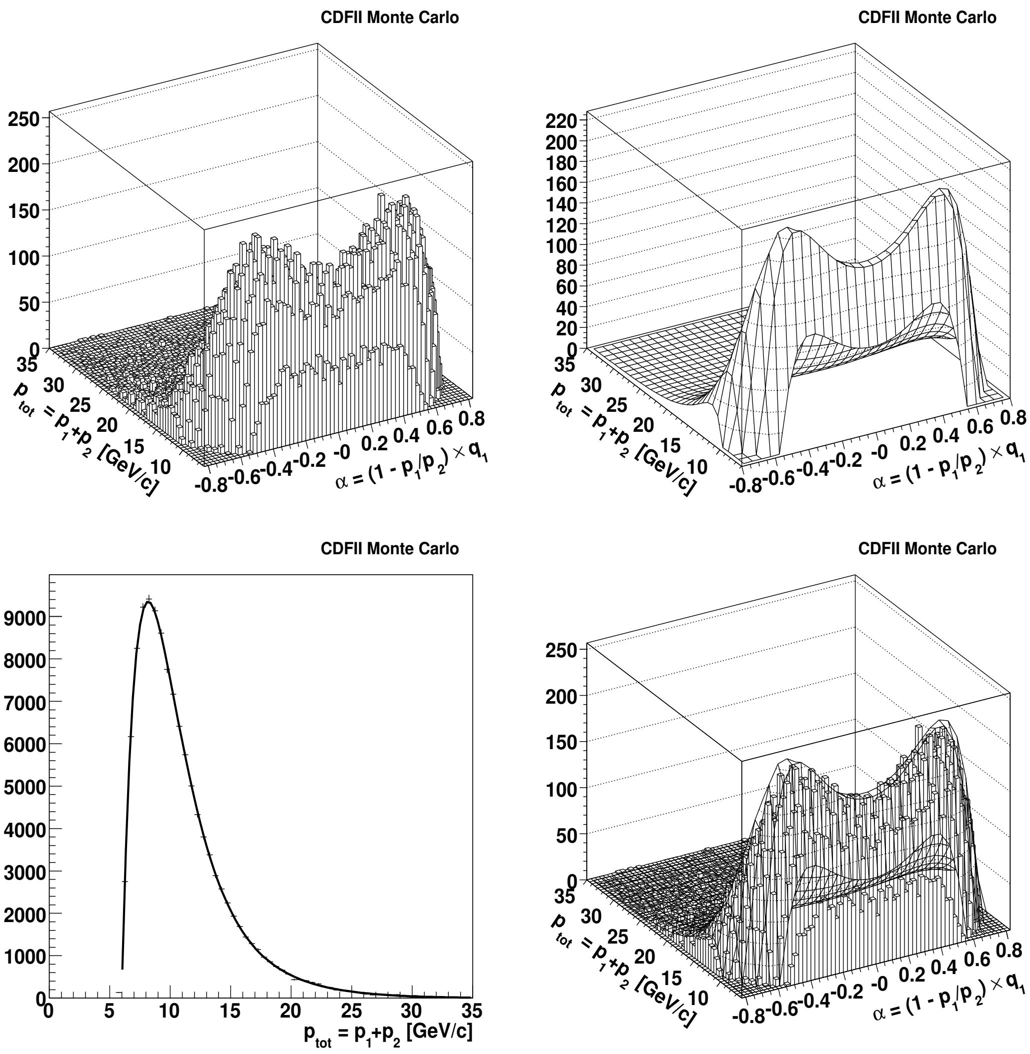

FIG. 32: Determination of the joint (α, p_{tot}) density for the mode $B_s^0 \to \pi^+\pi^-$. Top left plot: distribution of $\alpha - p_{tot}$ in simulated events. Top right plot: fit results. Bottom left plot: result of the fit of the p_{tot} distribution. Bottom right plot: result of the two-dimensional fit overlaid to the distribution of Monte Carlo.

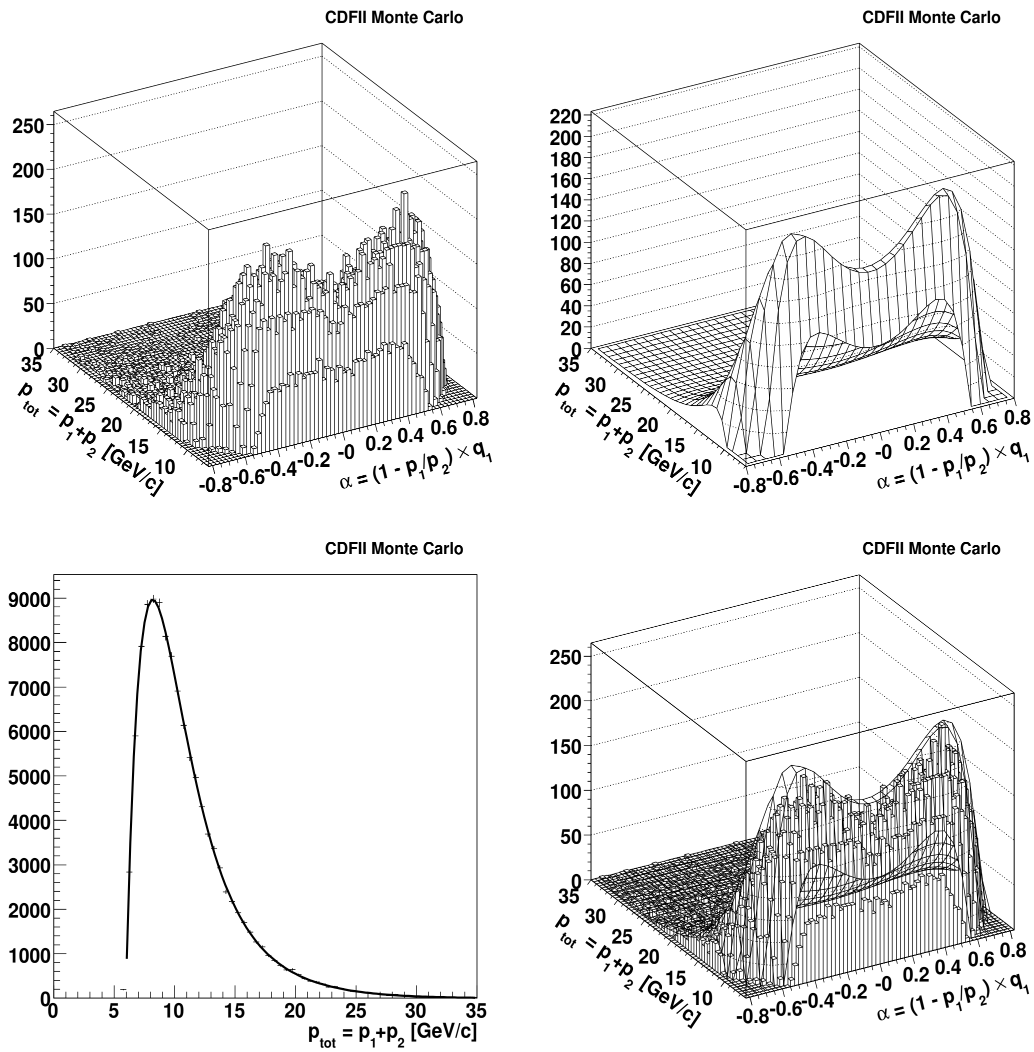

FIG. 33: Determination of the joint (α, p_{tot}) density for the mode $B_s^0 \to K^-\pi^+$. Top left plot: distribution of $\alpha - p_{tot}$ in simulated events. Top right plot: fit results. Bottom left plot: result of the fit of the p_{tot} distribution. Bottom right plot: result of the two-dimensional fit overlaid to the distribution of Monte Carlo.

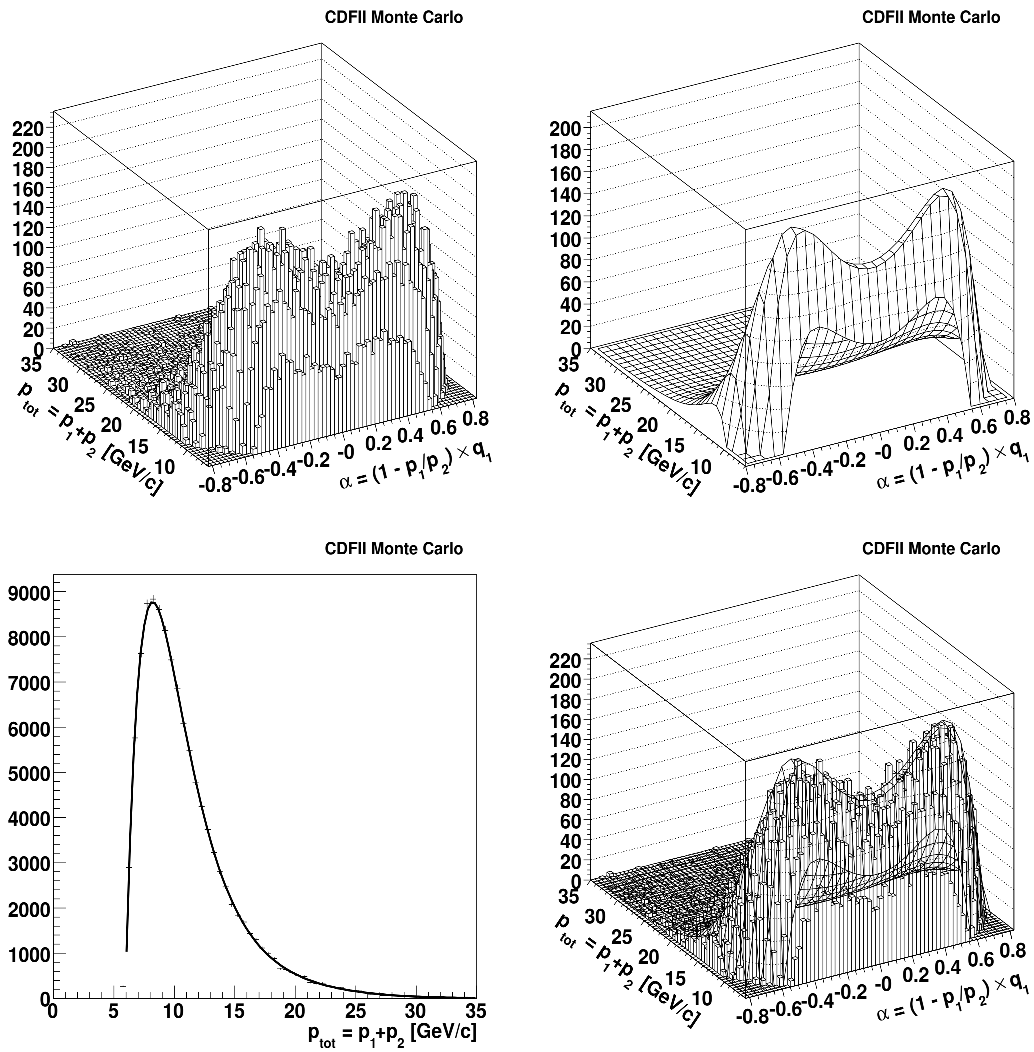

FIG. 34: Determination of the joint (α, p_{tot}) density for the mode $B_s^0 \to K^+K^-$. Top left plot: distribution of $\alpha - p_{tot}$ in simulated events. Top right plot: fit results. Bottom left plot: result of the fit of the p_{tot} distribution. Bottom right plot: result of the two-dimensional fit overlaid to the distribution of Monte Carlo.

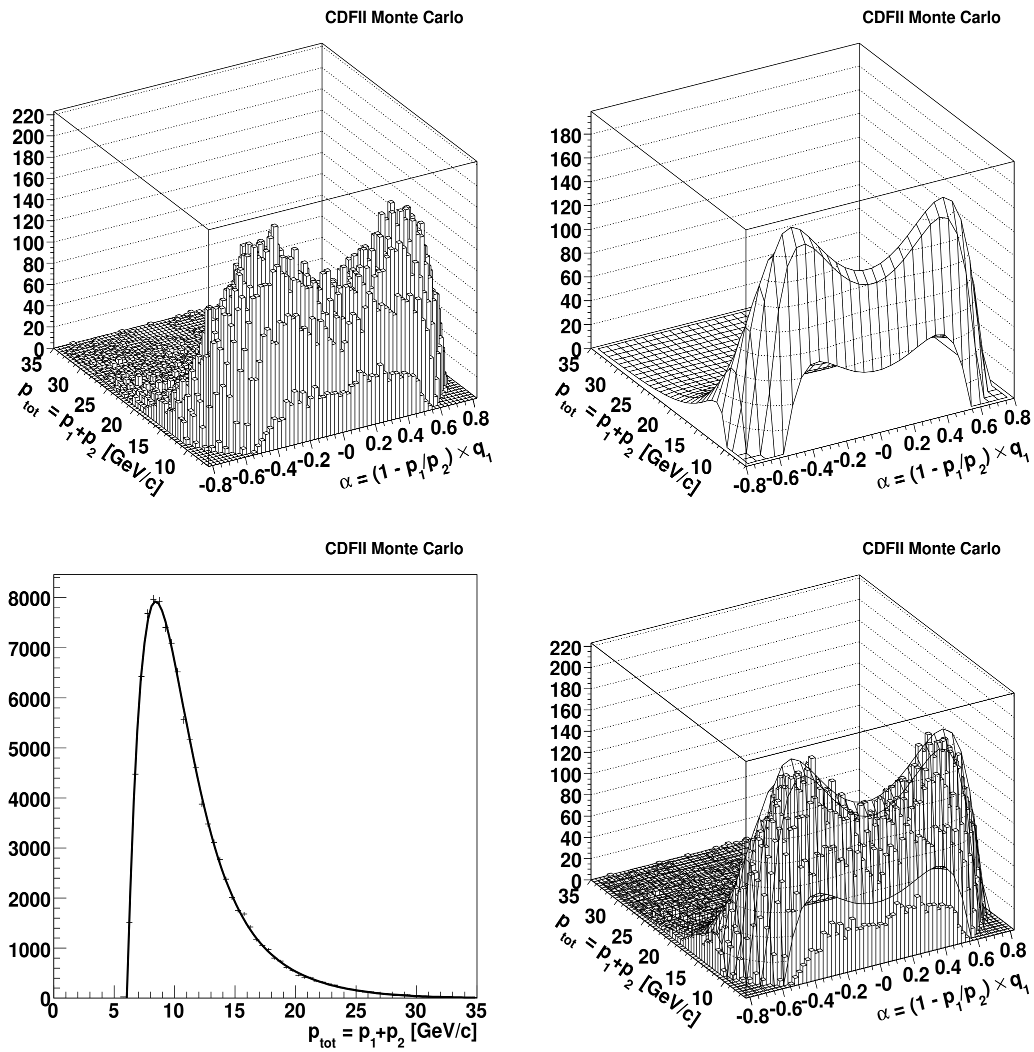

FIG. 35: Determination of the joint (α, p_{tot}) density for the mode $\Lambda_b^0 \to p\pi^-$. Top left plot: distribution of $\alpha - p_{tot}$ in simulated events. Top right plot: fit results. Bottom left plot: result of the fit of the p_{tot} distribution. Bottom right plot: result of the two-dimensional fit overlaid to the distribution of Monte Carlo.

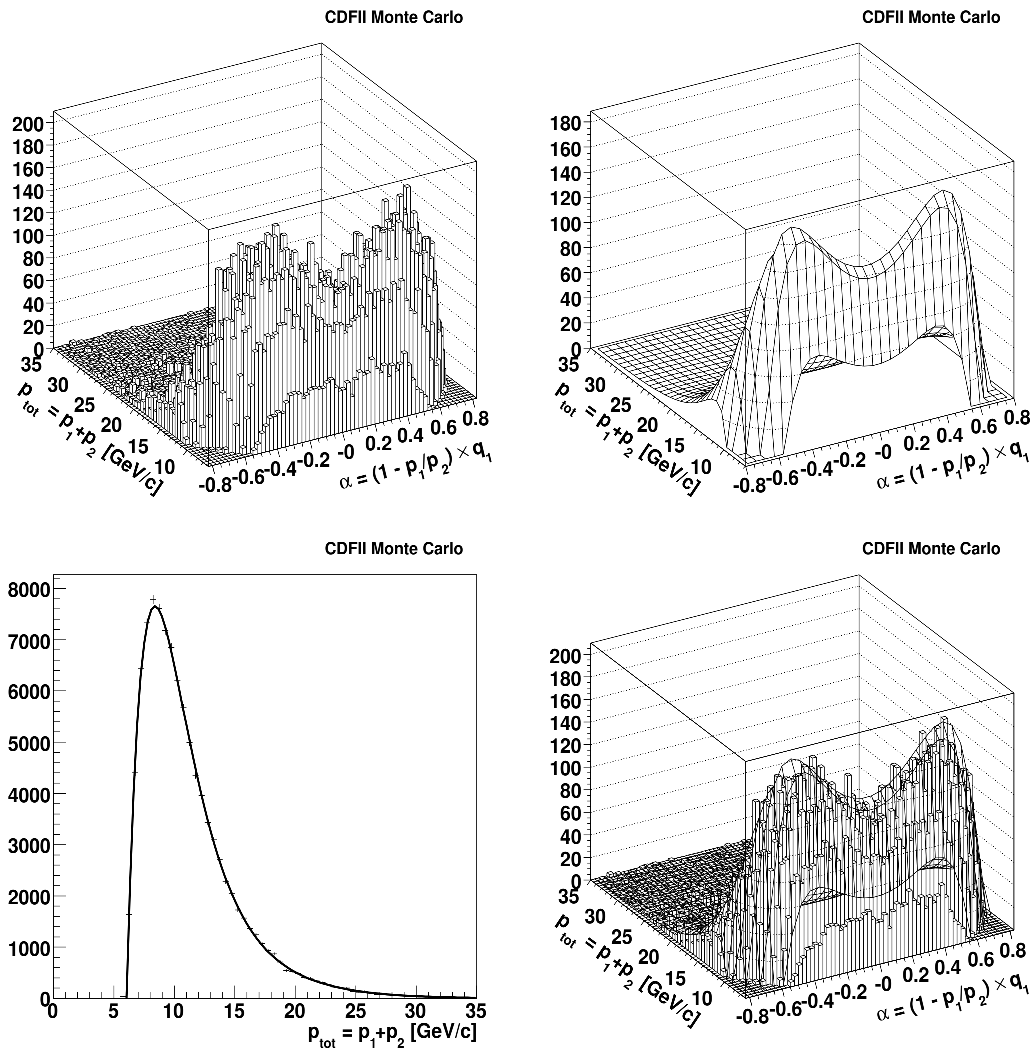

FIG. 36: Determination of the joint (α, p_{tot}) density for the mode $\Lambda_b^0 \to pK^-$. Top left plot: distribution of $\alpha - p_{tot}$ in simulated events. Top right plot: fit results. Bottom left plot: result of the fit of the p_{tot} distribution. Bottom right plot: result of the two-dimensional fit overlaid to the distribution of Monte Carlo.

mode	fraction	yield	observable	fit result
$B^0 \to \pi^+\pi^- + \overline{B}^0 \to \pi^+\pi^-$	(0.160 ± 0.009)	1121 ± 63	$\frac{N_{\rm raw}(B^0\to\pi^+\pi^-)}{N_{\rm raw}(B^0\to K^+\pi^-)}$	0.277 ± 0.018
$B^0 \to K^+\pi^- + \overline{B}^0 \to K^-\pi^+$	(0.577 ± 0.010)	4045 ± 84	$\frac{N_{\rm raw}(\overline{B}^0\to K^-\pi^+)-N_{\rm raw}(B^0\to K^+\pi^-)}{N_{\rm raw}(\overline{B}^0\to K^-\pi^+)+N_{\rm raw}(B^0\to K^+\pi^-)}$	-0.092 ± 0.023
$B^0 \to K^+\pi^-$	(0.315 ± 0.009)	2209 ± 64		
$\overline{B}^0 \to K^-\pi^+$	(0.262 ± 0.008)	1836 ± 62		
$B_s^0 \to K^-\pi^+ + \overline{B}_s^0 \to K^+\pi^-$	(0.035 ± 0.006)	247 ± 45	$\frac{N_{\rm raw}(B_s^0\to K^-\pi^+)}{N_{\rm raw}(B^0\to K^+\pi^-)}$	0.061 ± 0.011
$B_s^0 \to K^-\pi^+$	(0.009 ± 0.004)	64 ± 30	$\frac{N_{\rm raw}(\overline{B}_s^0\to K^+\pi^-)-N_{\rm raw}(B_s^0\to K^-\pi^+)}{N_{\rm raw}(\overline{B}_s^0\to K^+\pi^-)+N_{\rm raw}(B_s^0\to K^-\pi^+)}$	0.48 ± 0.19
$\overline{B}_s^0 \to K^+\pi^-$	(0.026 ± 0.005)	183 ± 34	$\frac{N_{\rm raw}(\overline{B}^0\to K^-\pi^+)-N_{\rm raw}(B^0\to K^+\pi^-)}{N_{\rm raw}(\overline{B}_s^0\to K^+\pi^-)-N_{\rm raw}(B_s^0\to K^-\pi^+)}$	-3.13 ± 1.43
$B_s^0 \to K^+K^- + \overline{B}_s^0 \to K^+K^-$	(0.186 ± 0.009)	1307 ± 64	$\frac{N_{\rm raw}(B_s^0\to K^+K^-)}{N_{\rm raw}(B^0\to K^+\pi^-)}$	0.323 ± 0.019
$B_s^0 \to \pi^+\pi^- + \overline{B}_s^0 \to \pi^+\pi^-$	(0.0004 ± 0.003)	3 ± 22	$\frac{N_{\rm raw}(B_s^0\to\pi^+\pi^-)}{N_{\rm raw}(B^0\to K^+\pi^-)}$	0.0007 ± 0.005
$B^0 \to K^+K^- + \overline{B}^0 \to K^+K^-$	(0.003 ± 0.004)	22 ± 31	$\frac{N_{\rm raw}(B^0\to K^+K^-)}{N_{\rm raw}(B^0\to K^+\pi^-)}$	0.005 ± 0.008
$\Lambda_b^0 \to pK^- + \overline{\Lambda}_b^0 \to \overline{p}K^+$	(0.022 ± 0.003)	156 ± 24	$\frac{N_{\rm raw}(\Lambda_b^0\to pK^-)}{N_{\rm raw}(B^0\to K^+\pi^-)}$	0.039 ± 0.006
$\Lambda_b^0 \to p\pi^- + \overline{\Lambda}_b^0 \to \overline{p}\pi^+$	(0.015 ± 0.003)	109 ± 23	$\frac{N_{\rm raw}(\Lambda_b^0\to p\pi^-)}{N_{\rm raw}(B^0\to K^+\pi^-)}$	0.027 ± 0.006
			$\frac{N_{\rm raw}(\Lambda_b^0\to p\pi^-)}{N_{\rm raw}(\Lambda_b^0\to pK^-)}$	0.69 ± 0.19

TABLE VI: Raw physics results from the fit. By “raw” we mean that the numbers have not been corrected for the relative efficiency factors yet. Cuts optimized for the measurement of the direct $A_{\mathsf{CP}}(B^0 \to K^+\pi^-)$.

parameter	value
f_{π^+} (combinatorial)	0.545 ± 0.017
f_{e^+} (combinatorial)	0.036 ± 0.005
f_p (combinatorial)	0.080 ± 0.025
f_{K^+} (combinatorial)	0.337 ± 0.031
f_{π^-} (combinatorial)	0.533 ± 0.018
f_{e^-} (combinatorial)	0.030 ± 0.005
$f_{\bar{p}}$ (combinatorial)	0.132 ± 0.027
f_{K^-} (combinatorial)	0.304 ± 0.033
fraction of physics bckg (ARGUS norm.)	0.197 ± 0.016
ARGUS cut-off [GeV/c^2]	5.135 ± 0.001
ARGUS shape	8.467 ± 3.45
f_π (ARGUS)	0.728 ± 0.027
f_K (ARGUS)	0.272 ± 0.027
background fraction	0.481 ± 0.008
c_1 (background shape)	-1.221 ± 0.124
d_1 (Corr. Gaussian 1)	0.993 ± 0.005
μ_1	-0.171 ± 0.020
σ_1	0.087 ± 0.138
μ_2 (Corr. Gaussian 2)	2.481 ± 0.055
σ_2	0.0002 ± 10.

TABLE VII: Complementary results from the fit. Cuts optimized for the measurement of the direct $A_{\mathsf{CP}}(B^0 \to K^+\pi^-)$.

mode	fraction	yield	observable	fit result
$B^0 \to \pi^+\pi^- + \overline{B}^0 \to \pi^+\pi^-$	(0.152 ± 0.008)	875 ± 46	$\frac{N_{\rm raw}(B^0\to\pi^+\pi^-)}{N_{\rm raw}(B^0\to K^+\pi^-)}$	0.269 ± 0.017
$B^0 \to K^+\pi^- + \overline{B}^0 \to K^-\pi^+$	(0.567 ± 0.011)	3256 ± 66	$\frac{N_{\rm raw}(\overline{B}^0\to K^-\pi^+)-N_{\rm raw}(B^0\to K^+\pi^-)}{N_{\rm raw}(\overline{B}^0\to K^-\pi^+)+N_{\rm raw}(B^0\to K^+\pi^-)}$	-0.089 ± 0.025
$B^0 \to K^+\pi^-$	(0.309 ± 0.009)	1773 ± 53		
$\overline{B}^0 \to K^-\pi^+$	(0.258 ± 0.009)	1483 ± 51		
$B^0_s \to K^-\pi^+ + \overline{B}^0_s \to K^+\pi^-$	(0.040 ± 0.006)	230 ± 34	$\frac{N_{\rm raw}(B^0_s\to K^-\pi^+)}{N_{\rm raw}(B^0\to K^+\pi^-)}$	0.070 ± 0.010
$B^0_s \to K^-\pi^+$	(0.012 ± 0.004)	70 ± 22	$\frac{N_{\rm raw}(\overline{B}^0_s\to K^+\pi^-)-N_{\rm raw}(B^0_s\to K^-\pi^+)}{N_{\rm raw}(\overline{B}^0_s\to K^+\pi^-)+N_{\rm raw}(B^0_s\to K^-\pi^+)}$	0.39 ± 0.15
$\overline{B}^0_s \to K^+\pi^-$	(0.028 ± 0.004)	160 ± 26	$\frac{N_{\rm raw}(\overline{B}^0\to K^-\pi^+)-N_{\rm raw}(B^0\to K^+\pi^-)}{N_{\rm raw}(\overline{B}^0_s\to K^+\pi^-)-N_{\rm raw}(B^0_s\to K^-\pi^+)}$	-3.21 ± 1.53
$B^0_s \to K^+K^- + \overline{B}^0_s \to K^+K^-$	(0.179 ± 0.008)	1028 ± 47	$\frac{N_{\rm raw}(B^0_s\to K^+K^-)}{N_{\rm raw}(B^0\to K^+\pi^-)}$	0.316 ± 0.018
$B^0_s \to \pi^+\pi^- + \overline{B}^0_s \to \pi^+\pi^-$	(0.004 ± 0.003)	26 ± 16	$\frac{N_{\rm raw}(B^0_s\to\pi^+\pi^-)}{N_{\rm raw}(B^0\to K^+\pi^-)}$	0.008 ± 0.005
$B^0 \to K^+K^- + \overline{B}^0 \to K^+K^-$	(0.011 ± 0.004)	61 ± 25	$\frac{N_{\rm raw}(B^0\to K^+K^-)}{N_{\rm raw}(B^0\to K^+\pi^-)}$	0.019 ± 0.008
$\Lambda^0_b \to pK^- + \overline{\Lambda}^0_b \to \overline{p}K^+$	(0.027 ± 0.003)	156 ± 20	$\frac{N_{\rm raw}(\Lambda^0_b\to pK^-)}{N_{\rm raw}(B^0\to K^+\pi^-)}$	0.049 ± 0.006
$\Lambda^0_b \to p\pi^- + \overline{\Lambda}^0_b \to \overline{p}\pi^+$	(0.019 ± 0.003)	110 ± 18	$\frac{N_{\rm raw}(\Lambda^0_b\to p\pi^-)}{N_{\rm raw}(B^0\to K^+\pi^-)}$	0.034 ± 0.005
			$\frac{N_{\rm raw}(\Lambda^0_b\to p\pi^-)}{N_{\rm raw}(\Lambda^0_b\to pK^-)}$	0.71 ± 0.15

TABLE VIII: Raw physics results from the fit. By "raw" we mean that the numbers have not been corrected for the relative efficiency factors yet. Cuts optimized for the measurement of the direct $(f_s/f_d)\cdot\mathcal{B}(B^0_s \to K^-\pi^+)/\mathcal{B}(B^0 \to K^+\pi^-)$.

parameter	value
f_{π^+} (combinatorial)	0.506 ± 0.037
f_{e^+} (combinatorial)	0.048 ± 0.012
f_p (combinatorial)	0.095 ± 0.057
f_{K^+} (combinatorial)	0.350 ± 0.072
f_{π^-} (combinatorial)	0.492 ± 0.036
f_{e^-} (combinatorial)	0.034 ± 0.010
$f_{\bar{p}}$ (combinatorial)	0.226 ± 0.064
f_{K^-} (combinatorial)	0.248 ± 0.075
fraction of physics bckg (ARGUS norm.)	0.502 ± 0.033
ARGUS cut-off [GeV/c^2]	5.158 ± 0.001
ARGUS shape	0.429 ± 2.383
f_π (ARGUS)	0.717 ± 0.019
f_K (ARGUS)	0.282 ± 0.020
background fraction	0.307 ± 0.008
c_1 (background shape)	-0.675 ± 0.109
d_1 (Corr. Gaussian 2)	0.993 (fixed)
μ_1	-0.171 (fixed)
σ_1	0.087 (fixed)
μ_2 (Corr. Gaussian 2)	2.481 (fixed)
σ_2	0.0002 (fixed)

TABLE IX: Complementary results from the fit. Cuts optimized for the measurement of the $(f_s/f_d) \cdot \mathcal{B}(B_s^0 \to K^-\pi^+)/\mathcal{B}(B^0 \to K^+\pi^-)$.

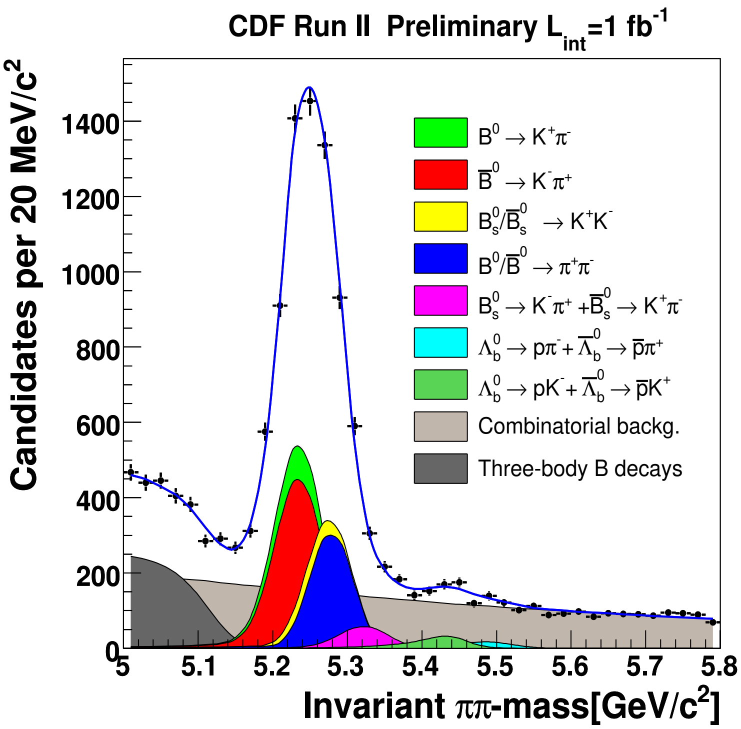

FIG. 37: Fit projection onto the $M_{\pi\pi}$ variable. Cuts optimized for the measurement of $A_{\mathsf{CP}}(B^0 \to K^+\pi^-)$.

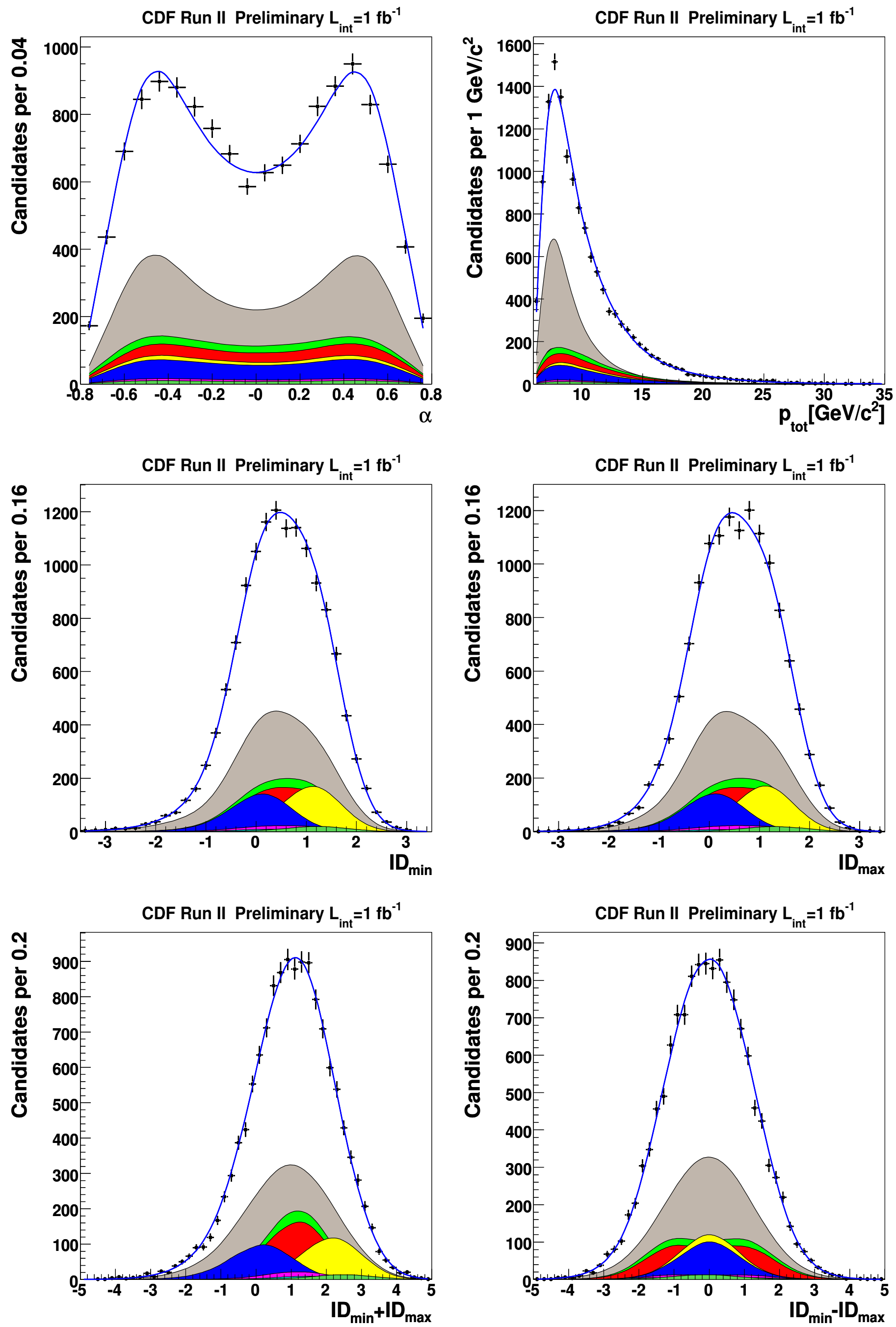

FIG. 38: Fit projections in all mass range onto the α, p_{tot}, ID_{min}, ID_{max}, $ID_{min} + ID_{max}$, $ID_{min} - ID_{max}$ variables. Cuts optimized for the measurement of $A_{\mathsf{CP}}(B^0 \to K^+\pi^-)$.

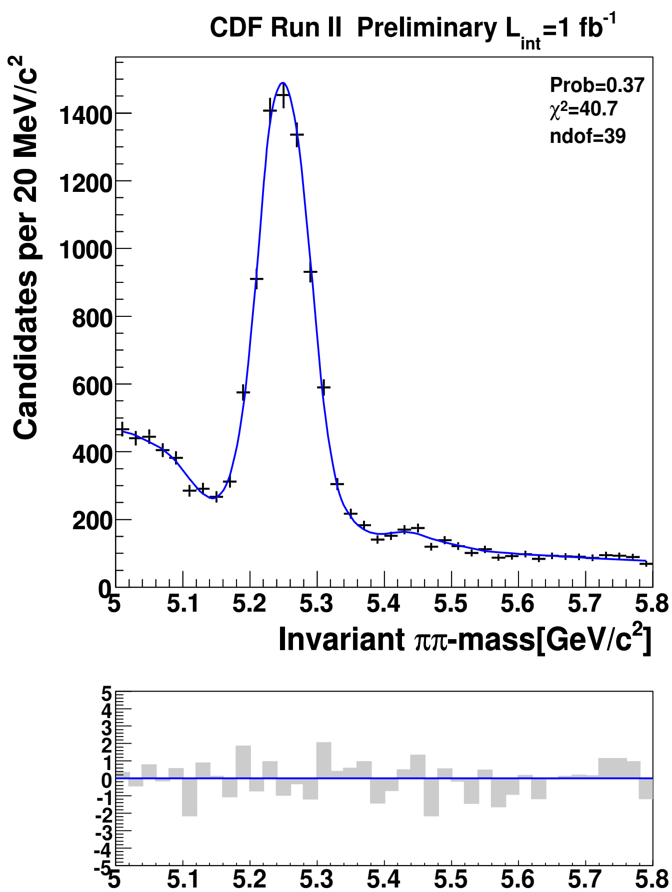

FIG. 39: Fit projection in all mass range onto the $M_{\pi\pi}$ variable. Cuts optimized for the measurement of $A_{\mathsf{CP}}(B^0 \to K^+\pi^-)$.

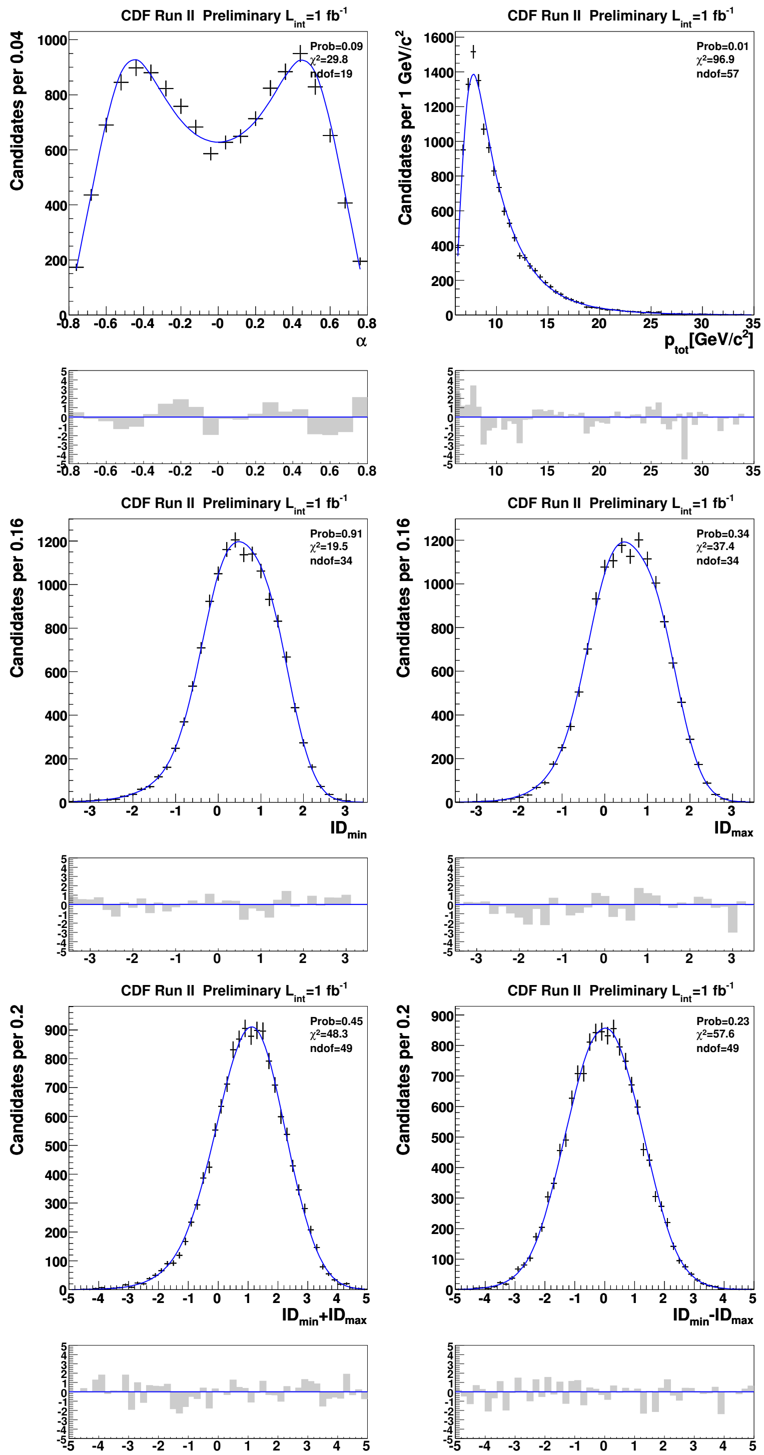

FIG. 40: Fit projections in all mass range onto the α, p_{tot}, ID_{min}, ID_{max}, $ID_{min} + ID_{max}$, $ID_{min} - ID_{max}$ variables. Cuts optimized for the measurement of $A_{\mathsf{CP}}(B^0 \to K^+\pi^-)$.

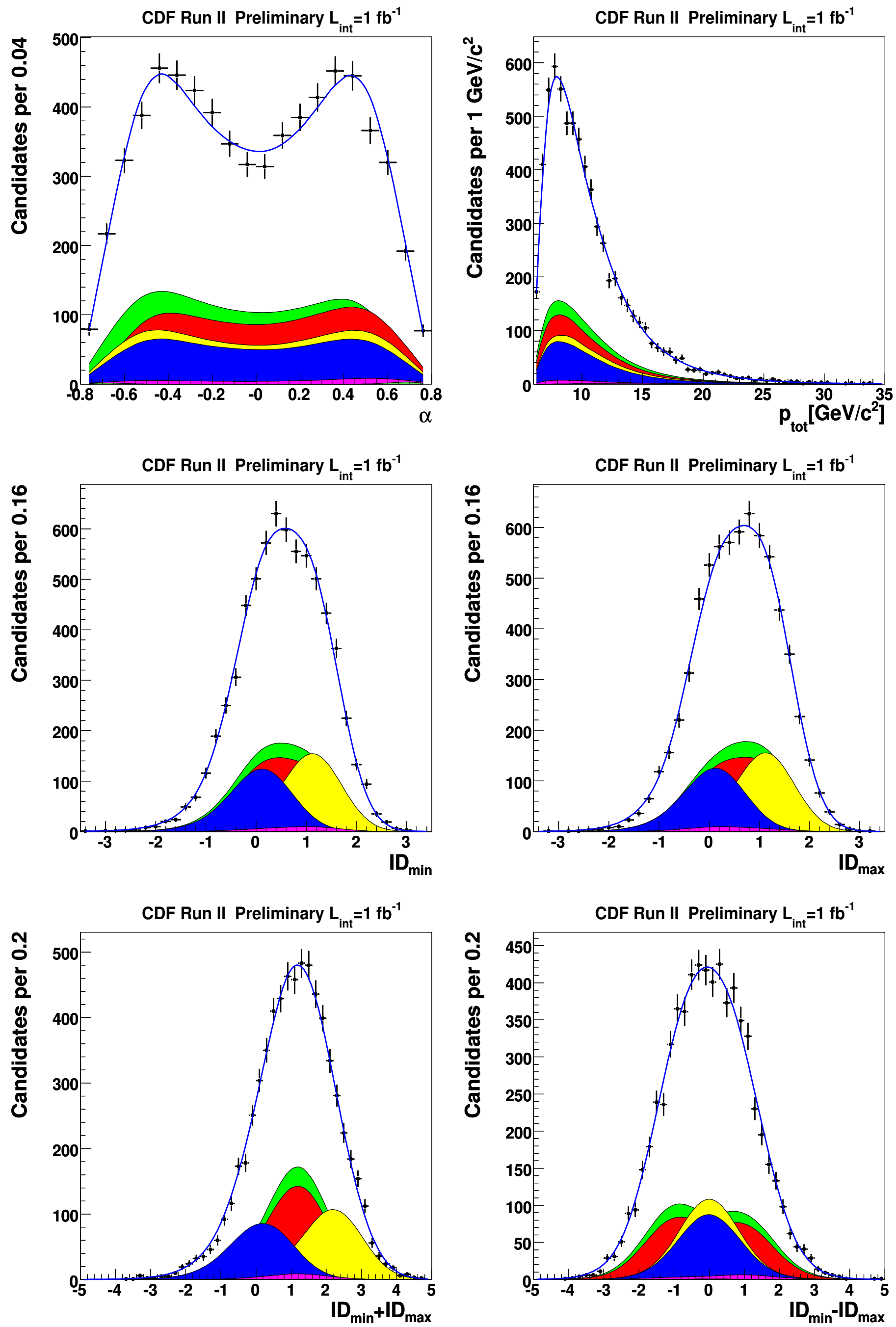

FIG. 41: Fit projections in the signal mass region ($5.19 < M_{\pi\pi} < 5.31$ GeV/c^2) onto the $M_{\pi\pi}$, α, p_{tot}, ID_{min}, ID_{max}, $ID_{min} + ID_{max}$, $ID_{min} - ID_{max}$ variables. Cuts optimized for the measurement of $A_{\mathsf{CP}}(B^0 \to K^+\pi^-)$.

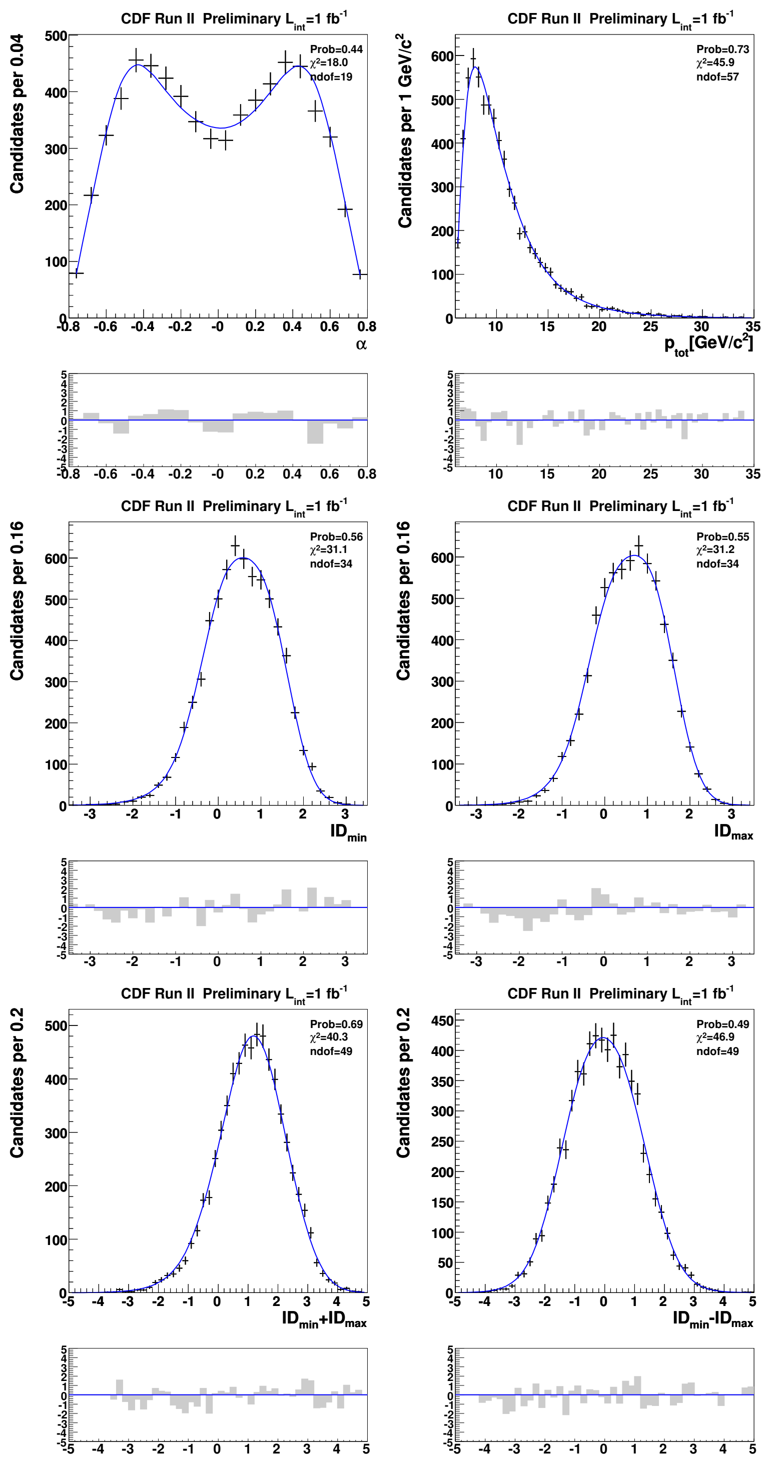

FIG. 42: Fit projections in the signal mass region ($5.19 < M_{\pi\pi} < 5.31$ GeV/c^2) onto the $M_{\pi\pi}$, α, p_{tot}, ID_{min}, ID_{max}, $ID_{min} + ID_{max}$, $ID_{min} - ID_{max}$ variables. Fit with the dE/dx correlation shape free. Cuts optimized for the measurement of $A_{\mathsf{CP}}(B^0 \to K^+\pi^-)$.

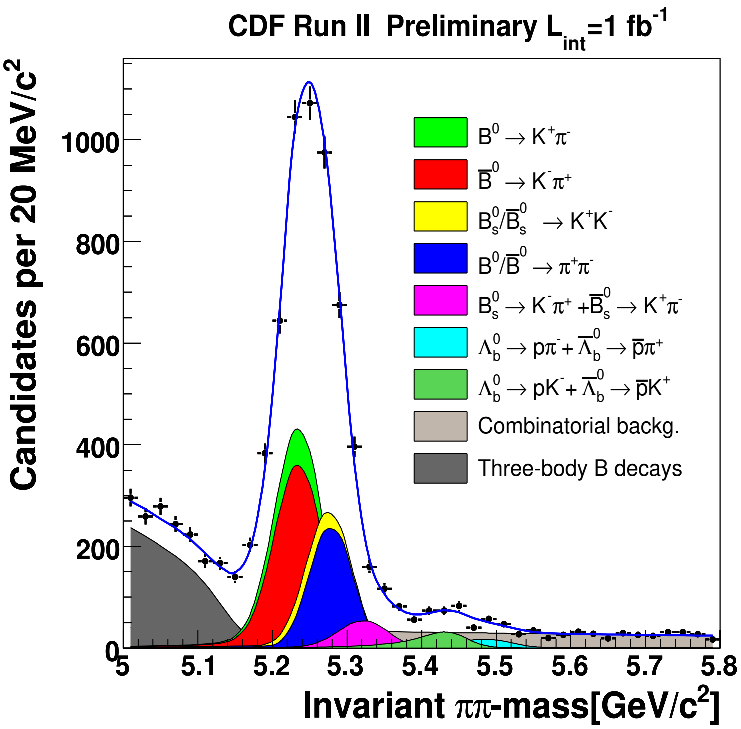

FIG. 43: Fit projection in all mass range onto the $M_{\pi\pi}$ variable. Cuts optimized for the measurement of the $(f_s/f_d) \cdot \mathcal{B}(B_s^0 \to K^-\pi^+)/\mathcal{B}(B^0 \to K^+\pi^-)$.

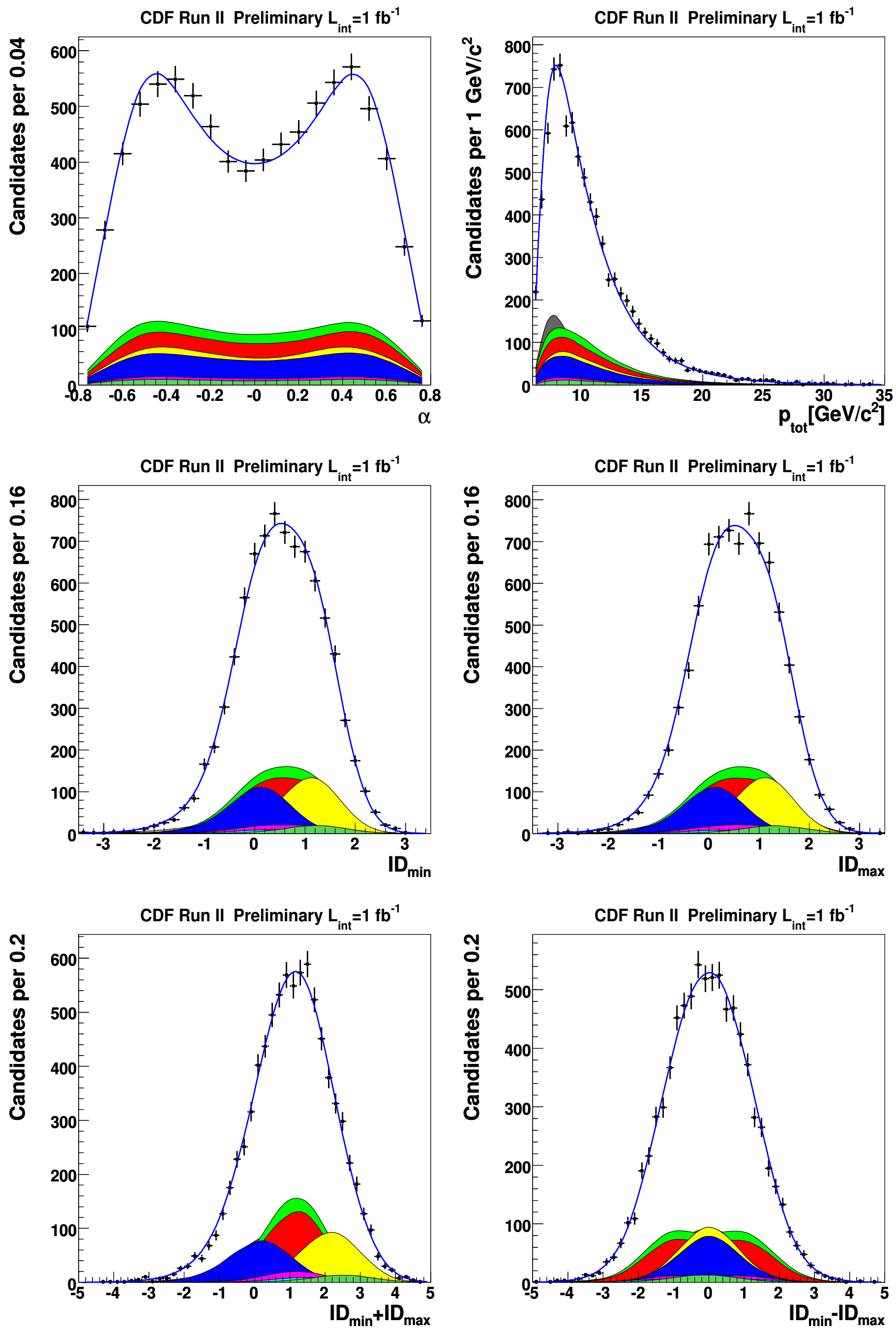

FIG. 44: Fit projections in all mass range onto the α, p_{tot}, ID_{min}, ID_{max}, $ID_{min} + ID_{max}$, $ID_{min} - ID_{max}$ variables. Cuts optimized for the measurement of the $(f_s/f_d) \cdot \mathcal{B}(B_s^0 \to K^-\pi^+)/\mathcal{B}(B^0 \to K^+\pi^-)$.

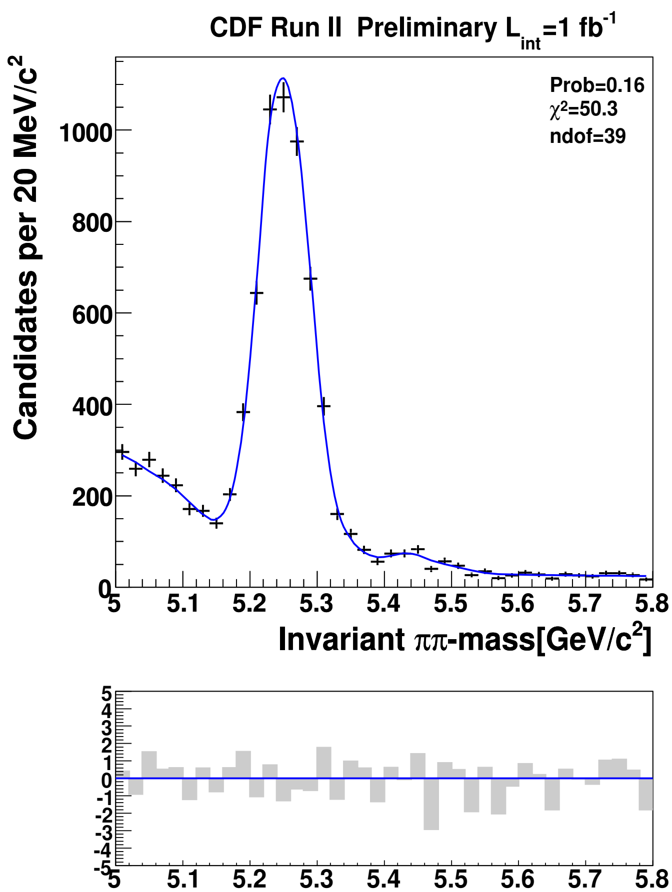

FIG. 45: Fit projection in all mass range onto the $M_{\pi\pi}$ variable. Cuts optimized for the measurement of the $(f_s/f_d) \cdot \mathcal{B}(B_s^0 \to K^-\pi^+)/\mathcal{B}(B^0 \to K^+\pi^-)$.

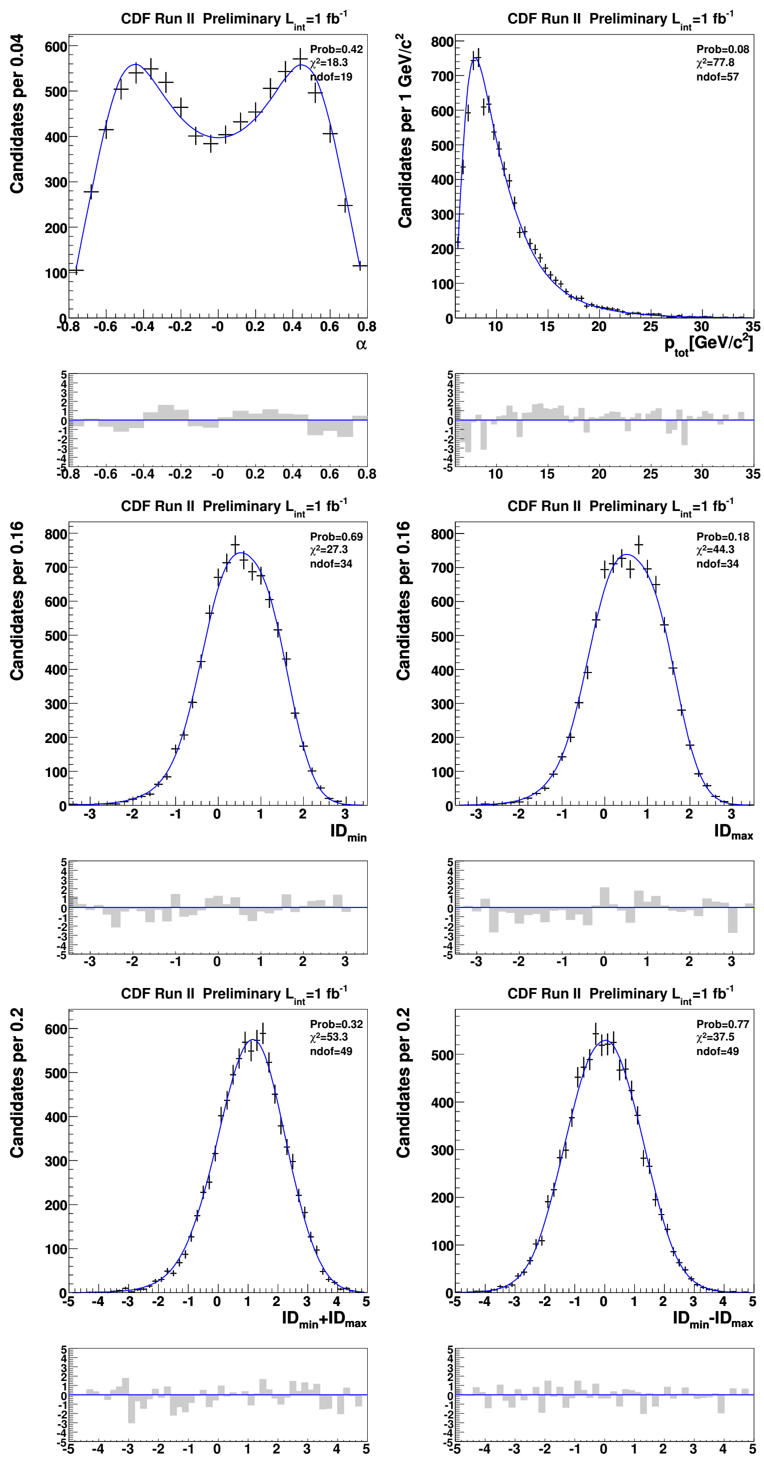

FIG. 46: Fit projections in all mass range onto the α, p_{tot}, ID_{min}, ID_{max}, $ID_{min} + ID_{max}$, $ID_{min} - ID_{max}$ variables. Cuts optimized for the measurement of the $(f_s/f_d) \cdot \mathcal{B}(B^0_s \to K^-\pi^+)/\mathcal{B}(B^0 \to K^+\pi^-)$.

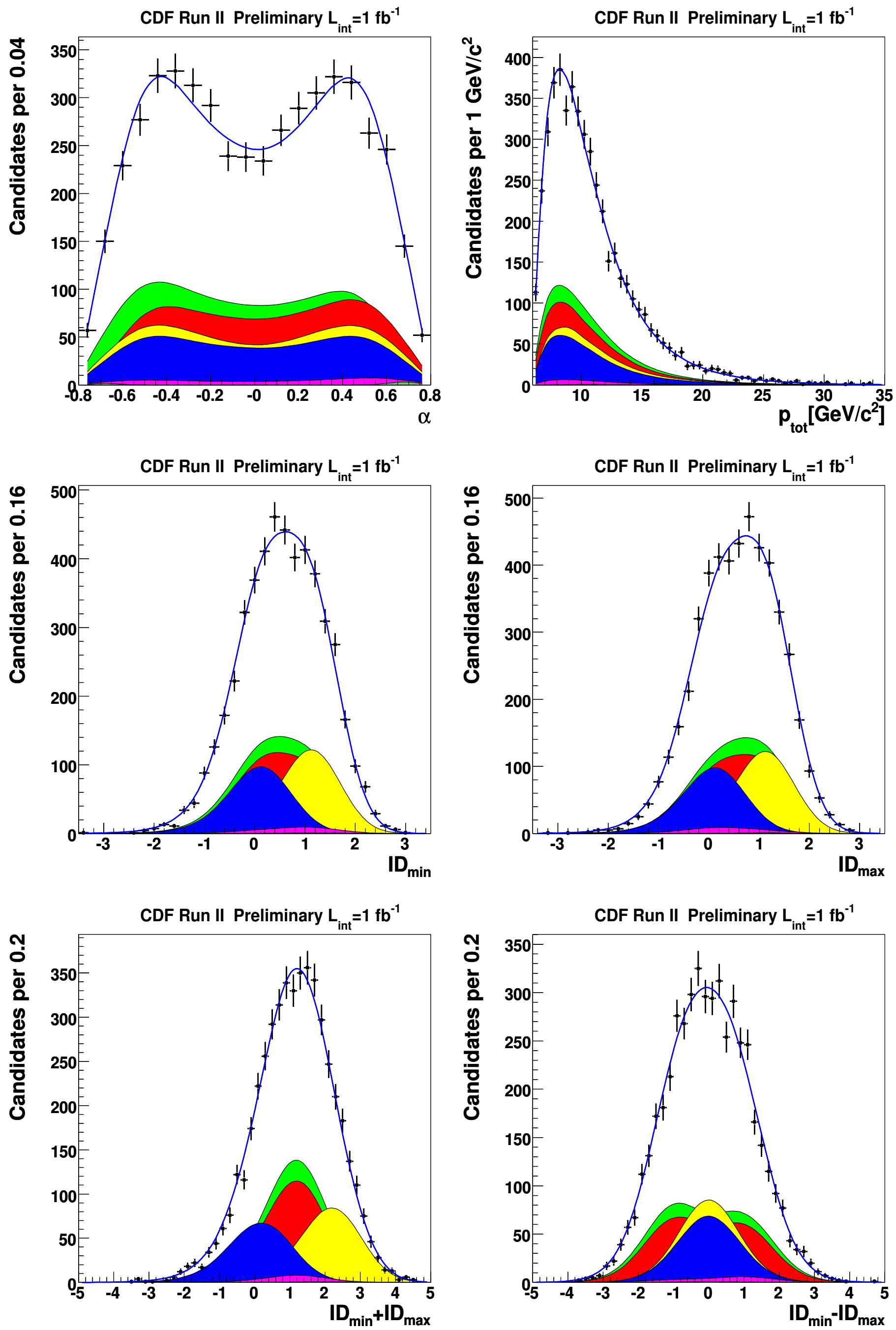

FIG. 47: Fit projections in the signal mass region ($5.19 < M_{\pi\pi} < 5.31$ GeV/c^2) onto the α, p_{tot}, ID_{min}, ID_{max},$ID_{min}+ID_{max}$, $ID_{min}-ID_{max}$ variables. Cuts optimized for the measurement of the $(f_s/f_d)\cdot\mathcal{B}(B_s^0 \to K^-\pi^+)/\mathcal{B}(B^0 \to K^+\pi^-)$.

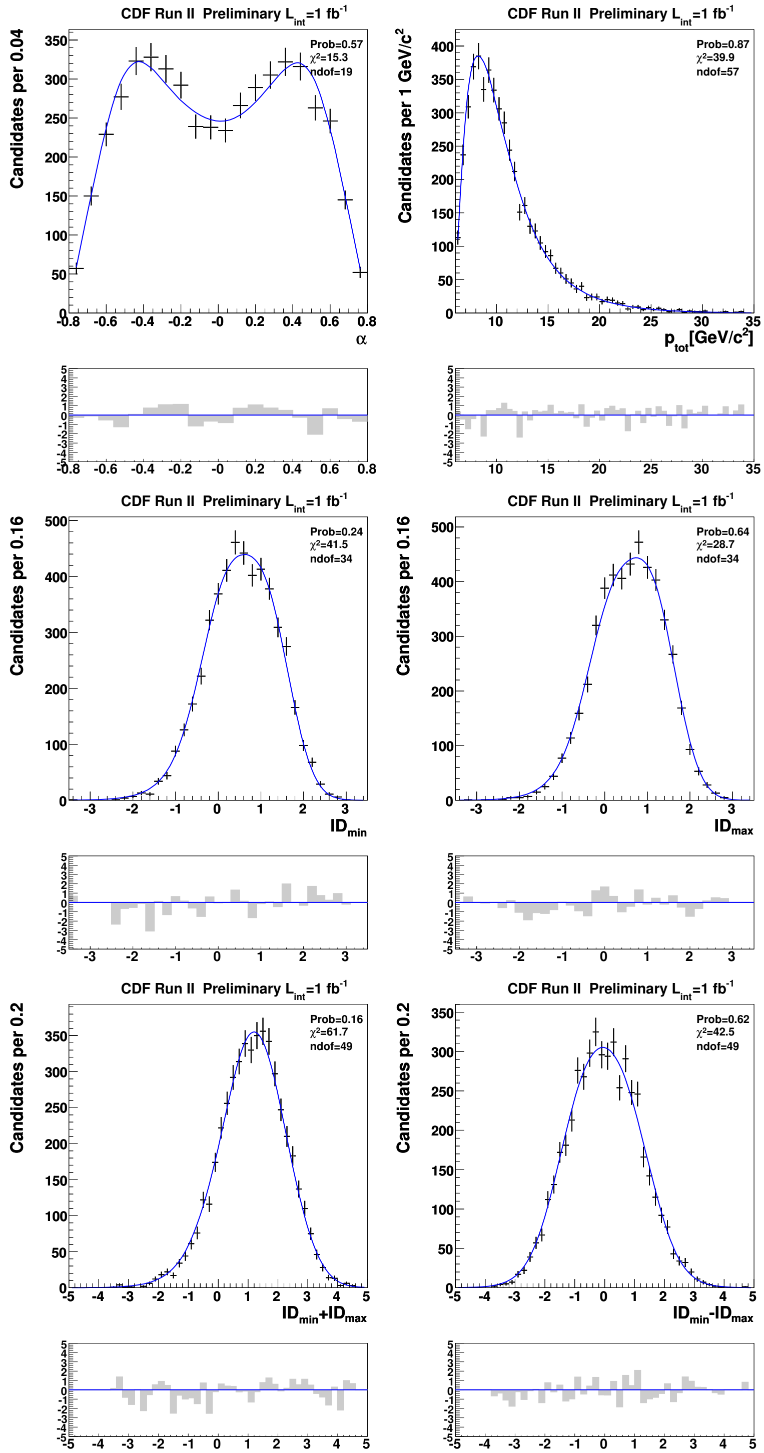

FIG. 48: Fit projections in signal mass region ($5.19 < M_{\pi\pi} < 5.31$ GeV/c^2) onto the α, p_{tot}, ID_{min}, ID_{max}, $ID_{min} + ID_{max}$, $ID_{min} - ID_{max}$ variables. Cuts optimized for the measurement of the $(f_s/f_d) \cdot \mathcal{B}(B_s^0 \to K^-\pi^+)/\mathcal{B}(B^0 \to K^+\pi^-)$.

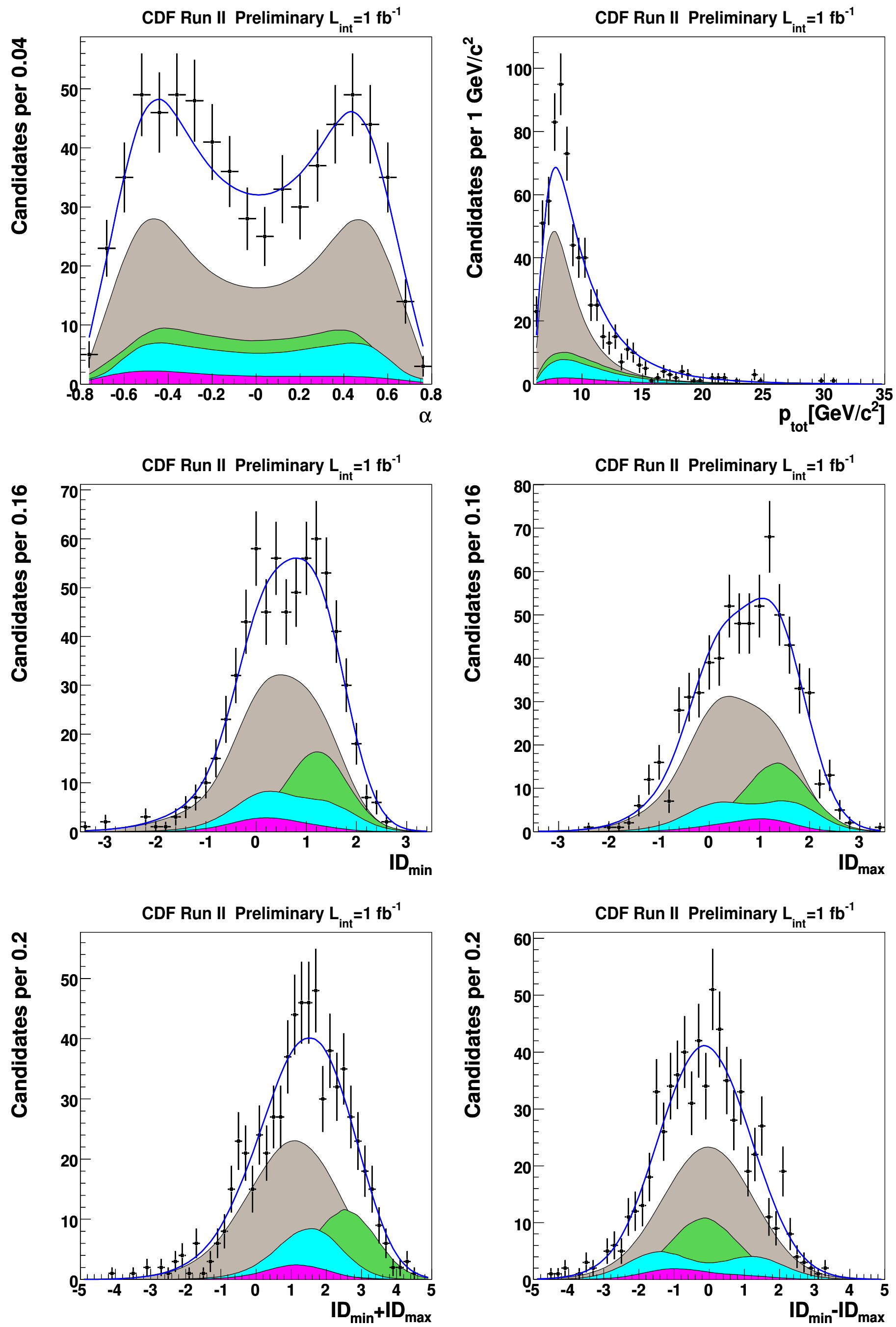

FIG. 49: Fit projections in the Λ_b^0 mass region ($5.35 < M_{\pi\pi} < 5.6$ GeV/c^2) onto the α, p_{tot}, ID_{min}, ID_{max}, $ID_{min} + ID_{max}$, $ID_{min} - ID_{max}$ variables. Cuts optimized for the measurement of the $(f_s/f_d) \cdot \mathcal{B}(B_s^0 \to K^-\pi^+)/\mathcal{B}(B^0 \to K^+\pi^-)$.

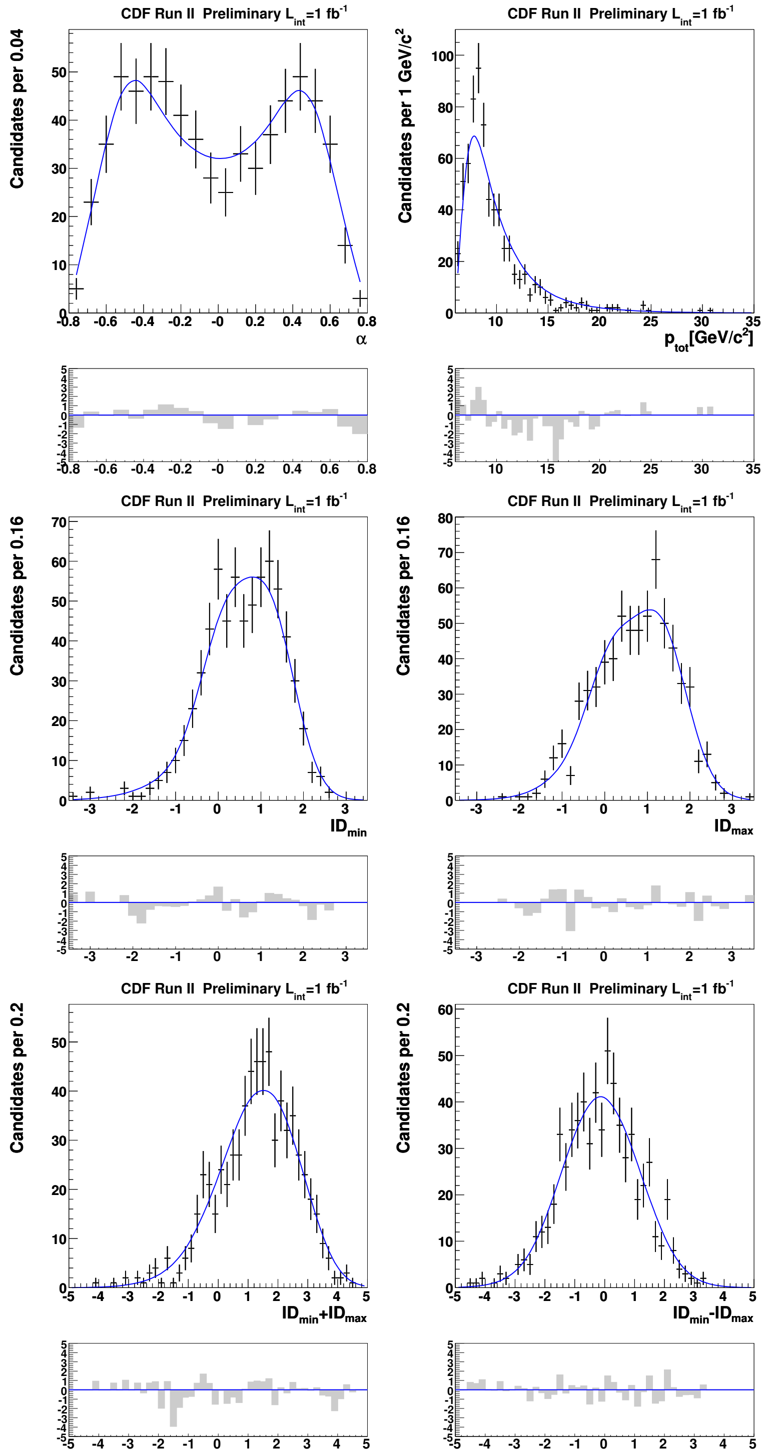

FIG. 50: Fit projections in the Λ_b^0 mass region ($5.35 < M_{\pi\pi} < 5.6$ GeV/c^2) onto the α, p_{tot}, ID_{min}, ID_{max}, $ID_{min} + ID_{max}$, $ID_{min} - ID_{max}$ variables. Cuts optimized for the measurement of the $(f_s/f_d) \cdot \mathcal{B}(B_s^0 \to K^-\pi^+)/\mathcal{B}(B^0 \to K^+\pi^-)$.

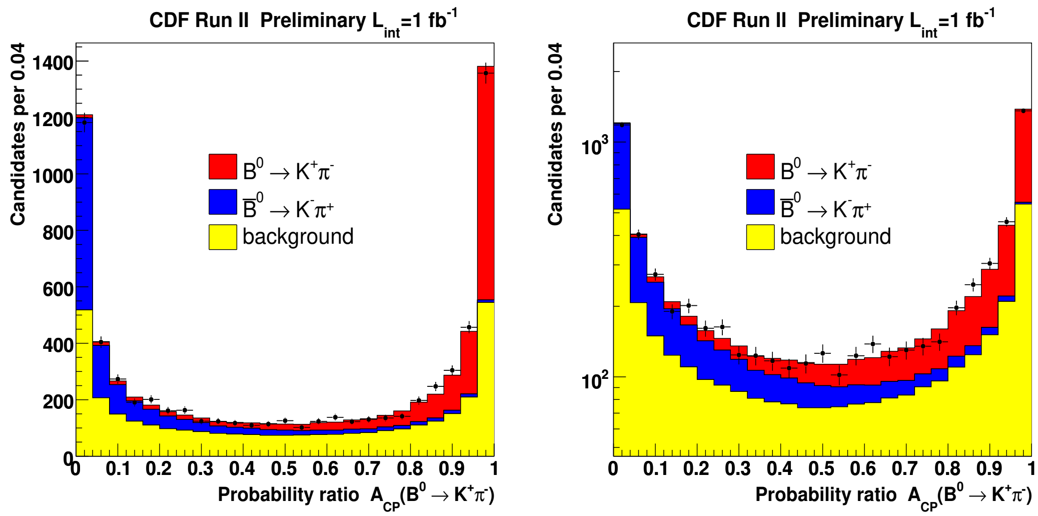

FIG. 51: Probability Ratio for $A_{\mathsf{CP}}(B^0 \to K^+\pi^-)$ in the signal mass region ($5.1 < M_{\pi\pi} < 5.6$ GeV/c^2). Distribution of $pdf_{S_1}/(pdf_{S_1} + pdf_{S_2})$ where $pdf_{S_1(S_2)}$ is the probability for each event to be a signal $S_1(S_2)$. The point with the error bars show the distribution obtained on the fitted data sample while the histogram show the distributions obtained by generating signals and background events directly from the total PDF of the fit of composition.

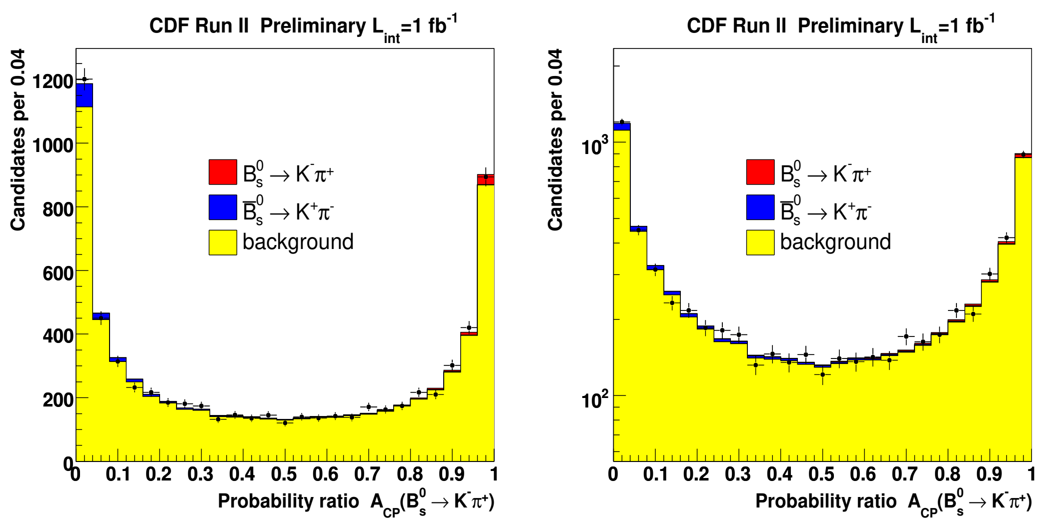

FIG. 52: Probability Ratio for $A_{\mathsf{CP}}(B_s^0 \to K^-\pi^+)$ in the signal mass region ($5.1 < M_{\pi\pi} < 5.6$ GeV/c^2). Distribution of $pdf_{S_1}/(pdf_{S_1} + pdf_{S_2})$ where $pdf_{S_1(S_2)}$ is the probability for each event to be a signal $S_1(S_2)$. The point with the error bars show the distribution obtained on the fitted data sample while the histogram show the distributions obtained by generating signals and background events directly from the total PDF of the fit of composition.

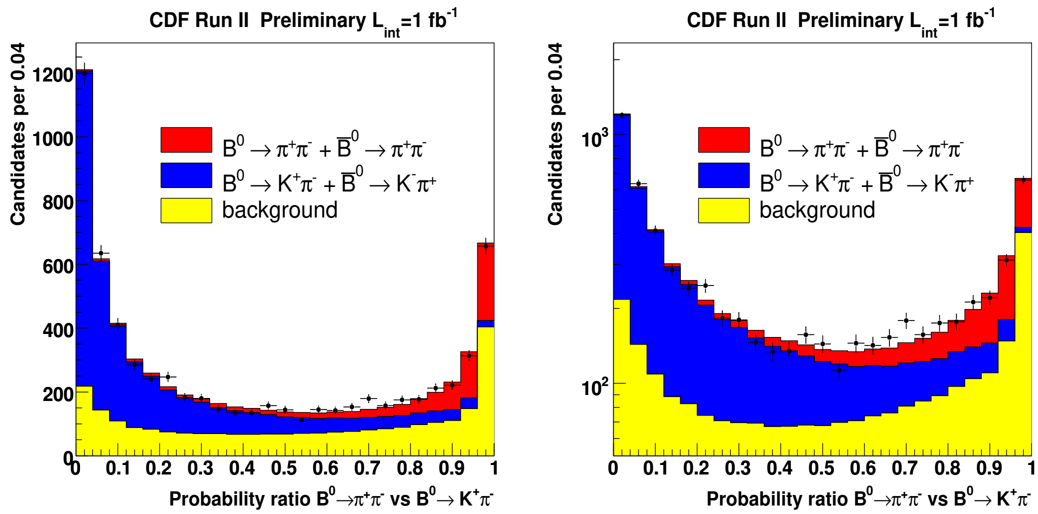

FIG. 53: Probability Ratio $B^0 \to \pi^+\pi^-$ vs $B^0 \to K^+\pi^-$ in the signal mass region ($5.1 < M_{\pi\pi} < 5.6$ GeV/c^2). Distribution of $pdf_{S_1}/(pdf_{S_1} + pdf_{S_2})$ where $pdf_{S_1(S_2)}$ is the probability for each event to be a signal $S_1(S_2)$. The point with the error bars show the distribution obtained on the fitted data sample while the histogram show the distributions obtained by generating signals and background events directly from the total PDF of the fit of composition.

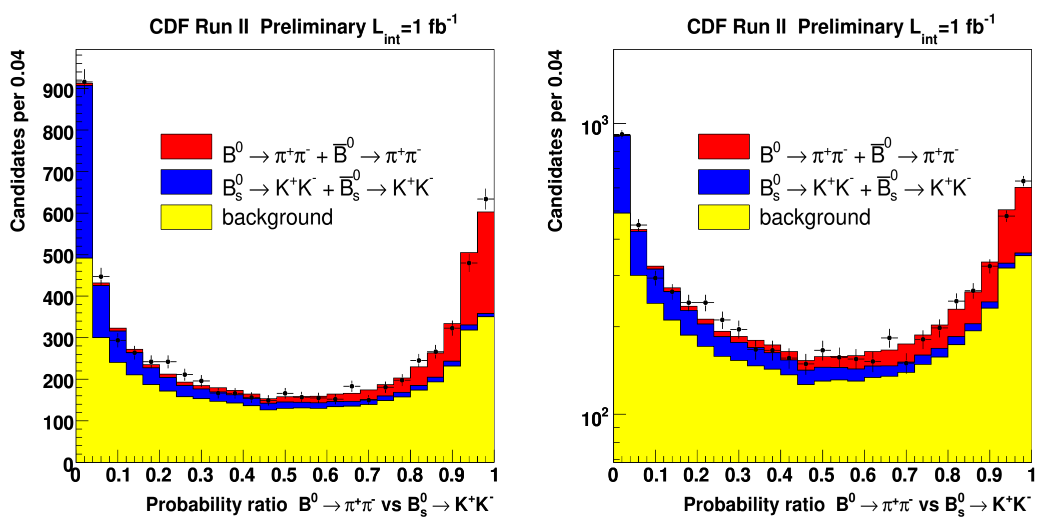

FIG. 54: Probability Ratio for $B^0 \to \pi^+\pi^-$ vs $B^0_s \to K^+K^-$ in the signal mass region ($5.1 < M_{\pi\pi} < 5.6$ GeV/c^2). Distribution of $pdf_{S_1}/(pdf_{S_1} + pdf_{S_2})$ where $pdf_{S_1(S_2)}$ is the probability for each event to be a signal $S_1(S_2)$. The point with the error bars show the distribution obtained on the fitted data sample while the histogram show the distributions obtained by generating signals and background events directly from the total PDF of the fit of composition.

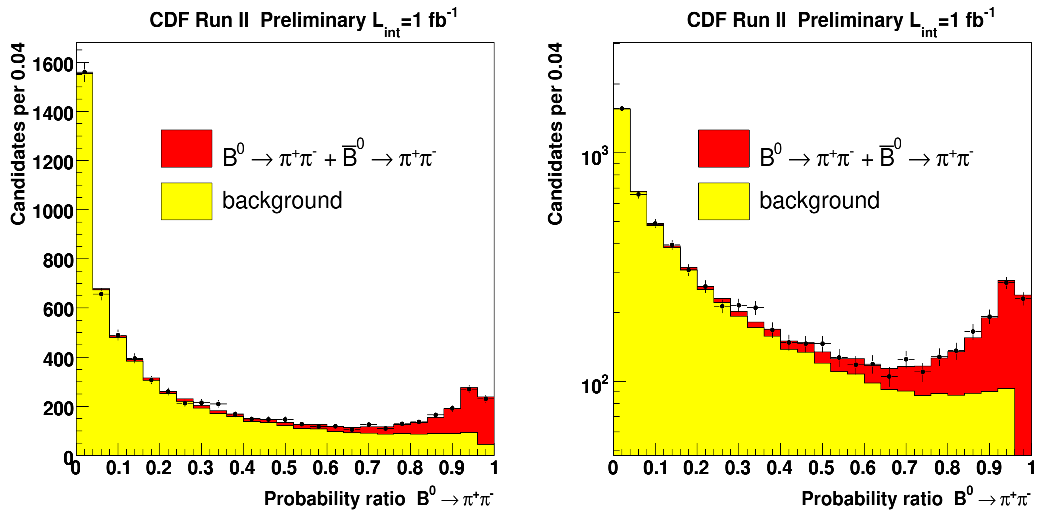

FIG. 55: Probability Ratio for $B^0 \to \pi^+\pi^-$ vs background in the signal mass region ($5.1 < M_{\pi\pi} < 5.6$ GeV/c^2). Distribution of $pdf_S/(pdf_S + pdf_{Rest})$ where pdf_S is the probability for each event to be a signal S and pdf_{Rest} is the probability for each event to be all except the signal S (other signals and backgrounds with the measured relative fractions). The point with the error bars show the distribution obtained on the fitted data sample while the histogram show the distributions obtained by generating signals and background events directly from the total PDF of the fit of composition.

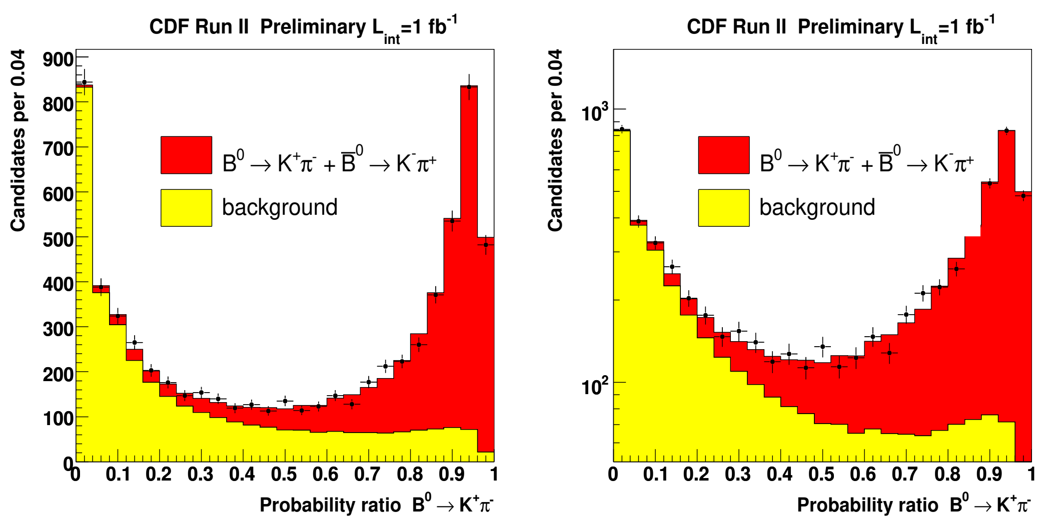

FIG. 56: Probability Ratio for $B^0 \to K^+\pi^-$ vs background in the signal mass region ($5.1 < M_{\pi\pi} < 5.6$ GeV/c^2). Distribution of $pdf_S/(pdf_S + pdf_{Rest})$ where pdf_S is the probability for each event to be a signal S and pdf_{Rest} is the probability for each event to be all except the signal S (other signals and backgrounds with the measured relative fractions). The point with the error bars show the distribution obtained on the fitted data sample while the histogram show the distributions obtained by generating signals and background events directly from the total PDF of the fit of composition.

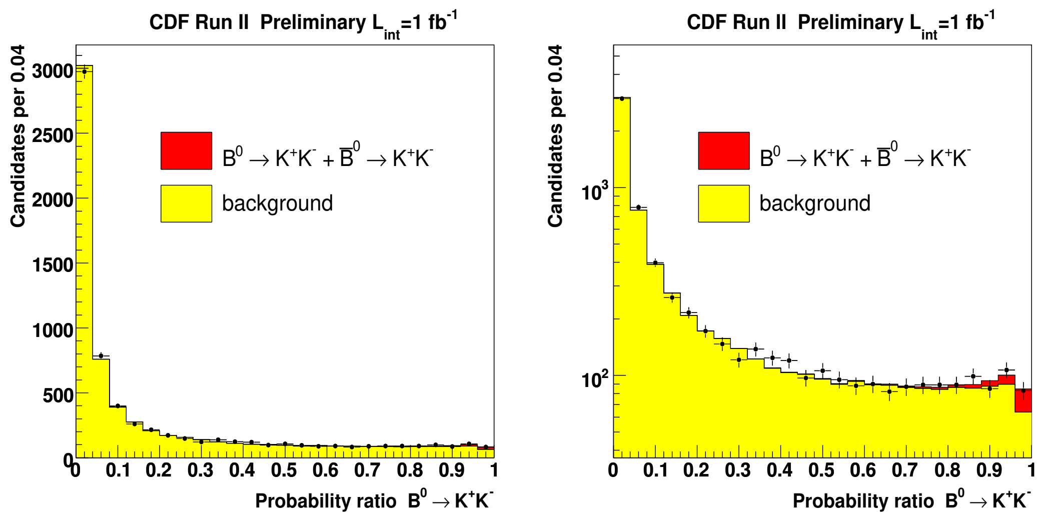

FIG. 57: Probability Ratio for $B^0 \rightarrow K^+K^-$ vs background in the signal mass region ($5.1 < M_{\pi\pi} < 5.6$ GeV/c^2) Distribution of $pdf_S/(pdf_S + pdf_{Rest})$ where pdf_S is the probability for each event to be a signal S and pdf_{Rest} is the probability for each event to be all except the signal S (other signals and backgrounds with the measured relative fractions). The point with the error bars show the distribution obtained on the fitted data sample while the histogram show the distributions obtained by generating signals and background events directly from the total PDF of the fit of composition.

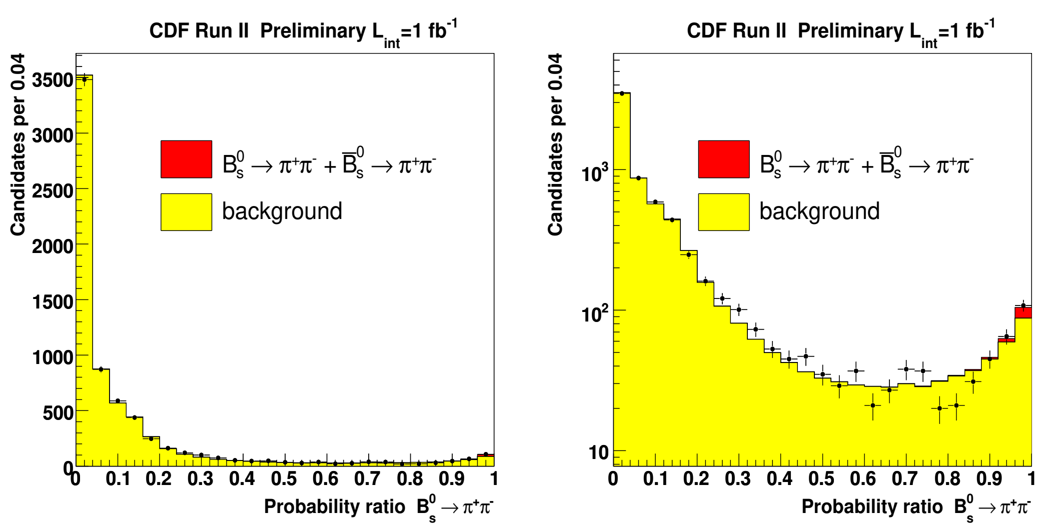

FIG. 58: Probability Ratio for $B^0_s \rightarrow \pi^+\pi^-$ vs background in the signal mass region ($5.1 < M_{\pi\pi} < 5.6$ GeV/c^2) Distribution of $pdf_S/(pdf_S + pdf_{Rest})$ where pdf_S is the probability for each event to be a signal S and pdf_{Rest} is the probability for each event to be all except the signal S (other signals and backgrounds with the measured relative fractions). The point with the error bars show the distribution obtained on the fitted data sample while the histogram show the distributions obtained by generating signals and background events directly from the total PDF of the fit of composition.

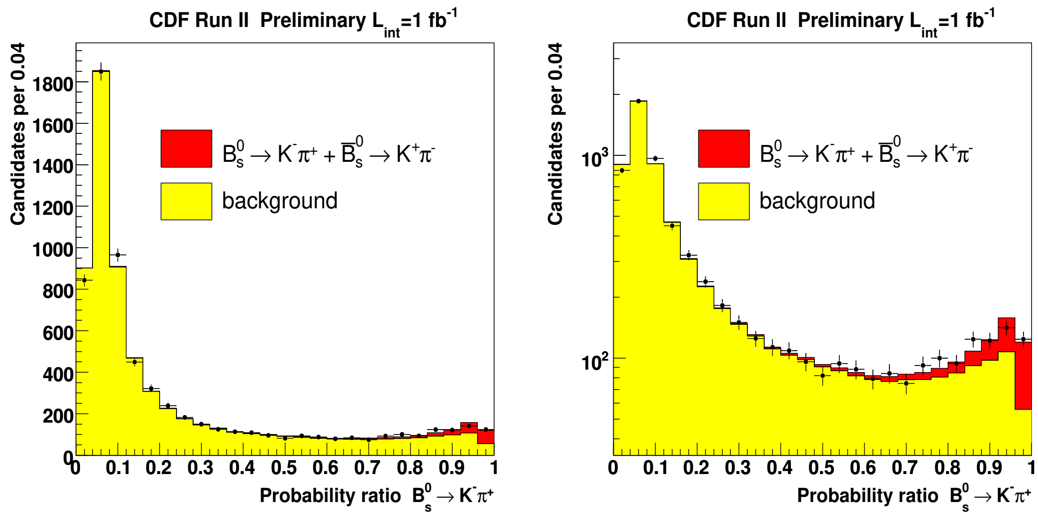

FIG. 59: Probability Ratio for $B_s^0 \to K^- \pi^+$ vs background in the signal mass region ($5.1 < M_{\pi\pi} < 5.6$ GeV/c^2) Distribution of $pdf_S/(pdf_S + pdf_{Rest})$ where pdf_S is the probability for each event to be a signal S and pdf_{Rest} is the probability for each event to be all except the signal S (other signals and backgrounds with the measured relative fractions). The point with the error bars show the distribution obtained on the fitted data sample while the histogram show the distributions obtained by generating signals and background events directly from the total PDF of the fit of composition.

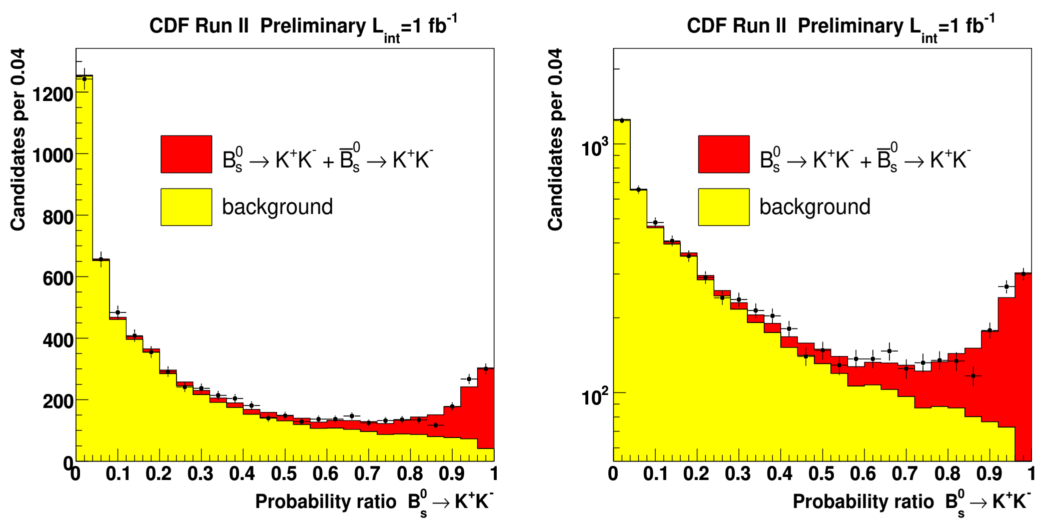

FIG. 60: Probability Ratio for $B_s^0 \to K^+ K^-$ vs background in the signal mass region ($5.1 < M_{\pi\pi} < 5.6$ GeV/c^2) Distribution of $pdf_S/(pdf_S + pdf_{Rest})$ where pdf_S is the probability for each event to be a signal S and pdf_{Rest} is the probability for each event to be all except the signal S (other signals and backgrounds with the measured relative fractions). The point with the error bars show the distribution obtained on the fitted data sample while the histogram show the distributions obtained by generating signals and background events directly from the total PDF of the fit of composition.

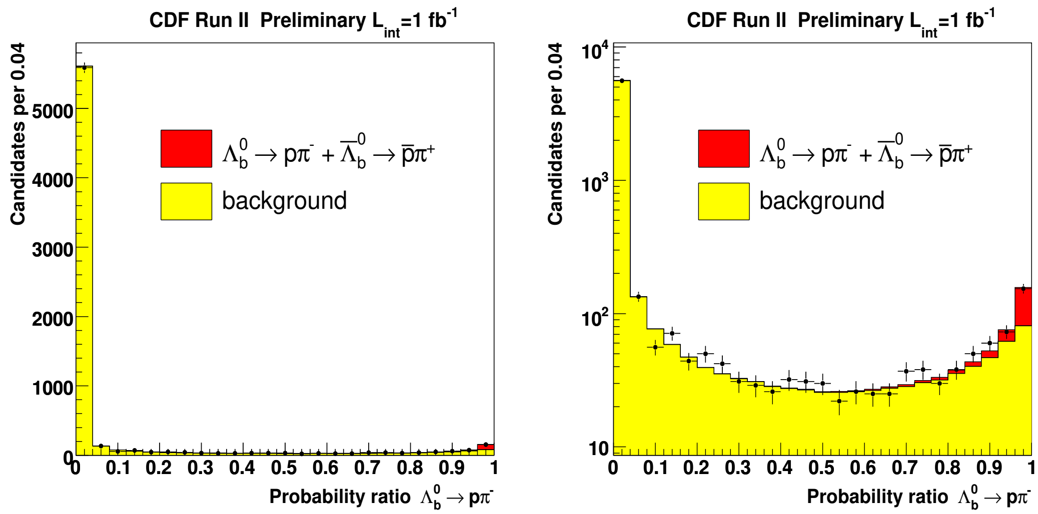

FIG. 61: Probability Ratio for $\Lambda_b^0 \to p\pi^-$ vs background in the signal mass region ($5.1 < M_{\pi\pi} < 5.6$ GeV/c^2) Distribution of $pdf_S/(pdf_S + pdf_{Rest})$ where pdf_S is the probability for each event to be a signal S and pdf_{Rest} is the probability for each event to be all except the signal S (other signals and backgrounds with the measured relative fractions). The point with the error bars show the distribution obtained on the fitted data sample while the histogram show the distributions obtained by generating signals and background events directly from the total PDF of the fit of composition.

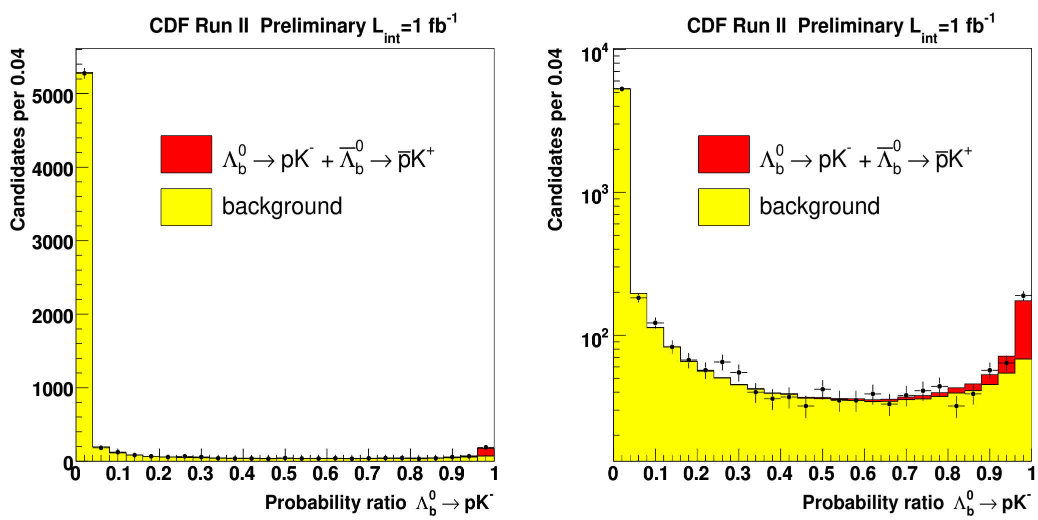

FIG. 62: Probability Ratio for $\Lambda_b^0 \to pK^-$ vs background in the signal mass region ($5.1 < M_{\pi\pi} < 5.6$ GeV/c^2) Distribution of $pdf_S/(pdf_S + pdf_{Rest})$ where pdf_S is the probability for each event to be a signal S and pdf_{Rest} is the probability for each event to be all except the signal S (other signals and backgrounds with the measured relative fractions). The point with the error bars show the distribution obtained on the fitted data sample while the histogram show the distributions obtained by generating signals and background events directly from the total PDF of the fit of composition.

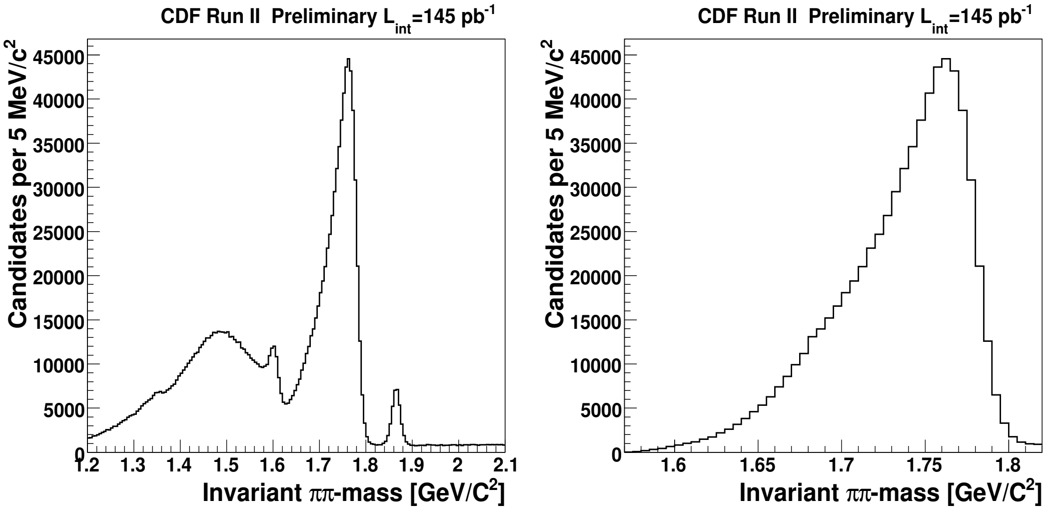

FIG. 63: Invariant $\pi\pi$-mass ($M_{\pi\pi}$) distribution. Left plot: $D^0 \rightarrow K^+K^-$, $D^0 \rightarrow K^-\pi^+$, $D^0 \rightarrow \pi^+\pi^-$decays (prompt) after applying the selection used to reconstruct the $B^0_{(s)} \rightarrow h^+h^{'-}$data sample reported in table IV. Right plot: $D^0 \rightarrow K^-\pi^+$decays (prompt) after applying the selection used to reconstruct the $B^0_{(s)} \rightarrow h^+h^{'-}$data sample reported in table IV plus the cuts: $m_{KK} \geq 1.93 GeV/c^2$ and $M_{\pi\pi} \leq 1.82 GeV/c^2$.

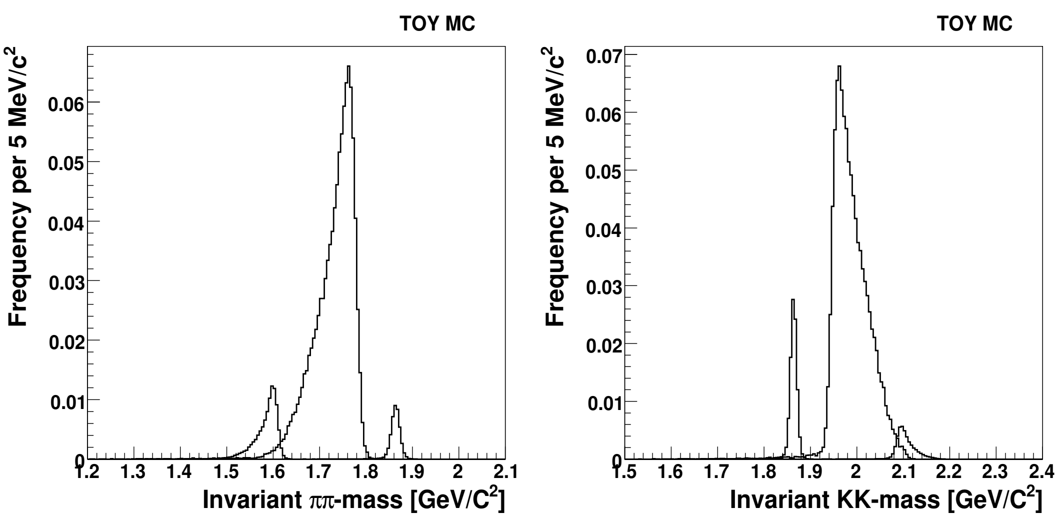

FIG. 64: Left plot: invariant $\pi\pi$-mass ($M_{\pi\pi}$) Monte Carlo distribution of $D^0 \rightarrow K^+K^-$, $D^0 \rightarrow K^-\pi^+$, $D^0 \rightarrow \pi^+\pi^-$decays (prompt). Right plot: invariant KK-mass (m_{KK}) Monte Carlo distribution of $D^0 \rightarrow K^+K^-$, $D^0 \rightarrow K^-\pi^+$, $D^0 \rightarrow \pi^+\pi^-$decays (prompt).

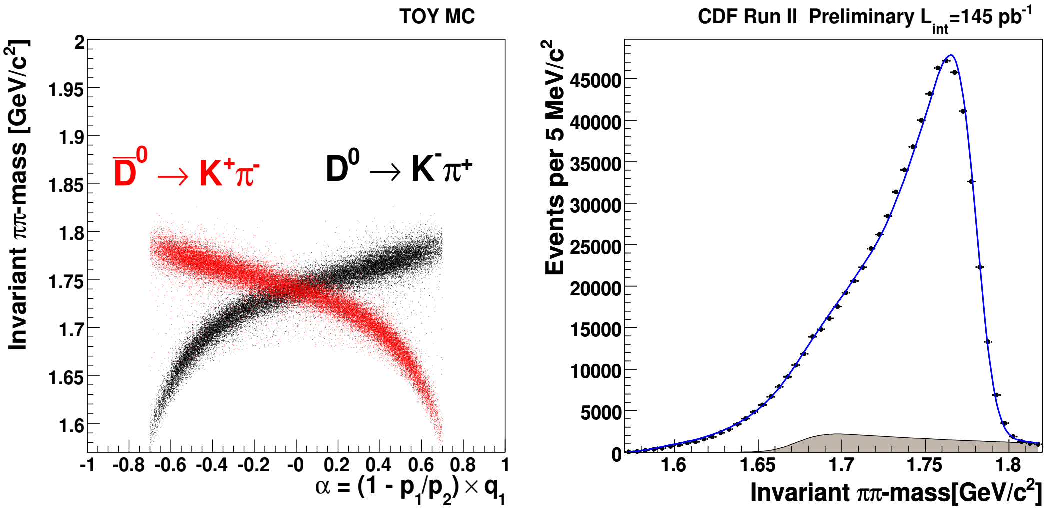

FIG. 65: Left plot (Monte Carlo): distribution of invariant $\pi\pi$-mass ($M_{\pi\pi}$) as a function of momentum imbalance $\alpha = (1 - p_1/p_2) \times q_1$ (red $\overline{D}^0 \rightarrow K^+\pi^-$, black $D^0 \rightarrow K^-\pi^+$). Right plot (DATA): fit projection onto the $M_{\pi\pi}$ variable.

source	shift wrt central fit
mass scale	0.0004
asymmetric momentum-p.d.f	0.0001
dE/dx	0.0064
input masses	0.0054
combinatorial background model	0.0027
momentum background model	0.0007
MC statistics	–
charge asymmetry	0.0014
$\boldsymbol{\Delta\Gamma_s/\Gamma_s}$ **Standard Model**	–
lifetime	–
isolation efficiency	–
XFT-bias correction	–
TOTAL (sum in quadrature)	**0.009**

TABLE X: Summary of systematic uncertainties for the $A_{\mathsf{CP}}(B^0 \to K^+\pi^-)$ measurement.

source	shift wrt central fit
mass scale	0.009
asymmetric momentum-p.d.f	0.020
dE/dx	0.053
input masses	0.020
combinatorial background model	0.034
momentum background model	0.040
MC statistics	–
charge asymmetry	0.001
$\boldsymbol{\Delta\Gamma_s/\Gamma_s}$ **Standard Model**	–
lifetime	–
isolation efficiency	–
XFT-bias correction	–
TOTAL (sum in quadrature)	**0.080**

TABLE XI: Summary of systematic uncertainties for the $A_{\mathsf{CP}}(B_s^0 \to K^-\pi^+)$ measurement.

source	shift wrt central fit
mass scale	0.0017
asymmetric momentum-p.d.f	0.0020
dE/dx	0.0036
input masses	0.0029
combinatorial background model	0.0040
momentum background model	0.0024
MC statistics	0.0003
charge asymmetry	–
$\boldsymbol{\Delta\Gamma_s/\Gamma_s}$ **Standard Model**	–
lifetime	0.0001
isolation efficiency	0.0020
XFT-bias correction	0.0011
TOTAL (sum in quadrature)	**0.0074**

TABLE XII: Summary of systematic uncertainties for the $(f_s/f_d) \cdot \mathcal{B}(B_s^0 \to K^-\pi^+)/\mathcal{B}(B^0 \to K^+\pi^-)$ measurement.

source	shift wrt central fit
mass scale	0.009
asymmetric momentum-p.d.f	0.045
dE/dx	0.115
input masses	0.060
combinatorial background model	0.040
momentum background model	0.116
MC statistics	0.012
charge asymmetry	0.042
$\boldsymbol{\Delta\Gamma_s/\Gamma_s}$ **Standard Model**	–
lifetime	0.065
isolation efficiency	0.084
XFT-bias correction	0.054
TOTAL (sum in quadrature)	**0.224**

TABLE XIII: Summary of systematic uncertainties for the $(f_d/f_s) \cdot (\mathcal{B}(\overline{B}^0 \to K^-\pi^+) - \mathcal{B}(B^0 \to K^+\pi^-))/(\mathcal{B}(\overline{B}_s^0 \to K^+\pi^-) - \mathcal{B}(B_s^0 \to K^-\pi^+))$ measurement.

source	shift wrt central fit
mass scale	0.0034
asymmetric momentum-p.d.f	0.0030
dE/dx	0.0107
input masses	0.0050
combinatorial background model	0.0020
momentum background model	0.0060
MC statistics	0.0012
charge asymmetry	–
$\boldsymbol{\Delta\Gamma_s/\Gamma_s}$ **Standard Model**	0.0060
lifetime	0.0060
isolation efficiency	0.0097
XFT-bias correction	0.0080
TOTAL (sum in quadrature)	**0.0208**

TABLE XIV: Summary of systematic uncertainties for the $(f_s/f_d) \cdot \mathcal{B}(B_s^0 \to K^+K^-)/\mathcal{B}(B^0 \to K^+\pi^-)$ measurement.

source	shift wrt central fit
mass scale	0.0036
asymmetric momentum-p.d.f	0.0006
dE/dx	0.0129
input masses	0.0050
combinatorial background model	0.0020
momentum background model	0.0010
MC statistics	0.0011
charge asymmetry	–
$\boldsymbol{\Delta\Gamma_s/\Gamma_s}$ **Standard Model**	–
lifetime	–
isolation efficiency	–
XFT-bias correction	0.0050
TOTAL (sum in quadrature)	**0.0165**

TABLE XV: Summary of systematic uncertainties for the $\mathcal{B}(B^0 \to \pi^+\pi^-)/\mathcal{B}(B^0 \to K^+\pi^-)$ measurement.

source	shift wrt central fit
mass scale	0.0009
asymmetric momentum-p.d.f	0.0010
dE/dx	0.0033
input masses	0.0016
combinatorial background model	0.0030
momentum background model	0.0040
MC statistics	0.
charge asymmetry	–
$\boldsymbol{\Delta\Gamma_s/\Gamma_s}$ **Standard Model**	–
lifetime	–
isolation efficiency	–
XFT-bias correction	0.0001
TOTAL (sum in quadrature)	**0.0063**

TABLE XVI: Summary of systematic uncertainties for the $\mathcal{B}(B^0 \to K^+K^-)/\mathcal{B}(B^0 \to K^+\pi^-)$ measurement.

source	shift wrt central fit
mass scale	0.0002
asymmetric momentum-p.d.f	0.0022
dE/dx	0.0007
input masses	0.0003
combinatorial background model	0.0015
momentum background model	0.0043
MC statistics	0.
charge asymmetry	–
$\boldsymbol{\Delta\Gamma_s/\Gamma_s}$ **Standard Model**	0.
lifetime	0.0001
isolation efficiency	0.0002
XFT-bias correction	0.0001
TOTAL (sum in quadrature)	**0.0052**

TABLE XVII: Summary of systematic uncertainties for the $(f_s/f_d) \cdot \mathcal{B}(B^0_s \to \pi^+\pi^-)/\mathcal{B}(B^0 \to K^+\pi^-)$ measurement.

source	shift wrt central fit
mass scale	0.0040
asymmetric momentum-p.d.f	0.0320
dE/dx	0.0502
input masses	0.0180
combinatorial background model	0.0468
momentum background model	0.0060
MC statistics	0.0028
charge asymmetry	–
$\boldsymbol{\Delta\Gamma_s/\Gamma_s}$ **Standard Model**	–
lifetime	–
isolation efficiency	–
XFT-bias correction	0.0120
TOTAL (sum in quadrature)	**0.0790**

TABLE XVIII: Summary of systematic uncertainties for the $\mathcal{B}(\Lambda_b^0 \to p\pi^-)/\mathcal{B}(\Lambda_b^0 \to pK^-)$ measurement.

source	shift wrt central fit
mass scale	4
asymmetric momentum-p.d.f	4
dE/dx	13
input masses	6
combinatorial background model	27
momentum background model	17
TOTAL (sum in quadrature)	**35**

TABLE XIX: Summary of systematic uncertainties for the $N(B^0 \to K^+K^-)$ measurement.

source	shift wrt central fit
mass scale	1
asymmetric momentum-p.d.f	6
dE/dx	7
input masses	3
combinatorial background model	12
momentum background model	4
TOTAL (sum in quadrature)	**16**

TABLE XX: Summary of systematic uncertainties for the $N(B_s^0 \to K^-\pi^+)$ measurement.

source	shift wrt central fit
mass scale	1
asymmetric momentum-p.d.f	9
dE/dx	2
input masses	3
combinatorial background model	8
momentum background model	7
TOTAL (sum in quadrature)	**14**

TABLE XXI: Summary of systematic uncertainties for the $N(B_s^0 \to \pi^+\pi^-)$ measurement.

source	shift wrt central fit
mass scale	1
asymmetric momentum-p.d.f	1
dE/dx	7
input masses	2
combinatorial background model	6
momentum background model	6
TOTAL (sum in quadrature)	**11**

TABLE XXII: Summary of systematic uncertainties for the $N(\Lambda_b^0 \to pK^-)$ measurement.

source	shift wrt central fit
mass scale	1
asymmetric momentum-p.d.f	6
dE/dx	7
input masses	3
combinatorial background model	12
momentum background model	4
TOTAL (sum in quadrature)	**16**

TABLE XXIII: Summary of systematic uncertainties for the $N(\Lambda_b^0 \to p\pi^-)$ measurement.

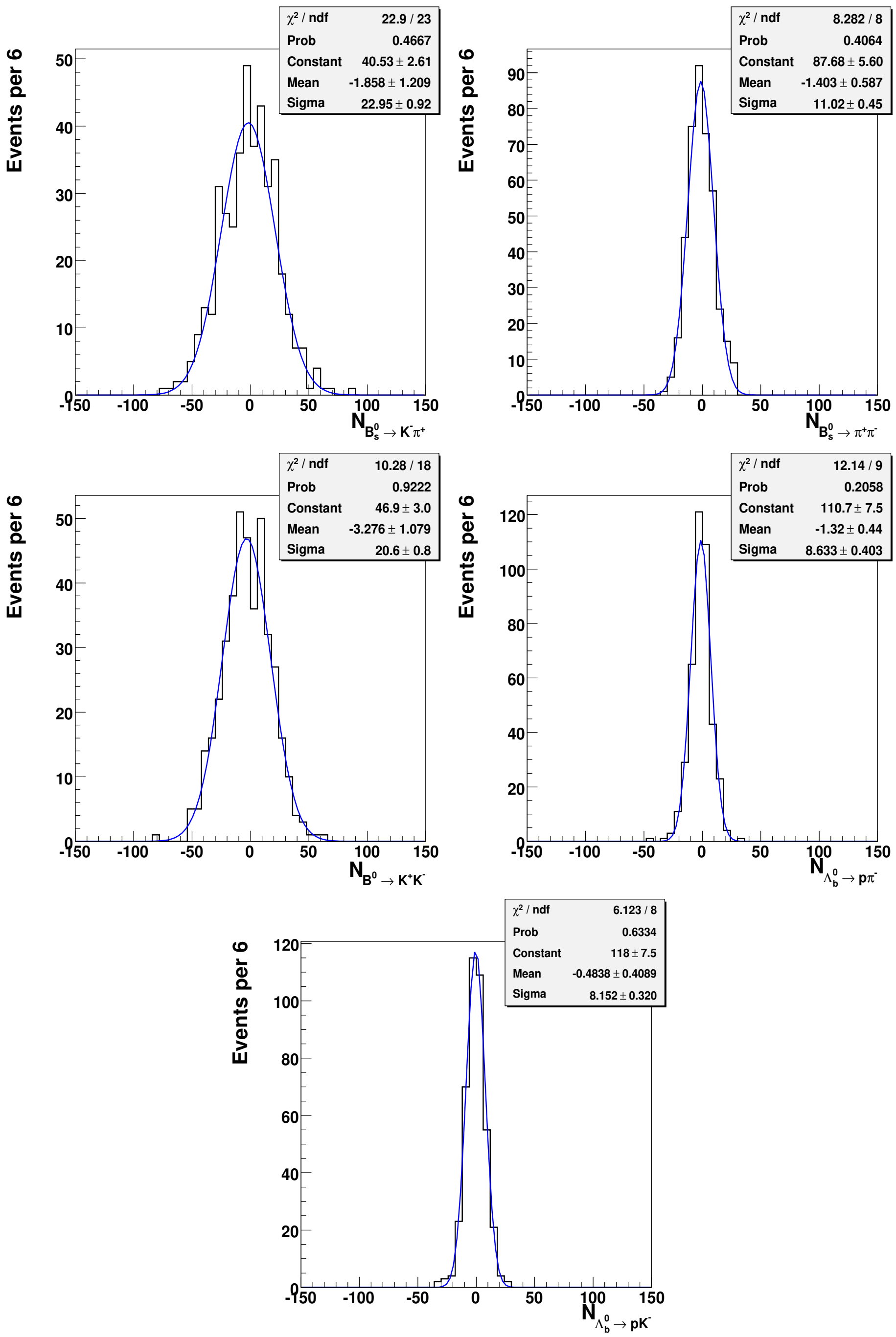

FIG. 66: Residual distributions of the yield for the rare modes (500 pseudo-experiments). The fractions of the rare modes are fixed to 0 in the toy sample generation. The distributions are clearly gaussians.

mode	$N_S \pm \sigma(N_S)$	TOY stat. $(f = 0)$	syst.	Sign.(TOY stat.$(f = 0)$ + syst.)
$B^0 \to K^+K^-$	61±25	21	35	1.5σ
$B_s^0 \to \pi^+\pi^-$	26±16	11	14	1.5σ
$B_s^0 \to K^-\pi^+$	230±34	23	16	8.2σ
$\Lambda_b^0 \to p\pi^-$	110±18	9	16	6.0σ
$\Lambda_b^0 \to pK^-$	156±20	8	11	11.5σ

TABLE XXIV: Significance of the new rare modes. We calculated the significance performing additional global fits onto the toy samples (pseudo-experiments) where the frations of all rare modes ($B^0 \to K^+K^-$, $B_s^0 \to K^-\pi^+$,$B_s^0 \to \pi^+\pi^-$, $\Lambda_b^0 \to p\pi^-$, $\Lambda_b^0 \to pK^-$) were fixed to 0. *First column*: rare modes. *Second column*: yield (N_S) returned from the fit on data $\pm 1\sigma$ statistical uncertainty ($\sigma(N_S)$). *Third column*: statistical uncertainty returned from the fits on the toy samples. *Fourth column*: systematic uncertainty. *Last column*: significance: the ratio between the yield N_S (first column) returned from the fit on the data and the quadrature sum of the statistical uncertainty from pseudo-experiments (third column) and the systematic uncertainty (fouth column).